Turbulent Flow over a Superhydrophobic Surface with Isotropic Slip

By

Babak Vajdi Hokmabad

A thesis submitted in partial fulfillment of the requirements for the degree of

Master of Science

Department of Mechanical Engineering

University of Alberta

Abstract

Superhydrophobic surfaces are proven to be capable of reducing the skin friction in laminar and turbulent flows. These surfaces consist of micro/nano-scale hydrophobic roughness features which make the surface render a non-wetting property due to the entrainment of air pockets between the solid surface and the liquid phase. This shear free air-water interface reduces the frictional drag force. This flow control method has two distinct effects in turbulent flow: drag reduction due to effective slip velocity and drag reduction associated with the modification of the turbulent flow structures (Rastegari & Akhavan, 2015). In the current research, the turbulent structure of the inner layer of a turbulent channel flow over a non-wetted superhydrophobic (SHO) surface with random pattern is experimentally studied. The results are compared with the wetted counterpart and also a smooth reference surface. Two planar particle image velocimetry (PIV) measurements are carried out in the streamwise/spanwise and streamwise/wall-normal planes. The vector fields are obtained from both ensemble averaging and individual cross-correlations of double-frame PIV images. The results showed a small increase (~5%) of the mean velocity profile at y^+=10 over the non-wetted surface in comparison with the wetted and the smooth surfaces. Up to 15% reduction of normal and shear Reynolds stresses is observed in the inner layer over the non-wetted SHO surface. The wetted SHO counterpart demonstrates no effect on the mean velocity and Reynolds stresses in comparison with the smooth surface implying that the surface is hydrodynamically smooth. A noticeable suppression of the sweep and ejection events, increase of the spanwise spacing of the low and high speed streaks, and attenuation of vortical structures are observed over the non-wetted SHO. These indicate attenuation of the turbulence regeneration cycle due to the slip boundary condition over the non-wetted SHO surfaces with random texture. Tomographic PIV (tomo-PIV) and 3D particle

tracking velocimetry (3D-PTV) as three-dimensional flow measurement techniques can unravel the relevant physics by revealing the flow modifications across the third dimension. The performance of these measurements is evaluated through comparison with DNS data in the literature. The results show that 3D-PTV is more accurate compared to tomo-PIV especially in near-wall region where noise increases for all PIV measurements.

Preface

This thesis contains experimental investigations of turbulent channel flow over a superhydrophobic surface with an emphasis on detailed study of turbulent flow modification. Application of planar and three-dimensional measurement techniques is also evaluated.

The literature review on the fundamentals of turbulent channel flow – in terms of governing equations, flow characterization and coherent flow structures–, superhydrophobic surfaces and measurement techniques are carried out by BVH.

In chapter 3, the utilized planar particle tracking velocimetry (2C-PTV) program is developed by Sina Rafati, Ph.D. student. The discussion of the algorithm and the results in chapter 5 are also prepared with assistance of the code developer. All of the experiments, data analysis and interpretation presented in chapters 4-6 are conceived by BVH under supervision of Dr. S. Ghaemi.

This thesis is dedicated to my family,

Aliasghar, Afsaneh and Siamak.

Acknowledgment

First and foremost, I owe a debt of gratitude to my supervisor, Dr. Sina Ghaemi. Aside from the scientific provision and thoughtful supervision, his patience and endless supports allowed me to experience working in a positive academic environment.

I am very grateful to Sina Rafati for his unconditional helps. He is an outstandingly insightful experimentalist whose patience in teaching the technical skills and introducing the details of experimentation accelerated the procedure of this research and certainly made the work much stronger.

I had the privilege to be labmates with talented graduate and undergraduate students during my career at University of Alberta, from all of whom I have learned valuable lessons.

I am forever thankful for my family's support and sacrifice. They taught me the value of knowledge and encouraged me to pursue my education.

Contents

List of Figures

List of Tables

1. Introduction

The friction force between fluid and solid surfaces is a significant source of energy loss in turbulent industrial flows. The efficiency of transportation pipelines and marine vessels is limited by friction drag that has prompted interest in drag reduction methods using various active and passive techniques. Hitherto, polymer additives (White & Mungal, 2008), near-wall addition of bubbles (Sanders *et al.*, 2006) and air layer (Elbing *et al.*, 2008), and wall surface modification (Carpenter 1997; Choi 2006; Rothstein 2010a) have been employed. The latter method of surface modification is of particular interest due to no requirement for a supply of polymer or gas and also due to recent advances in micro/nano-manufacturing technique.

The prevailing idea that the smoother is the surface, the smaller is the drag, was undermined once drag reduction was observed by applying streamwise grooves known as riblets on the wall surface (Walsh 1983; Walsh & Lindemann 1984). Riblets result in reduction of skin friction in spite of the fact that the wetted area has dramatically increased. Later on, Carpenter (1997) and Sirovich & Karlsson (1997) designed random patterns of v-shaped roughness elements interacting with the small scale coherent eddy structures in the wall region to break up the phase coherence of the vortices leading to maximum 12 % skin friction reduction. However, the final

result was sensitive to the geometry and flow circumstances as the subsequent attempts to reproduce the results were partially successful (Choi 2006).

A recent surface modification technique includes fabrication of micro/nano size patterns on an intrinsically hydrophobic material. The result is known as a superhydrophobic (SHO) surface, in which because of the low surface energy of the material, the adhesion force cannot overcome the water surface tension. This phenomenon, known as the Cassie state, results in a partially or fully non-wetted surface (Lafuma & Quéré 2003). When submerged in water, microscale air pockets will be trapped and retain in the pores and void regions of the surface forming a plastron. While the slip length over smooth hydrophilic surfaces is in the order of mean-free-path of the liquid molecules, the slip of water over non-wetted SHO surfaces in laminar flows has reported to be in the order of 10 μm (Rothstein, 2010a). This, in turn, results in significant drop in wall shear stress.

Possibility of deriving analytical (Lauga & Stone, 2003) studies on laminar flows over SHO surfaces has prompted significant attention leading to numerous publications with theoretical and experimental results (a comprehensive review is conducted by (Rothstein, 2010a)). Yet, due to the lack of an analytical solution, there remains demand to further study the effect of SHO surfaces in turbulent wall flows. Apart from the longevity and durability challenges of SHO applications, many open questions are found in terms of fluid dynamics of the turbulent flow over SHO surfaces and the circumstances of skin friction reduction. Mathematical analysis of Rastegari & Akhavan (2015) shows that the effect of superhydrophobicity is twofold in turbulent flow. One effect is attributed to the slip velocity over the surface which is supposed to alter the mean velocity profile and the other one is associated with the modifications to the turbulence structure and dynamics within the flow. In contrast to the laminar flow, the topography of the SHO surface significantly interacts with the inner flow of the turbulent boundary layer (TBL) which requires further characterization of the SHO roughness profile with respect to the near wall flow physics. The numerous questions here necessitate a thorough investigation on the underlying causes for modifications to turbulence production and transport. This could include the study of the different flow physics responsible for turbulence production in the self-generation cycle of turbulent flow.

This thesis contains experimental studies of turbulent flow over a superhydrophobic surface with random structure with an emphasis on turbulence physics of the boundary layer. It starts with providing an introduction to basic concepts and background in chapter 2 including the basic knowledge behind turbulent boundary layer, superhydrophobic surfaces, planar and volumetric tomographic particle images velocimetry (tomo-PIV) techniques are presented in this chapter. In chapter 3, the experimental methodology and setups including planar PIV, high-magnification particle tracking velocimetry (PTV) and tomo-PIV are discussed. The main results are presented in the following three chapters:

Chapter 4. "*Turbulent flow over wetted and non-wetted superhydrophobic counterparts with random structure*". The results of the planar 2C-PIV are presented. This experiment aims at obtaining the mean velocity profiles and detailed turbulent statistics in the buffer layer and log-layer of the TBL over both smooth and SHO surfaces. Reynolds stresses, sweep/ejection events and two-dimensional vortex analysis are carried out and discussed in this chapter.

Chapter 5. "*Near-wall flow measurement using long-range micro-PTV: Assessment of measurement accuracy*". In this chapter, the procedures carried out to warrant standard channel flow as well as more accurate measurements are discussed. The evaluation of high-magnification near-wall flow is presented to ascertain the fully-developed turbulent boundary layer flow. Channel-wide two-dimensional particle tracking velocimetry technique is conducted to scrutinize the symmetry of the mean flow. Further efforts aiming at improvement of the illumination system and flow seeding quality are discussed. An in-house PTV code (developed by Sina Rafati) is applied here to process the near-wall high-magnification images.

Chapter 6. "*Evaluation of 3D measurement system: Tomographic PIV and 3D-PTV* ". Three-dimensional measurement of the TBL is performed. Performance of tomographic PIV and 3D-PTV techniques are evaluated through comparison with DNS reference data. Acquisition of the spanwise turbulent intensities is of vital importance to scrutinize the drag reduction method's effect on turbulent flow modification.

In Conclusion and future research chapter, final remarks and recommendations for future work are presented.

2. Literature review

2. 1. Turbulent channel flow

In this section, the terminology associated with the turbulent wall flow is introduced followed by the theoretical modeling of the turbulent channel flow. Unsteady organization of the coherent flow structures and their interactions are also overviewed. Most of the discussion is adopted from Pope (2000).

2.1.1. Terminology

The presence of a solid boundary in turbulent shear flow leads to zero fluid velocity at the stationary solid surface (no-slip boundary condition). The confinement imposed by the geometry of the canonical channels with parallel walls impedes the perpetuating growth of the turbulent boundary layer in wall-normal direction. This confined flow ultimately turns into fully-developed flow which is statistically independent of the streamwise direction.

The current thesis focuses on the turbulent channel flow of an incompressible fluid between two parallel plates (figure 2.1). As primary assumptions, the channel is long enough so that the flow is fully-developed (statistically independent of x) with a sufficient aspect ratio to ensure that the flow is statistically independent of the spanwise, z, directions. x denotes the streamwsie direction (mean flow direction) while the mean velocity changes in the wall-normal direction, y.

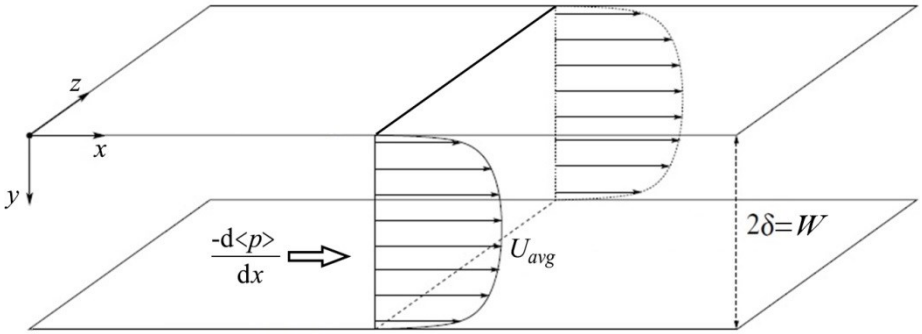

Fig. 2.1.The coordinate system, channel geometry and mean velocity profile of the channel flow. Flow is derived by pressure gradient.

The flow is studied in a Cartesian coordinate with x-, y-, and z-coordinates denoting the streamwise, wall-normal, and spanwise directions of a channel flow, respectively. The instantaneous velocity vector is $\boldsymbol{U} = (U, V, W) = (U_1, U_2, U_3)$ between the walls located at $y = 0$ and $y = 2\delta$ with the mid-plane at $y = \delta$. The ensemble average of the quantities is indicated by $\langle\ \rangle$ and the flow is statistically stationary.

To study the fluctuations associated with turbulent flows the *Reynolds decomposition* is adopted as

$$\boldsymbol{U} = \langle \boldsymbol{U} \rangle + \boldsymbol{u} \tag{2.1}$$

where $\boldsymbol{u} = (u, v, w) = (u_1, u_2, u_3)$ shows the fluctuation of the velocity vectors. In the fully-developed flow region, the boundary layer formed over the two walls merge at the channel centerline. To calculate the Reynolds number of the flow between two parallel plates typically the channel width (W=2δ) is used as follows

$$\mathrm{Re} = \frac{\rho\, U_{avg}\, 2\delta}{\mu} \tag{2.2}$$

where ρ is the density and μ is the dynamic viscosity of water and U_{avg} is the mean flow velocity across the channel.

The wall shear stress (τ_w) of the turbulent channel flow which is due entirely to the viscous effects is

$$\tau_w = \mu \frac{\partial \langle U \rangle}{\partial y}\Big|_{y=0}. \tag{2.3}$$

This quantity in conjunction with viscosity and density are used to define the inner scales which are velocity and length scales associated with the flow in the vicinity of the wall. The inner velocity scale — also known as friction velocity —is defined as

$$u_\tau = \sqrt{\frac{\tau_w}{\rho}} \tag{2.4}$$

and the viscous length scale —also known as wall unit — is

$$\delta_v \equiv \nu \sqrt{\frac{\rho}{\tau_w}} = \frac{\nu}{u_\tau} \tag{2.5}$$

where $\nu = \mu / \rho$ is the kinematic viscosity of water.

2.1.2. Conservation laws

The conservation of mass and momentum associated with an incompressible flow field has to be obtained. The Reynolds decomposition of the mass conservation equation is

$$\frac{\partial U_i}{\partial x_i} = 0 \tag{2.6}$$

which shows the divergence-free behavior of both the mean flow and the fluctuating flow fields. The conservation of momentum mathematically relates the material acceleration of the flow to the pressure gradient and the viscous diffusion as follows

$$\frac{\partial U_i}{\partial t} + U_j \frac{\partial U_i}{\partial x_j} = -\frac{1}{\rho}\frac{\partial P}{\partial x_i} + \nu \frac{\partial^2 U_i}{\partial x_j \partial x_j} \tag{2.7}$$

Reynolds decomposition of the velocity field followed by taking the mean results in the so-called "mean-momentum" or the "Reynolds equation" becomes

$$\frac{\partial \langle U_i \rangle}{\partial t} + \langle U_j \rangle \frac{\partial \langle U_i \rangle}{\partial x_j} = -\frac{1}{\rho}\frac{\partial \langle P \rangle}{\partial x_i} - \frac{\partial \langle u_i u_j \rangle}{\partial x_j} + \nu \frac{\partial^2 \langle U_i \rangle}{\partial x_j \partial x_j} \tag{2.8}$$

Further simplifications are possible through application of the boundary layer approximation in channel flow i.e., the mean flow is two-dimensional and statistically stationary. Thus,

$$\frac{\partial}{\partial t} = 0,\ \frac{\partial}{\partial z} = 0,\ \text{and}\ \langle W \rangle = 0 \tag{2.9}$$

Since $\langle W \rangle$ is zero and $\langle U \rangle$ is independent of *x,* the incompressible continuity equation reduces to

$$\frac{\partial V}{\partial y} = const. \tag{2.10}$$

Applying the boundary condition $\langle V \rangle_{y=0} = 0$

$$\frac{\partial V}{\partial y} = 0 \tag{2.11}$$

across the channel width.

The *y* component of the momentum equation reduces to

$$\frac{d}{dy}\langle v^2 \rangle - \frac{1}{\rho}\frac{\partial \langle p \rangle}{\partial y} = 0 \tag{2.12}$$

which in turn, with the boundary condition $\langle v^2 \rangle_{y=0} = 0$ can be integrated along the *y* direction

$$\langle v^2 \rangle + \frac{\langle p \rangle}{\rho} = \frac{p_w(x)}{\rho} \tag{2.13}$$

in which p_w is the mean pressure on the bottom wall.

The *x* component of the momentum equation reduces to

$$\nu \frac{d^2\langle U \rangle}{dy^2} - \frac{d}{dy}\langle uv \rangle - \frac{1}{\rho}\frac{\partial \langle p \rangle}{\partial x} = 0 \tag{2.14}$$

which can also be rewritten in terms of total shear stress

$$\frac{d\tau}{dy} = \frac{dp_w}{dx} \tag{2.15}$$

where total shear stress is

$$\tau = \mu \frac{\partial \langle U \rangle}{\partial y} - \rho \langle uv \rangle. \tag{2.16}$$

According to equation 2.16, the total shear stress consists of two components which are the viscous and the Reynolds stress. The term $\mu\frac{\partial\langle U\rangle}{\partial y}$ represents the viscous contribution while $-\rho\langle uv\rangle$ is the representative term for Reynolds stress contribution.

2.1.3. Mean velocity profile

The division of the turbulent boundary layer profile into particular regions stems from the relative contribution of the viscous and the Reynolds stress components of the total shear stress in equation 2.16.

In the vicinity of the wall, the viscous effects are dominant so, the mean velocity profile of this region known as the inner layer is only a function of the wall-shear stress, fluid properties, and the wall-normal distance so that

$$\langle U\rangle = F(\tau_w, \mu, \rho, y) \tag{2.17}$$

in which F is a universal non-dimensional function used for describing the inner layer. Dimensional analysis leads to two dimensionless parameters of $u^+ = \langle U\rangle/u_\tau$ and $y^+ = yu_\tau/\nu$ useful for expressing equation 2.17. Hence,

$$\frac{\langle U\rangle}{u_\tau} = f\left(\frac{y}{\delta_v}\right). \tag{2.18}$$

This relation is called the law of the wall. Experimental measurements at the immediate vicinity of the wall in which the viscous effects dominate have observed a linear behavior

$$\frac{\langle U\rangle}{u_\tau} = \frac{y}{\delta_v} \quad \text{or} \quad u^+ = y^+ \tag{2.19}$$

This linear trend persists in a limited region near the wall (y^+<5) which is called the viscous sublayer. The viscous effects attenuate as we move away from the wall. In the region between y^+= 5 and 40, known as the buffer layer, the transition between the preceding viscous-dominated and the proceeding turbulence-dominated regions occurs (Pope, 2000). The majority of the turbulence energy production and dissipation happen in the buffer layer (Klebanoff, 1955; Pope, 2000). Beyond this layer, the viscous effects contribution to the total shear stress is negligible and consequently the velocity is not a function of μ. In this region known as the outer layer, the

momentum is mostly transported by the large (in the scale of boundary layer thickness δ) eddies. Thus, in this region the velocity defect law is applied

$$\frac{U_{avg}-\langle U\rangle}{u_\tau} = g\left(\frac{y}{\delta}\right). \tag{2.20}$$

where, g is a function and may depend on the Reynolds number. However, in this region once $\delta_v << y << \delta$, not only viscous effects are negligible (i.e. dependence on δ_v vanishes) but also the length scale δ is not important. This sub-region is called the overlap region. Therefore, the function adopts a constant value and the equation, in terms of velocity gradient, becomes

$$\frac{du^+}{dy^+} = \frac{1}{\kappa\, y^+} \tag{2.21}$$

which integrates to

$$u^+ = \frac{1}{\kappa}\ln y^+ + B, \tag{2.22}$$

where κ is the von Karman constant and B is a constant. This equation is called the logarithmic law of the wall—also known as log law— due to von Karman (Pope, 2000). The constants are κ = 0.41 and B = 5.2 acquired from experimental data for turbulent channel flows with smooth walls.

2.1.4. Coherent structures

In wall turbulence, coherent structures transport the majority of momentum and contain Reynolds stresses that produce turbulent kinetic energy. They are defined as individual three-dimensional motions in the turbulent flow with spatial and temporal coherence (Adrian & Adrian, 2007; Lumley & Blossey, 1998). Robinson (1991) has comprehensively reviewed and classified these coherent structures. Each category of the taxonomy presented by Robinson has a particular role in production and transport of turbulence completing the self-sustaining process of near-wall turbulence structures. The kinematic (e.g. length scales, shape, vorticity) and dynamic (origin, stability, contribution to averages) properties of the coherent structures in turbulent flows are of interest due to the fact that they are responsible for the production and transport of

turbulence. Additionally, the interactions between these flow structures are the connecting links forming the self-generating cycle of turbulence production (Kim, 2011).

Control of these coherent structures has been recently introduced as an effective method of disrupting the self-generating turbulence production process leading to development of systematic flow control strategies. Extensive investigations are conducted to develop passive (Sirovich & Karlsson, 1997) and active (Elbing *et al.*, 2008; Kim, 2011) methods of flow control interfering with the self-generating process mainly aiming at skin-friction reduction.

Low and high speed streaks

In the vicinity of the wall in turbulent boundary layer flow, the ubiquitous flow structures are the low and high speed streaks which appear in the form of spanwise modulations in the streamwise velocity. Elongated in streamwise direction, low and high speed streaks show negative and positive fluctuations in streamwise velocity, respectively. First observation of these flow structures dates back to 1967 in the hydrogen bubble visualizations of Kline *et al.* (1967). The low-speed streaks in a turbulent boundary layer are known to originate in the viscous sub-layer and then during the ejection events (reviewed in section 1.3.2) are lifted into the logarithmic region (Hussain, 1986; Smith & Metzler, 1983). These streaks are created by vortices (reviewed in section1.3.3), which are roughly aligned in the streamwise direction (Kim *et al.*, 1987; Kim, 2011) as shown in figure 2.2.

The average spanwise spacing between the neighbor low and high speed streaks is an important parameter widely used to characterize the streaks. The measured value for this parameter in sublayer is reported to be about $100\delta_v$ (Smith & Metzler, 1983). Although this parameter is reported to grow in wall-normal direction, it is observed to be invariant with Reynolds number up to $Re_\theta = 6000$ (Ghaemi, 2013).

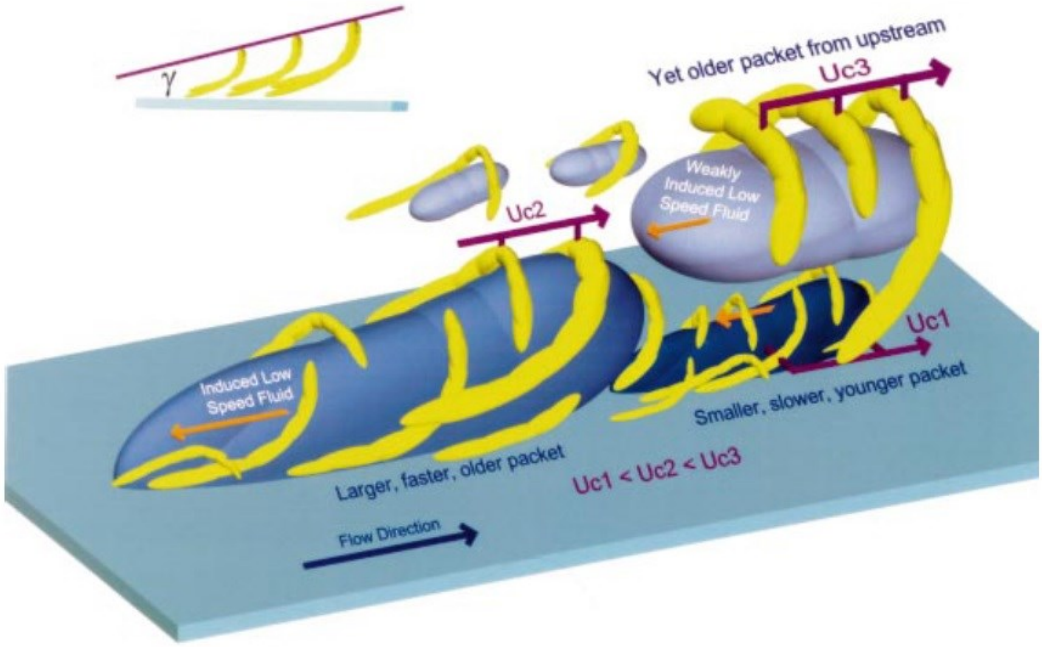

Fig. 2.2. Arrangement of the coherent structure in the near-wall region (viscous and buffer layers). Nucleation of the quasi-streamwise vortices around the low speed streaks is illustrated. From (Adrian, 2000) reprinted with permission of CAMBRIDGE UNIVERSITY PRESS.

Ejection and sweep events

Ejection events are referred to the relative upward motion of the negative streamwise fluctuations (low-speed streaks) away from the wall by means of positive wall-normal fluctuations (shown as Q_2 in figure 2.3). Thus, the motion consists of $u < 0$ and $v > 0$ fluctuations leading to turbulence production ($uv < 0$) accompanied by transport of vorticity away from the wall (Adrian, 2007). Due to their role in conversion of the large scale low-speed streaks into small-scale vortical structures, the ejection events are one of the key factors in the turbulence production. Conversely, sweep events are referred to the inrush of the positive streamwise fluctuations (high-speed flow) towards the surface by means of negative wall-normal fluctuations (denoted by Q_4 in figure 2.3). These sweep events also contribute to the production in the energy cascade of turbulence. The ejection and sweep events are found to be the main factors in turbulence production in the turbulent boundary layer (Kim, 2011). The near-wall region of the flow ($y^+< 12$) is dominated by the sweep events contributing to turbulence production whereas the ejection motions prevail in the region $y^+ > 12$ (Kim *et al.*, 1987; Wallace

et al., 1972). The quadrant splitting of the Reynolds shear stress provides detailed information on the contribution of ejection and sweep motions to the total turbulence production (Wallace *et al.*, 1972). DNS results of Kim *et al.* (1987) reported side-by-side spanwsie arrangement of ejection and sweep events.

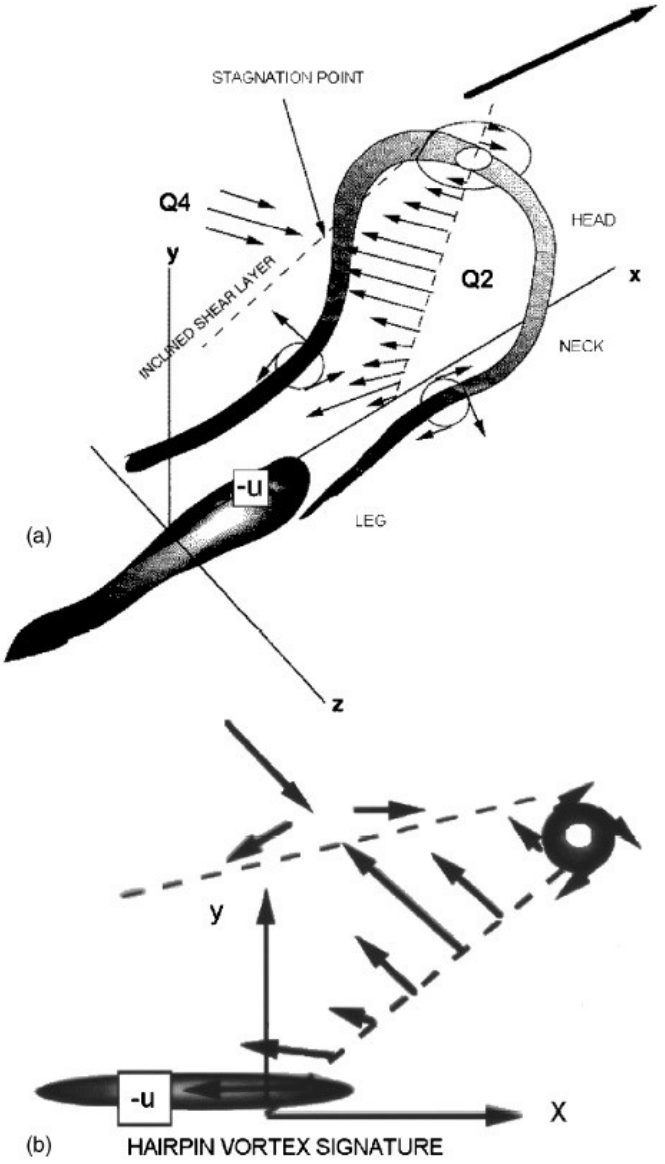

Fig. 2.3. (a) Schematic of a hairpin eddy attached to the wall; (b) signature of the hairpin eddy in the streamwise wall-normal plane. From (Adrian *et al.*, 2000) reprinted with permission of CAMBRIDGE UNIVERSITY PRESS.

Vortices

A vortex is a spatially and temporally coherent flow structure in the form of a distinct region in the flow with circular or spiral pattern of streamlines when viewed from a reference frame moving with the center of the vortex core (Robinson, 1991; Spalart, 1988). It can also be defined as a coherent region in the flow having excess vorticity relative to shear strain rate (Davidson, 2004).

The ubiquitous vortices found in turbulent boundary layer are quasi-streamwise and hairpin vortices (Robinson, 1991). A schematic illustration of a hairpin vortex is presented in figure 2.3. As shown, it mainly consists of a spanwise section and two trailing quasi-streamwise sections. The hairpin vortices are usually found in packet of hairpins stemmed from the autogeneration process that spawns multiple hairpins with different sizes in streamwise direction (Adrian, 2007). Hairpins are typically observed in logarithmic layer and outer layer. The quasi-streamwise vortices, typically in the order of 20–50 wall units in diameter, are mostly found in the buffer layer (y^+ = 10–50) (Kim *et al.*, 1987). It is proven that the majority of the skin-friction in turbulent boundary layers is induced by the quasi-streamwise vortices (Kim, 2011).

The interaction between the coherent flow structures in the turbulent boundary layer is of significant importance due their roles in forming the self-sustaining turbulence production process. The hairpin vortex paradigm of Theodorsen (1952) in conjunction with the quasi-streamwise vortex paradigm have been widely accepted. A conceptual model proposed by Smith & Metzler (1983) suggests that an unstable shear layer around a low-speed streak forms a hairpin-like vortex. This vortex moves away from the wall due to self-induction with the trailing quasi-streamwise vortices stretching and maintaining their near-wall position. Induced by these counter-rotating vortices the low speed streak lifts up and moves away from the wall leading to an ejection event. Subsequently, on the sides of this ejection event the high-speed fluid sweeps towards the wall.

2.2. Superhydrophobic surfaces

Once a water droplet rolls on a surface, maintaining a closely spherical shape, and the surface does not get wet, such a surface is called superhydrophobic or super-water-repellent. In other words, superhydrophobic surface is capable of repelling water droplets implying an extremely low wettability. Common superhydrophobic surfaces in nature are lotus leaf, duck feathers, silver ragwort leaves and water-strider legs to name a few. Synthetic superhydrophobic surfaces are also obtained through a variety of exponentially growing fabrication methods. Either natural or synthetic, these surfaces consist of micro- or nanosized roughness elements in one level or in hierarchical structures (see figure 2.4).

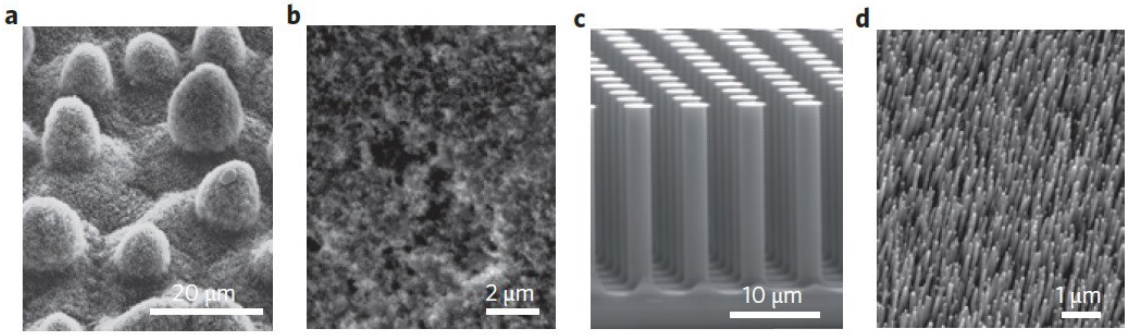

Fig. 2.4. Scanning electron microscopy (SEM) images of four common superhydrophobic surfaces. a) Hierarchical structure of the Lotus leaf, b) Black soot obtained from a lighted candle, c) Patterned micro-pillars, d) Carbon-nanotube carpet. From (Bocquet & Lauga, 2011) reprinted with permission of NATURE PUBLISHING GROUP.

Prior to further discussion on the surface classifications and characterization methods, it is necessary to review the relevant concepts and physics.

2.2.1. Fundamentals

Superhydrophobic surfaces in nature

The discovery of the superhydrophobicity of the lotus leaf and the mechanism of repellency was a great breakthrough in developing superhydrophobic surfaces. The latter is known as the lotus effect and enables water or oil droplets to roll off the leaf surface with no residue left behind. The surface roughness is an important factor causing the water-repellent behavior of all superhydrophobic surfaces. The lotus leaf's cuticle can be considered a composite material

mainly consisting of a network of cutin and hydrophobic waxes. In this region, the multilayer composite or hierarchical surface structures are created by convex cells covered by superimposed layer of wax tubules (Koch *et al.*, 2008; Yan *et al.*, 2011). This set of roughness elements deters the water from wetting the surface. Similar to lotus leaf, there are several other examples for natural surperhydrophobic surfaces in plants. Taro (Colocasia esculenta) leaf with similar surface roughness to lotus leaf (Barthlott & Neinhuis, 1997) and India canna (Canna generalis bailey) leaves and the rice leaves with binary micro/nanoscale surface structures (Guo & Liu, 2007) are other botanical examples.

With the same concept behind, there have been significant superhydrophobicity produced in animal realm. The leg of a water strider which consists of several needle-shaped setae a few nanometers to 3 μm in diameter is a good example (Evershed *et al.*, 1983). Each microseta is covered with numerous nanoscaled grooves. This hierarchical structure in conjunction with the hydrophobic wax origins the superhydrophobicity of the water strider's legs.

Artificial superhydrophobic surfaces

Recent remarkable advances in micro/nanofabrication techniques (Yan *et al.*, 2011) enabled the scholars to fabricate features as small as a few nanometers. The discovery of the mechanism of superhydriphobicity in nature prompted the idea of mimicking these natural structures by means of state-of-the-art fabrication techniques. Several techniques have been successfully developed for production of surfaces with regular patterns (structured) or random textures. Mostly produced by soft lithography or photo-lithography, the structured superhydrophobic surfaces are developed in small-scale (due to the fabrication limitation) and employed in small-scale application such as microfluidics. Surfaces with random roughness are produced through aerosol spray coating, chemical reactions and thermal spray coating with ease of fabrication and large scale production possibility.

Despite being well-established, the fabrication methods and material design yet needs to resolve the challenges for higher practicality of the surfaces. The first challenge is the thermodynamic robustness of these structures – also known as longevity– which is associated with the transition of the wetting state from Cassie to Wenzel mode. Specifically in under-water application where

the hydrostatic pressure is critically high the possibility of plastron failure increases dramatically. Second challenge is related to the mechanical robustness—also known as durability— of the surface structures which are fragile during physical contacts. Further challenges warranted by particular applications also exist such as finding optimal design for manipulating transport phenomena.

Wetting phenomena

Wetting phenomena for a sessile droplet on a flat homogeneous surface is modeled by the Young's equation (Callies & Quéré, 2005). The drop-surface contact area is in the form of a disk where the three-phase contact line is present, as shown in figure 2.5. The droplet contacts the solid at a contact angle θ. The balance between interfacial forces leads to the state in which the corresponding surface area is minimized. Following formula is attributed to Young's model (Yan *et al.*, 2011):

$$\cos\theta = \frac{\gamma_{SV} - \gamma_{SL}}{\gamma_{LV}} \tag{2.23}$$

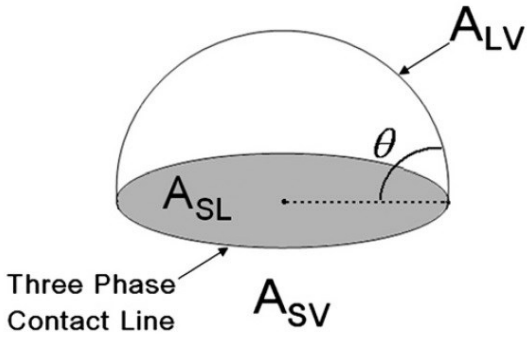

Fig. 2.5. A liquid drop balanced by three interfaces. A denotes the surface area while SV, SL and LV correspond to the interfaces between solid, liquid and vapor, respectively (Yan *et al.*, 2011) reprinted with permission of ELSEVIER.

where γ is the surface tension, θ is the intrinsic contact angle (Young Contact Angle) and SV, SL and LV correspond to the interfaces between solid, liquid and vapor, respectively. The Young equation relates the intrinsic contact angle to interfacial tensions (energies). Nevertheless, real

surfaces always have different surface profiles. Wenzel proposed an equation relating the contact angle to surface roughness and surface energies (Wenzel, 1936 and 1949), which can be written as

$$r(\gamma_{SV} - \gamma_{SL}) = \gamma_{LV} \cos \theta_w^* \tag{2.24}$$

and then reformed as:

$$\cos \theta_w^* = r \cos \theta \tag{2.25}$$

where θ_w^* is the apparent Wenzel contact angle which signifies the apparent contact angle while the surface roughness effects are also considered. In this equation, r is a roughness factor that is the ratio of the wetted to projected area. In Wenzel's model, water penetrates the space between roughness elements which is the homogeneous wetting regime (Marmur, 2003).

The second wetting regime is the heterogeneous wetting state (metastable regime is in between). Heterogeneous wetting regime refers to the state in which air bubbles are entrapped inside the pores and grooves between roughness elements underneath the liquid phase. The Cassie–Baxter equation is applied to model this regime. The equilibrium contact angle in this state is proportional to the air-water interface, $(1 - \phi_s)$:

$$\cos \theta_w^* = -1 + \emptyset_s(\cos \theta + 1) \tag{2.26}$$

where ϕ_s is the wetted area fraction of the surface roughness.

2.2.2. Characterization

The Cassie wetting regime stemmed from superhydrophobicity is not achievable through chemical manipulations. Recently, the majority of the investigations were focused on the wetting phenomena, whereas the application of superhydrophobicity can extend beyond wetting and move towards the applications in surface- and bulk-transport phenomena. Working in the Cassie state, the interface of a superhydrophobic surface consists of liquid–air and direct solid–liquid contact regions. This interface functions as a flat bubble mattress intervening the solid and liquid phases which in essence influences the transport of liquids, particles and heat (Bocquet & Lauga, 2011).

The skin friction drag is determined by fluid viscosity, strain rate (velocity gradient), and surface area (Samaha *et al.*, 2012) where the product of fluid viscosity and velocity gradient yields the shear stress. The main subject of interest in the implications of superhydrophobicity in transport phenomena is their potential in reducing skin friction drag. Indeed, the air pockets entrapped in between the liquid and the solid act as partial slip regions yielding a lower skin-friction. Rothstein (2010b) has comprehensively reviewed the simulations and the experiments reporting this effect. Although it has been found that the small-scale surface phenomena can have large scale impacts (Rothstein, 2010b) there is a demand for further investigation over the pertinence of small-scale surface phenomena to large-scale flow structures especially for turbulent flow. The requisite for developing a systematic model of the coupling between small-scale surface structures and large-scale flow behavior is defining a rigorous all-physics-inclusive characterization method which is specific to the target application. Below, the canonical characteristics of the superhydrophobic surfaces utilized in transport phenomena are reviewed.

Contact angle and contact angle hysteresis

Traditionally, two main criteria in characterizing the wetting states are the equilibrium water drop contact angle, θ, and contact angle hysteresis, $\Delta\theta$. The measurement procedure of these two parameters is illustrated in figure 2.6. $\Delta\theta$ is the difference between the advancing and receding stable contact angle $\theta_{adv} - \theta_{rec}$. Lower $\Delta\theta$ suggests that the water droplet does not stick to the surface and roll easily (rather than sliding) which are the traits for superhydrophobicity. The $\Delta\theta$ in the Wenzel state is a large number since the liquid-solid contact line is pinned along all roughness profiles while in Cassie state this line is only pinned along the wetted solid fraction of the surface. By convention, a surface is called superhydrophobic if its contact angle is higher than 150°.

In order to maximize the contact angle and its hysteresis, the spacing between the roughness elements should increase to raise the air fraction of the surface. However, this leads to an inevitable practical trade-off. In Cassie state, there is a limit for the static pressure before the air-water interface collapses and the system reverts to Wenzel state. This pressure is calculated for a surface composed of micro-posts (e.g., Rothstein, 2010b). However, this value cannot be found theoretically for surfaces with random roughness.

Defined above, the effective contact angle and its hysteresis are the traditional way of characterizing superhydrophobic surfaces. However, the suitablility of these parameters for characterization of the performance of superhydrophobic surfaces in transport phenomena requires further investigation. For example, as shown by Bidkar *et al.*'s experiments (2014), surfaces with identical contact angles but different length scales yielded different skin friction values.

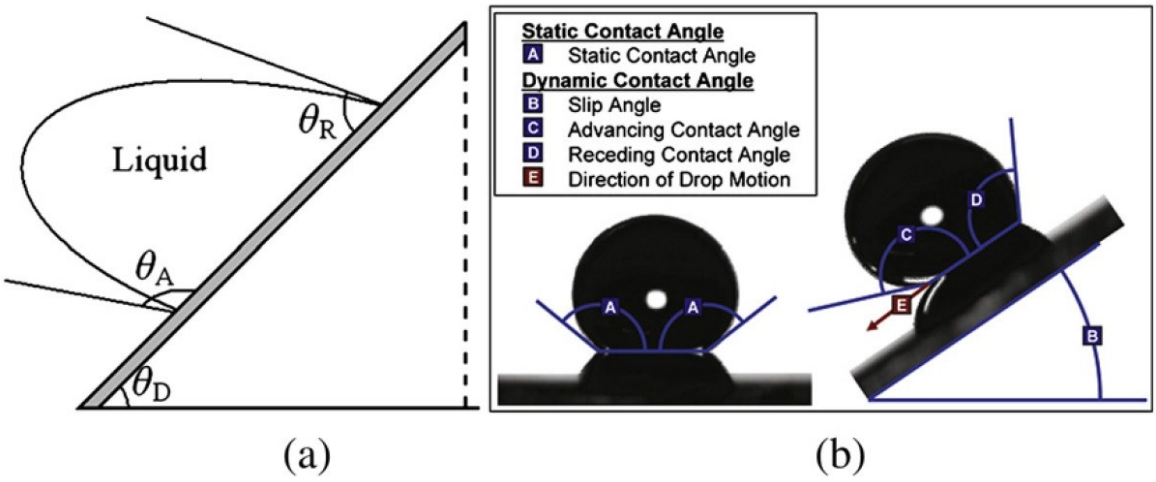

Fig. 2.6. a) A liquid drop on declined surface, θ_A is advancing angle and θ_R denotes receding angle, b) static contact angle and dynamic contact angles (Yan *et al.*, 2011) reprinted with permission of ELSEVIER.

Slip length

Liquid slip over a surface happens once the tangential velocities of the flow and the solid surface are different at the interface. According to Navier's model (Navier, 1823), the magnitude of the slip velocity is proportional to the magnitude of the wall-normal velocity gradient while the slip length is the proportionality constant:

$$b = \frac{u_{slip}}{\frac{\partial u}{\partial z}\Big|_{wall}} \tag{2.27}$$

where u_{slip} is the area-weighted average slip velocity at the superhydrophobic wall, u is the streamwise velocity, and z is the normal direction (Samaha *et al.*, 2012). This slip length

indicates a distance inside the solid surface at which the velocity extrapolation reaches zero. Generally b has a finite value implying a partial slip. Distinguishing between three different types of interfacial slip would facilitate defining specific length scales suitable for the particular interfacial fluid dynamics.

Molecular (or intrinsic) slip: The slip of liquid molecules over a solid surface while in direct contact with the solid surface is known as the intrinsic slip. As shown by molecular dynamics simulations (Huang *et al.*, 2008; Sendner *et al.*, 2009) intrinsic slip does not cause a large b and it falls below 10 nm for realistic contact angles. Such a minuscule slip would not affect the large-scale flow phenomena and consequently are not of interest in engineering applications.

Apparent slip: The experiments at scales larger than molecular scale—in which surface minuscule roughness elements come into play— over hydrophobic materials indicated different slip lengths compared to intrinsic slip boundary condition. Vinogradova (1995) proposed the "gas cushion model" of hydrophobic slippage which describes the solid-liquid interface region as a lubricating "gas film". His calculations gave the apparent slip as:

$$b = e\left(\frac{\eta}{\eta_g} - 1\right) \simeq e\frac{\eta}{\eta_g} \tag{2.28}$$

where e is the layer thickness and η_g is gas viscosity which is different from bulk liquid viscosity, η. Using experimental values of b, the thickness of this air layer is found to be lower than 2 nm (Vinogradova & Belyaev, 2011). A modification to this scenario for making it more realistic is a nanobubble coated surface.

Effective slip: The effective slip length is the slippage found from measurement of the average flow over the length scale of the experimental configuration (Stone *et al.*, 2004; Vinogradova & Belyaev, 2011). Considering the macroscale flow (larger than the surface pattern length scales) along the true heterogeneous surface leads to the effective slip length which is a physical parameter that scales the surface-flow interaction and quantifies drag reduction. Recently, effective slip lengths up to 400 μm have been achieved (Lee & Kim, 2009).

In terms of slip direction, surfaces are categorized into two types. The ubiquitous one is isotropic which means that the slip length is identical in both streamwise and spanwise directions. This type in three dimensional flows such as turbulence could cause spanwise slip amplification. On

the other hand, anisotropic surfaces with higher slippage in one direction can be used for amplifying or guiding liquid flow in particular direction. Legs of water strider and superhydrophobic surface with parallel microgrooves are examples for anisotropic slippage.

Multiple length scales

Natural and recently artificial extreme superhydrophobicity is obtained through introducing hierarchical microscopic length scales on the hydrophobic surface. Yet, the effects of superhydrophobic surface with multiple length scales are not fully discovered. Beside the slip length, two characteristic length scales used for patterned superhydrophobic surfaces are the height of the roughness features and the feature spacing. Superhydrophobic surfaces with random roughness texture display a broad spectrum of scales (Roach *et al.*, 2008). Bidkar *et al.* (2014) reported the arithmetic roughness size of the superhydrophobic textures applied in a turbulent flow experiment. However, these characteristics would not lead to universality unless their pertinence to flow length scales is considered. For turbulent flow in particular, Martell *et al.,* (2010) and Bidkar *et al.* (2014) compared the ratio of roughness length scales to viscous sublayer thickness and proposed universal laws for observation of drag reduction behavior due to hydrophobicity.

2.3. Experimental methodology

In this section, the working principles of planar PIV are overviewed. This technique has been frequently applied for investigation of turbulent boundary layer in different experiments (e.g. Adrian *et al.*, 2000; Stanislas *et al.*, 2008). This technique is employed in this thesis to study the turbulent boundary layer statistics.

2.3.1. Planar particle image velocimetry

2.3.1.1. Basic principles

Particle image velocimetry is one of the common non-intrusive flow measurement methods which uses imaging techniques to indirectly measure the local displacement of fluid elements

over a certain time interval. The technique measures the flow velocity by recording and evaluating the displacement of small tracer particles which follow the local fluid motion. The tracer particles have to be small and light enough to be able to follow the flow and yet large enough to scatter sufficient light visible for the imaging system. The images of the measurement region, illuminated by a thin light sheet, are captured at two consecutive moments t_o and $t_o + \Delta t$. The time interval between the two images, Δt, should be selected so that same particles are captured in both images (their displacement, Δx, is not larger than the interrogation window).

Exposed to two successive pulses of laser, the motion of the illuminated tracers is captured in the corresponding images. Planar PIV provides information on the displacement of the tracer particles in two dimensions of the measurement plane. The displacement which is the projection of the particle group motion in the measurement plane is calculated by cross-correlation of the successive images and is used to determine the local velocity of the flow.

Figure 2.7 illustrates a schematic illustration of a regular planar PIV setup. The illumination and the imaging system followed by measurement procedure are also shown.

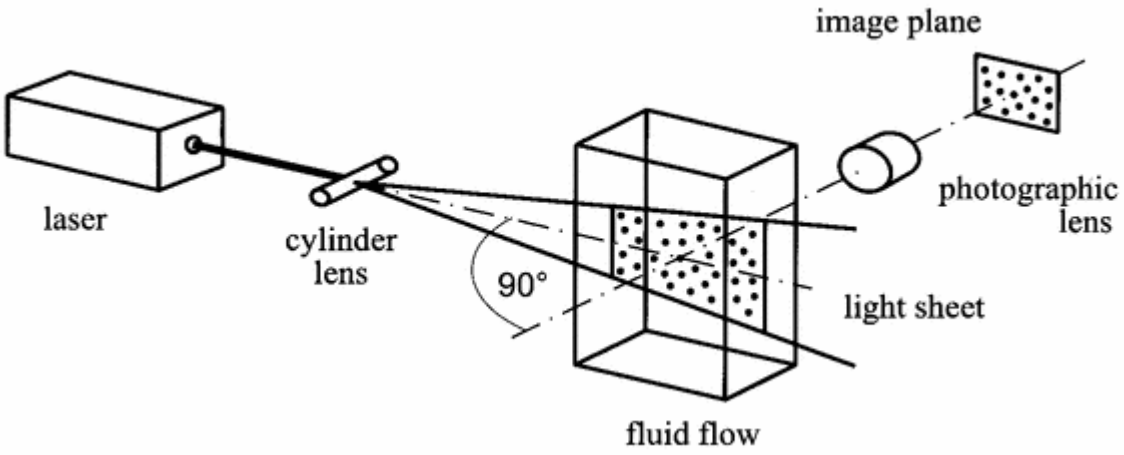

Fig. 2.7. A schematic view of the PIV setup showing illumination system and seeding particles. The imaging system records two consecutive images of the particles motion (Merzkirch, 2001) reprinted with permission of SPRINGER.

2.3.1.2. Seeding particles

Hydrodynamic fidelity of the tracer particles

Selecting appropriate tracer particles based on the criteria raised from the flow physics and the illumination and imaging requirements is crucial to ensure accurate velocimetry of the flow field. The relative motion of the particles and fluid flow can be characterized using a Reynolds number defined as (Scarano, 2013):

$$Re = \frac{\rho\, \Delta U\, d}{\mu} \tag{2.29}$$

Where ρ is the density of the surrounding fluid, ΔU is the magnitude of relative velocity between the particle and the fluid velocities and d is the diameter of the particle. Owing to the very small size of the particles (in the order of a few micrometers) the Re is typically smaller than unity implying that tracer motion is dominated by the viscous forces and the total force follows the Stokes law. According to Stokes law, the Stokes drag comprises the form and frictional components. Due to viscous forces dominance one can neglect the inertial terms in the Navier-Stokes equation and integrate the normal and tangential forces over the surface of a spherical particle to acquire the Stokes drag (Hinds, 2012)

$$F_D = 3\pi\, \mu\, d\, \Delta U \tag{2.30}$$

and the final equation of particle motion is

$$\frac{1}{18\mu} d^2 \left(\rho_p - \rho\right) \frac{dU_p}{dt} = \Delta U \tag{2.31}$$

in which ρ_p is the particle density. Based on this equation neutrally buoyant particles are the best choice for tracer particles due to the highest fidelity to the flow motions. From equation 2.31 we can find the particle response time as (Scarano, 2013):

$$\tau_p = d^2 \frac{(\rho_p - \rho)}{18\mu} \tag{2.32}$$

The fidelity of the particles to flow in turbulence is found by the particles Stokes number S_k

$$S_k = \frac{Particle\ response\ time}{flow\ characteristic\ time} \tag{2.33}$$

where for a turbulent boundary layer the flow characteristic time can be expressed as δ / U_b.

Scattering properties of the tracer particles

From optical visibility point of view, the light scattering properties of the tracers is important in PIV measurements. For PIV experiments, in which the particle diameter is usually larger than the wavelength of the illumination light, the Mie scattering theory applies. Based on this theory, the scattered light by a particle depends on the particle diameter, the refractive index of the particle relative to the surrounding medium and the wavelength of the laser light (Hulst, 1981). The scattering distribution varies considerably with the observation angle and the highest scattering intensity occurs at forward scattering position. Planar PIV experiments are mostly performed at 90° viewing angle.

2.3.1.3. Illumination

The illumination of the tracer particles is carried out using two successive laser pulses. Lasers emit monochromatic light beam which is free of chromatic aberrations (Raffel *et al.*, 2007). The most common device used in PIV measurements is the solid-state frequency doubled Nd-YAG laser that emits light with a wavelength of 532 nm. These dual cavity lasers produce two successive laser pulses independently. The two laser beams are aligned by a mirror and a polarizing beam combiner. The produced pulses have near infrared wavelength and then the light is converted into green by a frequency doubling crystal. The laser beam emitted in circular cross-section is converged into a thin sheet of light by means of spherical and cylindrical lenses.

2.3.1.4. Imaging

Images of the particle are recorded by charge coupled device (CCD) camera which contains a sensor that converts collected photons into free electrons. Each individual element in the CCD sensors is called a pixel which is subject to a given light intensity during the exposure. The particle size is selected for optimal particle image size on the image plane noting that the light scattering by particles causes different particle image size than its actual. Image of the particles is formed on the camera sensor after passing through a lens between the sensor and the field of view. The size of the particle image, d_i, is influenced by both optical- and diffraction-limited imaging and can be found as

$$d_i = \sqrt{d_{opt}^2 + d_{diff}^2} \tag{2.34}$$

where d_{opt} *and* d_{diff} are the diameter of the particles affected by optical and diffraction-limited imaging, respectively. Diameter due to optical imaging is calculated using the magnification M as

$$d_{opt} = M d_p \tag{2.35}$$

in which magnification is the ratio of the image size (on CCD sensor) to the actual object size. The optical diameter of the particle is small compared with d_{diff} which is estimated as

$$d_{diff} = 2.44 f_{\#}(M+1)\lambda \tag{2.36}$$

while *f/#* is aperture size. Regarding the optimal overall particle image size, it is recommended that d_i should be larger than one pixel in order to avoid peak-locking effect and allow subpixel accuracy in detecting the location of the particles (Raffel *et al.*, 2007). Besides, it is recommended that particle image size should be close to 2×2 pix^2 because extending the sizes is not beneficial because of limited sensor size.

The depth of focus, δ_z, associated with the imaging system can be calculated using

$$\delta_z = 4.88 \left[\frac{f_{\#}(M+1)}{M}\right]^2 \tag{2.37}$$

which should be as thick as the laser sheet thickness to prevent blurred images of the illuminated out of focus particles.

2.3.1.5. Evaluation of particle image motion

The locations of the particles are recorded on the images as peaks in the light intensity. Each pair of successive images is used to evaluate the displacement of the particles. The analysis contains partitioning the images into smaller cells called interrogation windows. The displacement of the particle groups in each interrogation window is acquired using a cross-correlation technique. The recommended particle number for an interrogation window in planar PIV is a minimum of 10

particles (Keane & Adrian, 1992). For the two corresponding interrogation windows *I(x,y,t)* and *I′(x,y,t+Δt),* defined at instants *t* and *t+Δt*, the displacement vector is extracted by the normalized cross-correlation function ∅*,*

$$\emptyset(m,n) = \frac{\sum_{i=1}^{I}\sum_{j=1}^{J} I(i,j)\,.\,I'(i+m,j+n)}{\sqrt{\sum_{i=1}^{I}\sum_{j=1}^{J} I^2(i,j)\,.\,\sum_{i=1}^{I}\sum_{j=1}^{J} I'^2(i,j)}} \tag{2.38}$$

The highest peak value of the correlation map — estimated through sub-pixel interpolation of the peak — pertains to the most probable shift within the interrogation window. The acquired vector presents the particle displacement in pixel space. Dividing the displacement value by the time interval between the image pair yields the velocity in pixels per second. In order to scale the velocity vector, it should be multiplied by the size of the pixel and divided by the optical system magnification.

2.3.2. Tomographic particle image velocimetry

Tomographic PIV is an extension of planar PIV which measures the three components of the velocity vector within a volume. This technique in now known as a powerful method to study turbulent flows (Scarano, 2013). In this section, the fundamental working principles of the tomo-PIV are discussed in terms of the illumination and tracer particles, imaging systems and calibration. Later on, the 3D reconstruction of the volume and the motion analysis are concisely discussed. This section is basically adapted from the review paper of Scarano (2013).

2.3.2.1. Working principles of tomo-PIV

Figure 2.8 schematically illustrates the tomo-PIV experimental setup and data analysis procedure. The flow field is homogeneously seeded with tracer particles and the measurement volume is illuminated by expanding the thickness of the laser sheet. The volume of interest is simultaneously imaged by three or four cameras viewing from different angles. To map the physical space into the images coordinate a complicated calibration procedure, consisting of physical and digital methods, is applied to all the cameras. The recorded images are then processed through an iterative algebraic reconstruction method to reconstruct the three-dimensional light intensity distribution representing the particle field. The volumetric motion

analysis is then conducted through a three-dimensional cross-correlation applied to the pairs of interrogation sub-volumes inside the reconstructed particle field for the two consequent images. This yields a 3D vector field demonstrating the fluid flow within the measurement volume.

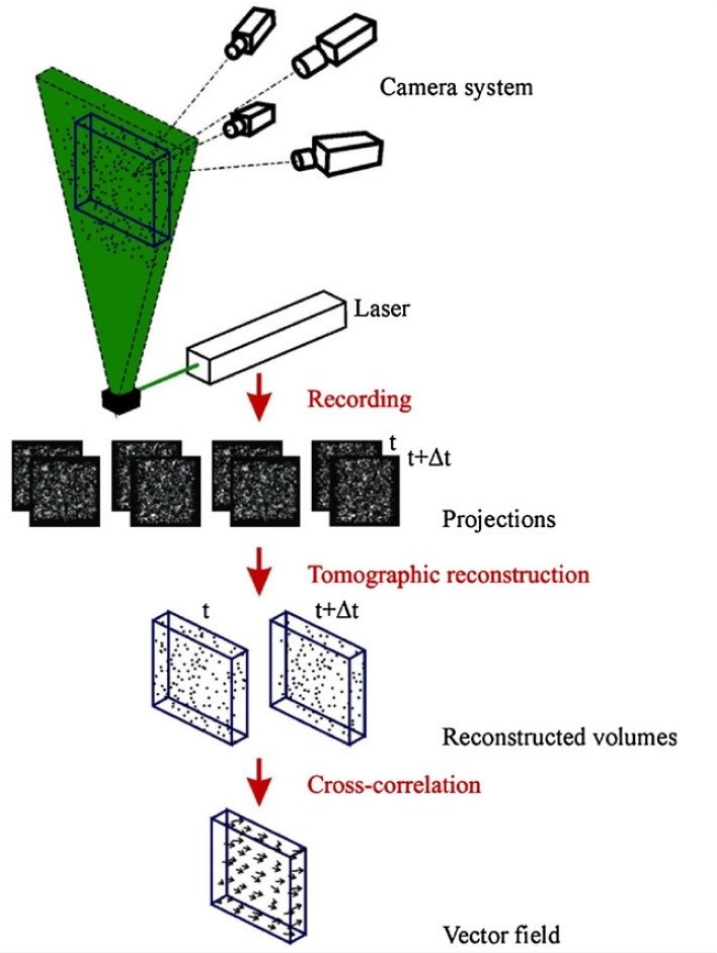

Fig. 2.8. A Schematic illustration of the working principles of tomo-PIV from (Elsinga *et al.*, 2006) reprinted with permission of SPRINGER.

2.3.2.2. Illumination of the measurement volume

Typically, the lasers used for 2C-PIV are used for volume illumination in tomo-PIV, as well. This volumetric illumination is obtained by making an expanded laser sheet using laser sheet optics. The thickness should be set to be roughly equal to the camera depth of field since extra illumination leads to out-of-focus particles which eventually act as noise. For a particular FOV,

the light intensity is inversely proportional to the volume thickness. Moreover, imaging of a thick measurement volume requires operation with small apertures diameter to get deeper depth of focus. Owing to these two considerations the light budget becomes a critical limitation in tomo-PIV.

2.3.2.3. Seeding density

The accuracy of tomo-PIV significantly depends on the tracer particles density. In terms of spatial resolution higher particle number density is preferred since it allows smaller interrogation volumes. On the other hand, high particle number density increases the reconstruction algorithm error. Hence a trade-off is inevitable. According to the study of Elsinga *et al.* (2006), the recommended number density is 0.05 particles per pixel (ppp) for a tomo-PIV system consisting of 4 cameras. Since there is no out of plane motion issues in tomo-PIV, the general rule of thumb of 10 particles per interrogation window is relaxed to 5 to 10 particles per interrogation volume (Scarano, 2013).

2.3.2.4. Imaging system: camera configuration and system calibration

The tomographic imaging is conducted by means of multiple cameras arranged with different configuration with different viewing angles. Scheimpflug adapter is used to align the objective focal plane with the mid plane of the measurement volume. This equipment let the imaging systems operate at wider aperture diameter yielding brighter images. An important parameter is the maximum planar angle β (solid angle) achieved by system of cameras. For a linear system of cameras, as shown in Figure 2.9, accuracy of the reconstruction is maximized for total β in the range of 40° to 80° (Elsinga *et al.*, 2006). Small viewing angle leads to elongated reconstructed particles along the viewing direction and consequently larger error in cross-correlation calculation. On the other hand, larger viewing angle causes higher noise (larger number of ghost particles) in the reconstructed volume arising from the long path of the cameras' line of sight.

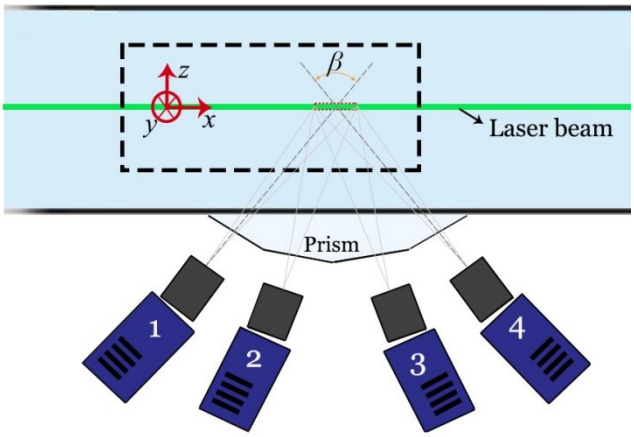

Fig. 2.9. Linear configuration of the cameras.

In order to reconstruct a three-dimensional object from collected 2D images a calibration of digital pixels of the images in the 3D space is needed. The calibration is performed in two steps. In the first step, a target with a particular pattern is imaged at several locations within the depth of the measurement volume. This procedure gives a mapping function relating the pixels coordinates on the camera sensor (x, y) to their projection in the physical space (X, Y) using a third order polynomial. Later, the mapping function is linearly interpolated along the depth direction (Z) between slices where the calibration target is imaged (Ghaemi, 2013).

As the second step, the self-calibration method developed by Wieneke (2008) can be applied to ensembles of images to reduce the calibration errors to a sub-pixel level. In this technique, individual particle images are detected in the images based on an intensity threshold (so, the images should be at lower seeding density of about 0.02 ppp). Next, these identified particles are triangulated into a best-fit location in the three-dimensional space (X, Y, Z) based on all images. Defining (x_i', y_i') as the projection of this best-fit location (X, Y, Z) back into the image plane of ith camera the disparity is calculated as the difference between the projected position (x_i, y_i) and the imaged position (x_i', y_i'). The disparity map is applied to correct the mapping function. This self-calibration procedure is repeatedly performed till the disparity level is reduced to below 0.1 pixel.

2.3.2.5. 3D reconstruction and motion analysis

Once the calibration and the mapping function of individual pixels of the imaging sensor in the three-dimensional space is established, a 3D reconstruction algorithm is applied to obtain the

tracer particle distribution in the volume. This algorithm provides the three dimensional intensity distribution of the particles from the 2D images. For each image recorded from different viewing angles, the light intensity projection on each individual sensor pixel (x_i, y_i) can be represented in the form of an intensity distribution function I (x_i, y_i). The produced 3D reconstructed object, formed of voxels in physical space (X, Y, Z), has a light intensity distribution of E (X, Y, Z) which represents the relative position of the tracer particles in the measurement volume. The relationship between E and I is as follows

$$\sum_{j\in N_i} w_{i,j}\, E\left(X_j, Y_j, Z_j\right) = I(x_i, y_i) \tag{2.39}$$

In which N_i is the number of voxels in the line of sight of the (x_i, y_i) pixel (shaded voxels in Figure 2.10) and $w_{i,j}$ is the weighting coefficient of the contribution of the jth voxel to the ith pixel intensity (x_i, y_i). Figure 2.10 schematically represents the imaging model used for tomographic reconstruction. The 3D intensity field E (X, Y, Z) is acquired through iterative multiplicative algebraic reconstruction technique (MART). Then, the resulted successive reconstructed objects (3D intensity fields) are subject to 3D cross-correlation with multigrid yielding the instantaneous velocity vector field (Ghaemi, 2013).

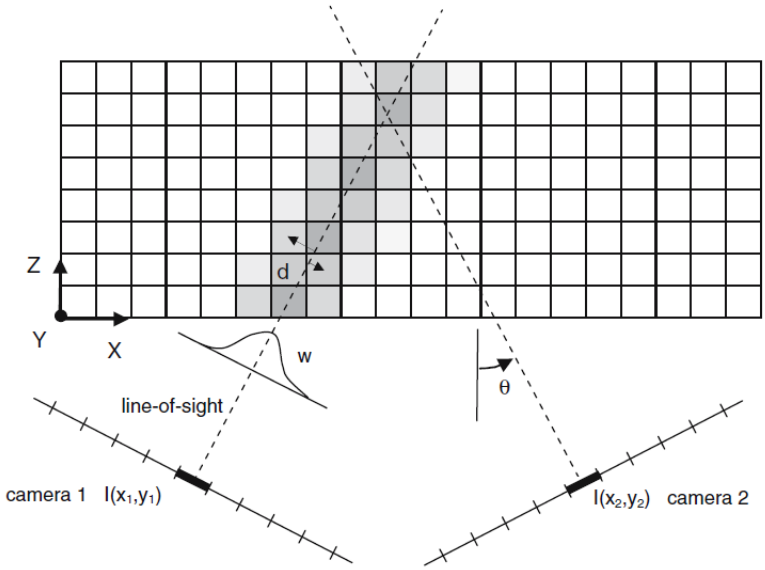

Fig. 2.10. "Object discretization and imaging model used for tomographic reconstruction. The voxels falling within the shaded stripe (weighted cross section) have nonzero value of the weighting coefficient $w_{i,j}$" from (Elsinga *et al.*, 2006) reprinted with permission of SPRINGER..

3. Experimental procedure

In this chapter, three particular experiments with specific goals are described. The first experiment is associated with measurement of the turbulent channel flow over wetted and non-wetted SHO surface. In this experiment, two planar-PIV configurations are used to obtain the turbulent flow statistics. The drawbacks of this system were diagnosed to improve the second experimental setup and measurement systems. In second experiment, the planar PIV measurement is followed by long-range micro-PTV measurement of the near-wall flow as the main objective. Third experiment pertains to the evaluation of three-dimensional measurement of the channel flow using tomographic PIV and 3D-PTV methods.

3.1. PIV measurement of turbulent flow over superhydrophobic surface

3.1.1. Flow facility

A closed-loop water channel at the Department of Mechanical Engineering of the University of Alberta is used for the experiments. The water channel has a rectangular test section of 0.68 m wide, 0.47 m deep, and 5.2 m long made out of glass walls. The channel is operated with a water depth of D = 420 mm in the current experiments. A flat-plate model with 3 m length made of cast acrylic with an elliptical leading edge and a sharp trailing-edge is placed parallel to the

channel side-wall at a distance of W=50 mm to generate a channel flow as shown in figure 3.1. The measurements are carried out in this rather large facility to improve the measurement spatial resolution in comparison with the previous works of Daniello *et al.* (2009) and Woolford *et al.* (2009) which the latter used a spatial resolution of 12 wall units. The upper surface of the channel is also covered with an acrylic surface resulting in a rectangular channel with no free surface and an aspect ratio of D/W = 8.4. The measurement region is located 2 m (40W) downstream of the leading edge over a replaceable module, 50 cm long (x-direction) and 32 cm wide (z-direction), to incorporate the SHO (wetted and non-wetted) and smooth surfaces.

The experiments are carried out at an average velocity of U_b = 0.154 m/s corresponding to Re = 9,600 based on W. Two tripping wires are also installed 0.2m downstream of the leading edge to ensure a uniform transition to turbulence along the z-direction. The mean velocity profile is symmetric at the measurement region with maximum velocity of U_{max}= 0.177 m/s at the centerline (smooth walls on both sides) and the flowrate is checked continuously by means of a pressure transducer for ascertaining the constant flow rate.

3.1.2. Fabrication and characterization of SHO samples

A random surface structure comprised of a hierarchy of micro and nano-particles was fabricated using spray coating (Ross Nanotechnology). The surface of the acrylic module was cleaned with ethanol to facilitate the adhesion of the SHO coating. An acrylic-based polymer solution was sprayed as a binding layer on the substrate followed by deposition of a mixture of micro and nano-particles in ethanol through a spray-coating procedure. After the solvent evaporates, the micro-particles form the large roughness features of the surface while the nano-particles stick to these structures and form a hierarchy to enhance the hydrophobicity (Aljallis *et al.*, 2013). This hierarchical roughness in conjunction with the intrinsic hydrophobicity of the particles deters the water from wetting the solid surface. Therefore, air pockets are trapped in the micro/nano pores of the surface. To investigate the consequences of the depletion of the air pockets from the SHO surface, another SHO surface produced with similar procedure was wetted using an aqueous solution of a surfactant. The addition of the surfactant reduces water surface tension and results in a wetted surface. The wetted SHO surface is transparent both inside and outside of the water channel, which clearly distinguishes it from the non-wetted surface during the experiments. The

contact angle (CA) of the non-wetted SHO is evaluated using the Krüss DSA 100 system (Krüss GmbH, Hamburg, Germany). Because of the low surface energy of the SHO coating, the droplet did not detach from the dispenser needle showing a minimum CA of 165°.

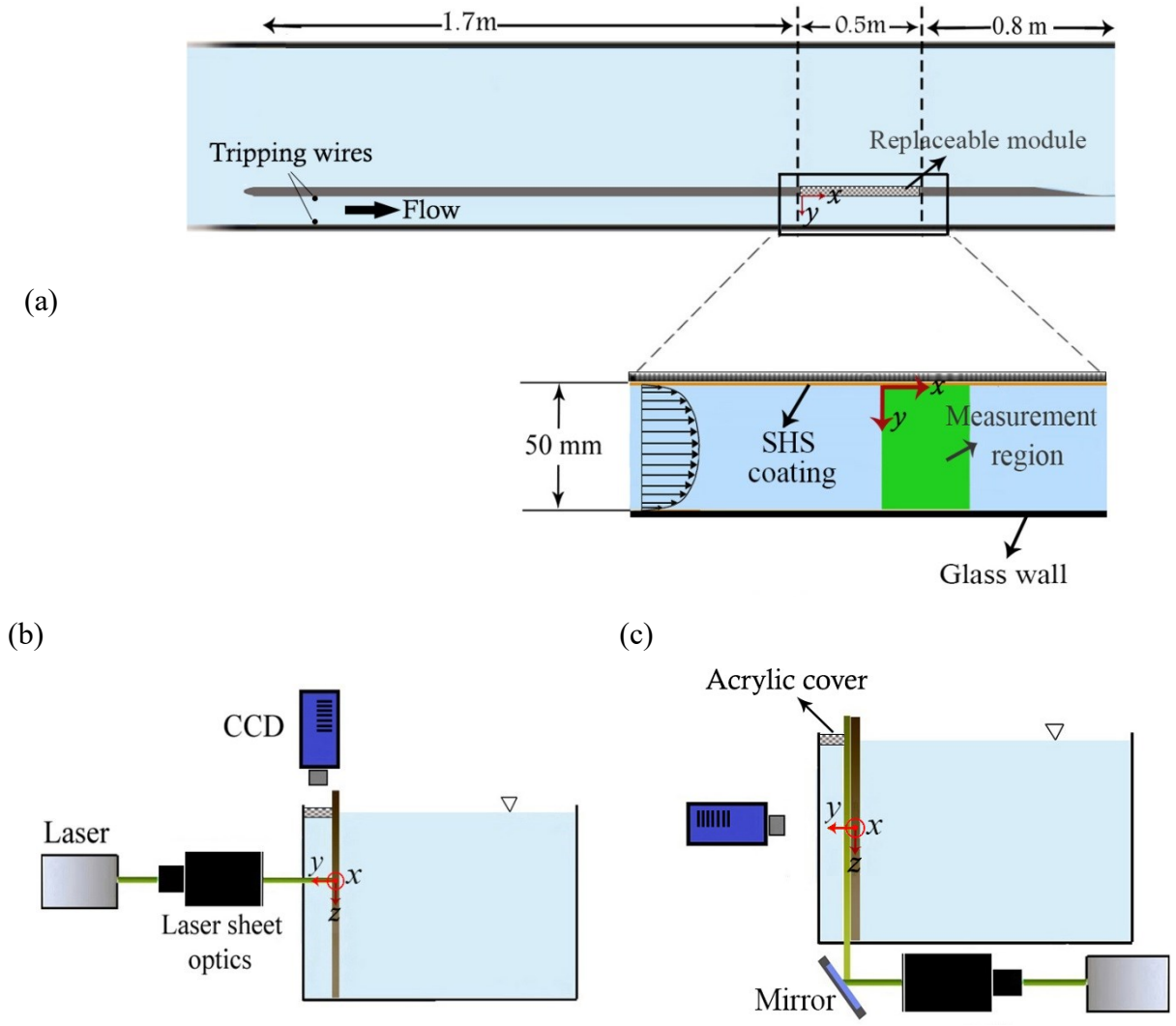

Fig. 3.1. A schematic view of the experimental setup showing (a) a top view of the channel flow formed between the flat-plat and the side wall of the water channel. (b) The arrangement of the camera and the illumination of the PIV system for the wall-normal/streamwise field-of-view (side view) and (c) the arrangement for the spanwise/streamwise field-of-view (side view).

The profile of surface roughness of the SHO surface was measured using Ambios XP-300 surface profilometer with a resolution of 0.1 μm in wall normal direction. Five linear profiles were taken over a sampling length of 10 mm and the data were digitized at a sampling interval of

0.8 μm along the surface. A high-pass filter is applied to remove the inclination of the sample profile. Figure 3.2.a depicts a measured profile of the SHO surface. Three parameters are used to characterize the roughness profile (details in Appendix A). The surface roughness R_a, also known as arithmetic roughness (Farshad & Pesacreta, 2003), is found to be 7.9 μm. The average root-mean-square height, R_{rms}, of the roughness profiles is 10.2 μm with a skewness of 0.66. The mean peak to trough roughness height, R_{PT}, which is a representative of the equivalent sand-grain roughness(Farshad & Pesacreta, 2003), is 41 μm. The normalized form of these statistically calculated equivalent roughness measures are also illustrated in figure 3.2.a. k^+ is defined as R_a $u_{\tau 0}/\upsilon$, where $u_\tau = \sqrt{\tau_0/\rho}$ is the friction velocity, τ_0 is the shear stress on the smooth wall, ρ is the density, and υ is the kinematic viscosity of water. Based on all the roughness parameters shown in figure 3.2.a, the size of the surface features of the SHO surface used in the present work is almost one order of magnitude smaller than viscous sublayer thickness ($y^+ = 5$) in the current experiment. Therefore, if the air pockets are depleted the wetted surface is hydrodynamically smooth. Owing to the random nature of the current roughness, there might be sporadic wetted surface protrusions in contact with the liquid phase. This can be a drawback of the randomly-textured SHO surfaces which depending on the size of these protrusions reduces the friction reduction effect. For a wetted SHO surface, the roughness elements coming into direct contact with water flow increase the wetted area compared to the smooth surface. However, any changes to bulk flow depend on the relative roughness size to the flow length scale. Figure 3.2.b presents photographs of the wetted and non-wetted SHO surfaces submerged in still water. The wetted SHO surface is transparent while the non-wetted SHO the entrapped air pockets make an opaque surface. The transparency of the wetted surface and the opaqueness of the non-wetted surface were maintained throughout the experiments as the surfaces were submerged in the water channel.

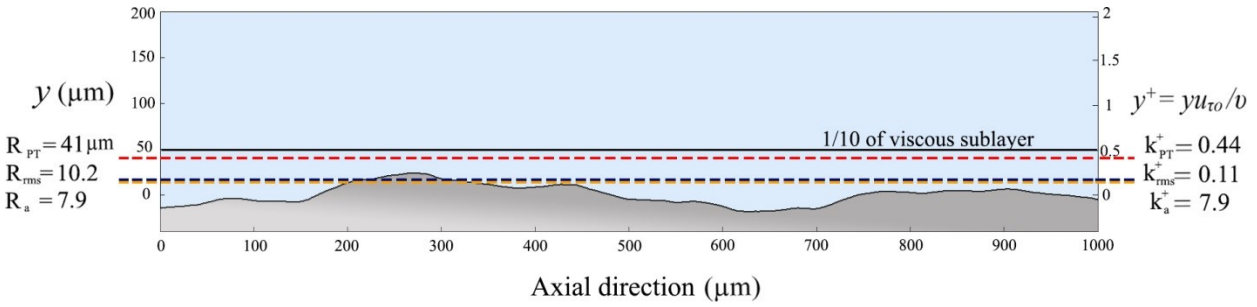

(a)

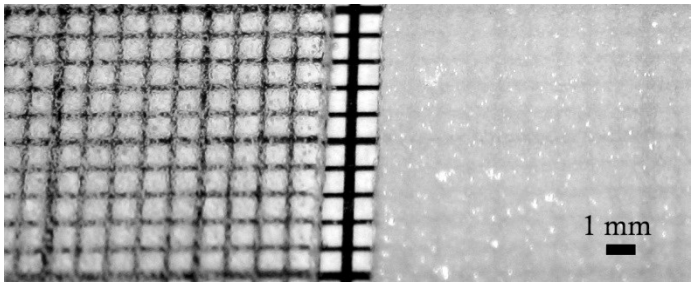

(b)

Fig. 3.2. a) The surface profile of SHO surface obtained from profilometery. The vertical axis on the left presents the roughness in μm while the dimensions normalized by inner scaling are shown on the right axis. Normalization is done by $u_{\tau 0}$ obtained from PIV experiments on the smooth surface. b) Photograph of the wetted (on the left) and non-wetted (on the right) SHO surfaces submerged in still water with a graph paper in the background. Light passes through the wetted SHO making the background grid visible, whereas for the non-wetted SHO the entrapped air pockets hinder the light passage.

3.1.3. Particle image velocimetry

Detailed characterization of the turbulent channel flow over the surfaces is carried out using two planar PIV configurations. The first field-of-view (FOV1), shown in figure 3.3.a, has a wall-normal/streamwise plane to capture the profile of mean velocity and the turbulent statistics in the wall-normal direction. The second field-of-view (FOV2), shown in figure 3.3.b, records spanwise/streamwise PIV images to scrutinize the low and high speed streaks within the inner layer. A schematic of both configurations is available in figures 3.1.b and 3.1.c.

The illumination for the PIV experiment was provided by a dual-cavity Nd-YAG laser (QUANTARAY PIV-400) with maximum output of 400 mJ/pulse and a wavelength of 532 nm. The laser has maximum operation frequency of 10 Hz and a pulse width of 5-8 ns. The laser initial beam diameter is 9 mm at the output which is collimated into a laser sheet of 30 mm wide and 1 mm thick. The water channel has been seeded with 12 μm hollow glass spheres (Potters

Industries Sphericel® 110P8). A CCD camera with a sensor size of 2048×2048 pixel and 14 bit resolution (Imager ProX, LaVision) is applied to capture the images. Each pixel has 7.4 μm×7.4 μm area. A calibration target is used to establish the relation between the image coordinates and the physical space. The camera is equipped with a 105 mm SLR lens with an aperture setting of f / 5.6. For each data set 10,000 images were recorded with Δt = 1000 μs. Detailed information about the imaging system of the two PIV configurations is available in Table 3.1.

The PIV images are improved for the cross-correlation algorithm by subtracting the ensemble minimum from the individual images. The images are further normalized by the ensemble average of the recordings. The mean velocity profile is obtained by averaging the cross-correlations over the ensemble of recordings (Kähler *et al.*, 2012; Meinhart *et al.*, 2000). This method increases the signal-to-noise ratio which allows a higher spatial resolution by allowing a smaller Gaussian interrogation window (IW) of 12×12 pixels with 75% overlap elongated with 4:1 aspect ratio in the streamwise direction. The instantaneous velocity fields for statistical investigation of the turbulent flow are obtained from cross-correlation of individual image pairs with IW of 48×48 pixels and 75% overlap. Similar processing algorithm with 48×48 pixels and 75% overlap was also applied to FOV2 images. The vector fields are post processed by universal outlier detection (Westerweel & Scarano, 2005) and limiting the allowable vector range to -0.03 to +0.03 m/s for wall normal and 0 to 0.2 m/s for streamwise velocity. The PIV processing of all data sets are conducted in DaVis 8.2 (LaVision, GmbH). Detailed processing procedure is discussed in Appendix B.

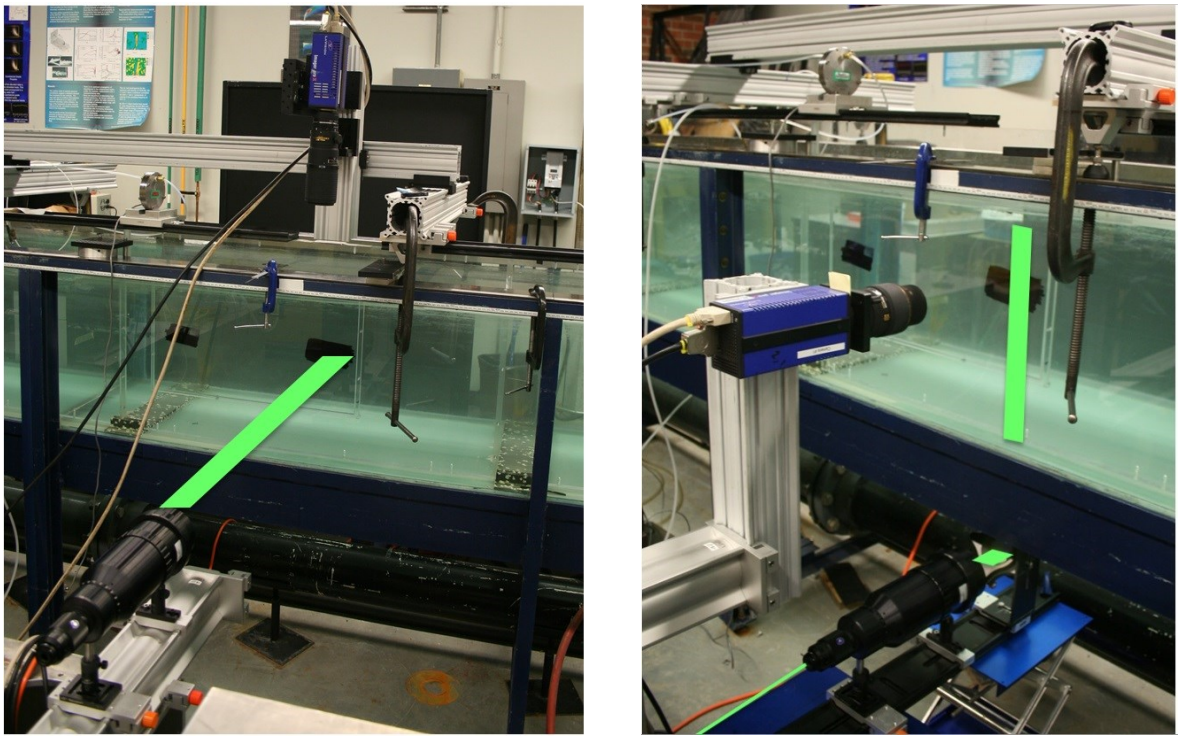

(a) (b)

Fig. 3.3. Photos of the each PIV configuration, a) wall-normal/streamwise, b) spanwise/streamwise field of view. The laser sheet trajectory is shown.

Table 3.1. System specifications of the two planar PIV measurement configurations. The wall unit of λ_0 = 92 μm associated with the smooth surface is used to normalize the dimensions.

	FOV1		FOV2
Orientation	Wall-normal/streamwise		Spanwise/streamwise
Magnification	0.29		0.51
Digital resolution	38.6 pixel mm^{-1}		56.3 pixel mm^{-1}
Measurement field	2048 × 2048 pixels 53 mm × 53 mm $576^+ \times 576^+$		2048 × 2048 pixels 28.6 mm × 28.6 mm $310^+ \times 310^+$
Velocity vector	Individual correlation	Ensemble of correlations	Individual correlation
Interrogation window (IW)	48 × 48 pixels 1.24 mm × 1.24 mm $13.6^+ \times 13.6^+$	12 × 12 pixels 0.31 mm × 0.31 mm $3.4^+ \times 3.4^+$	48 × 48 pixels 0.85 mm × 0.85 mm $9.24^+ \times 9.24^+$
IW overlap	75 %	75 %	75 %
Vectors per field	170 × 170	680 × 680	134 × 134

3.2. Near-wall flow measurement using long-range micro-PTV

Here, the problems encountered during the first experiment (section 3.1) are introduced and the measures taken in order to resolve them are discussed. The ultimate goal, here, is to conduct a long-range micro-PTV measurement. To this end, the imaging quality is improved and a fully-developed turbulent channel flow is ascertained with optimizing the geometry of the flow. First the changes to the flow setup are described. Then, the changes applied to illumination and seeding procedure are discussed. The 2C-PIV measurement, performed to obtain general information regarding the turbulent flow across the channel, is described and finally the high-magnification PTV system is discussed.

3.2.1. Improvements to the experimental setup

During the first experiment, the major and minor shortcomings associated with the flow facility and measurement system were recognized and necessary changes were made to amend the experiment accuracy. These shortcomings and the corresponding improvements are concisely overviewed here and the details are presented subsequently.

- Fully development of the flow: in order to further ascertain the fully development of the flow the length to width (wall-normal dimension) ratio and the channel depth (spanwise dimension) to width ratio are increased significantly (details in section 3.2.2).
- Flow entrance: to tackle the flow asymmetry problem a honeycomb grid is installed to further uniform the flow. Besides, the channel flow is formed by placing two parallel plates with a distance from the water channel wall. This will cause the entrance of the water into the channel flow from the region outside the boundary layer already formed over the water channel wall.
- Plastron light scattering/reflection: in the first experiment, adjacent to the wall, the number density of the tracer particles tended to drop significantly and the reflection from the air plastron over SHO surface imposes additional noise to image background which is due to the fact that the laser sheet was directed perpendicularly to the channel wall. To solve this issue, the laser sheeting process is conducted just before entering the water channel and subsequently, the laser sheet is directed in the streamwise direction (parallel

to the channel walls) using a mirror placed inside the water channel far downstream of the measurement region. By this illumination technique, the laser sheet travels parallel to streamwise direction eliminating the reflections attributed to the incident to the SHO surface (further details are provided in section 3.2.3).

- Seeding particles: to achieve higher image contrast, the particles are changed to silver-coated glass sphere which scatter significantly more light than the ordinary glass sphere particles.

3.2.2. Flow facility

The closed-loop water channel at the Department of Mechanical Engineering of the University of Alberta as detailed in section 3.1.1 is used. The channel is operated at water depth of D = 230 mm in the current experiments. A 3 m long flat glass plate was placed parallel to the channel bottom wall at a distance of 20 mm. A flat-plate model with 3 m length made of cast acrylic with an elliptical leading edge and a sharp trailing-edge is placed parallel to the glass plate at a distance of W = 20 mm to generate a channel flow with an aspect ratio of D/W = 8.4 (figure 3.4.a). These plates are placed at a 30 mm distance from the water channel bottom wall in order to avoid the turbulent boundary layer already formed over it so that any flow asymmetry would be circumvented. The measurements are carried out in this rather large facility to improve the measurement spatial resolution in comparison with the previous works (Daniello *et al.*, 2009; Woolford, Prince, *et al.*, 2009). The measurement region is located 2 m (100W) downstream of the leading edge over a replaceable module, 50 cm long (x-direction) and 32 cm wide (z-direction), to incorporate the SHO and smooth surfaces. The experiments are carried out at an average velocity of U_b = 0.21 m/s corresponding to Re = 5,236 based on W. At the entrance, a honeycomb grid is installed to ensure symmetry of the channel. The mean velocity profile is symmetric at the measurement region with maximum velocity of U_{max}= 0.243 m/s at the centerline (smooth walls on both sides). Optimization of the channel geometry is also considered. To further ascertain the fully-development of the channel flow, the length to width (wall-normal dimension) ratio is increased from 40 to 100. This will further let the flow to develop and to become more symmetric as well as letting the flow reach to equilibrium in the

presence of SHO surface. The channel depth (spanwise dimension) to width ratio is also increased from 8.4 to 21 to further decrease the corner flow effects.

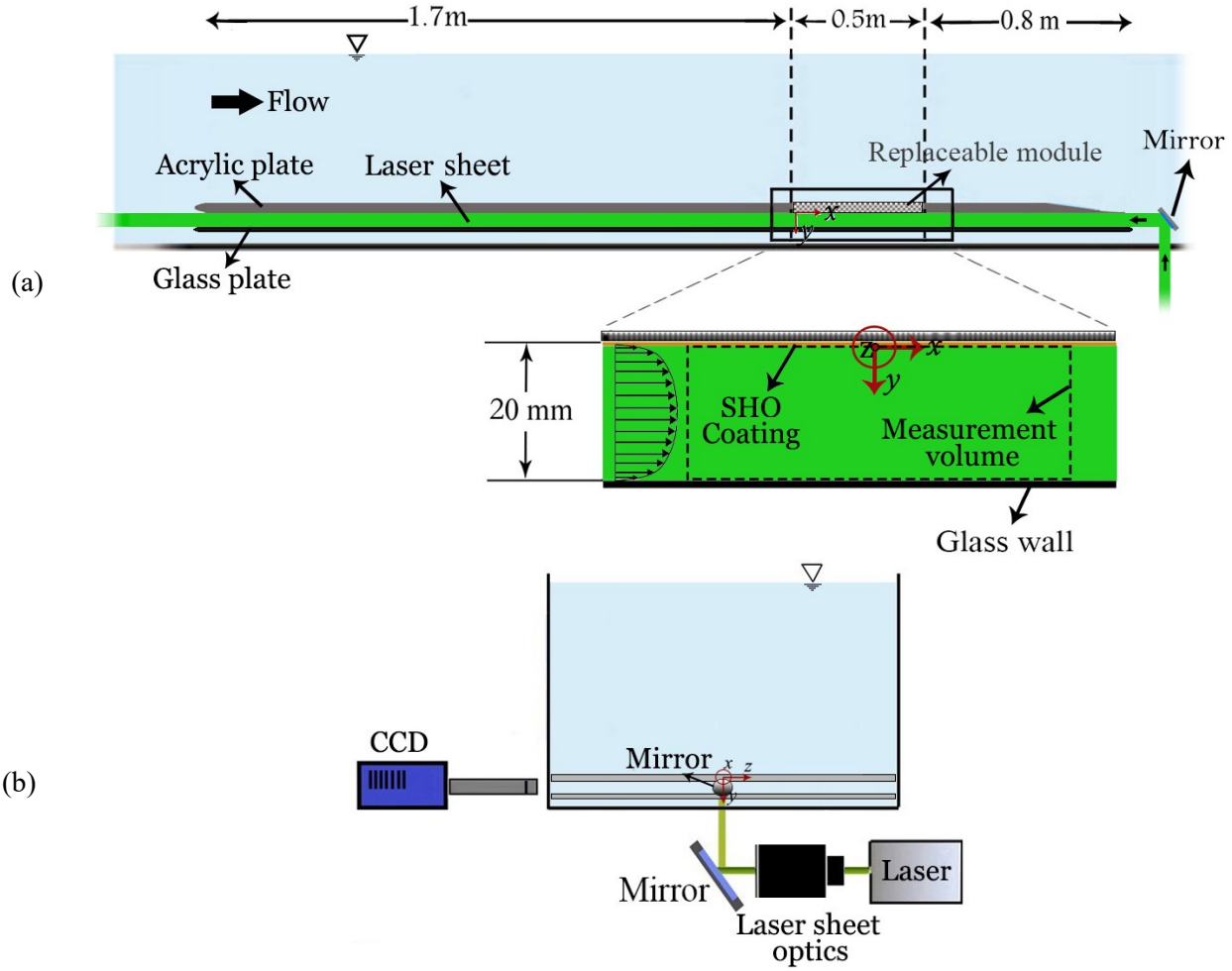

Fig. 3.4. A schematic view of the experimental setup showing (a) a front view of the channel flow formed between the flat-plat and the glass plate in the water channel. (b) The arrangement of the camera and the illumination of the PIV system for the wall-normal/streamwise field-of-view (side view)

3.2.3. Planar PIV

The planar PIV configuration in this experiment has a wall-normal/streamwise field-of-view plane to capture the profile of mean velocity and the turbulent statistics in the wall-normal direction. A schematic of the setup is available in figure 3.4.b.

In image-based velocimetry measurements, the quality of the recorded images plays the key role in the measurement accuracy. Measurement in the proximity of the wall has always been a

challenge as the number density of the tracers diminishes significantly and reflection from the wall imposes additional noise to image background deteriorating the overall performance of the measurement system. In the first set of experiments, the laser beam was directed perpendicularly to the channel wall (laser sheet travelled in wall-normal direction) as shown in figure 3.3.a. As expected, the incident of laser beam to the smooth acrylic surface would cause laser light reflection. In the case of SHO surface, due to presence of an air plastron on top of an opaque non-light-transmitting material the reflection escalates resulting in a glare which decreases the signal-to-noise ratio especially in near-wall region. The effect of this phenomenon is manifest in figure 3.5.a. The quality of the image in near-wall region is lower than other areas leading to unreliable velocity vectors.

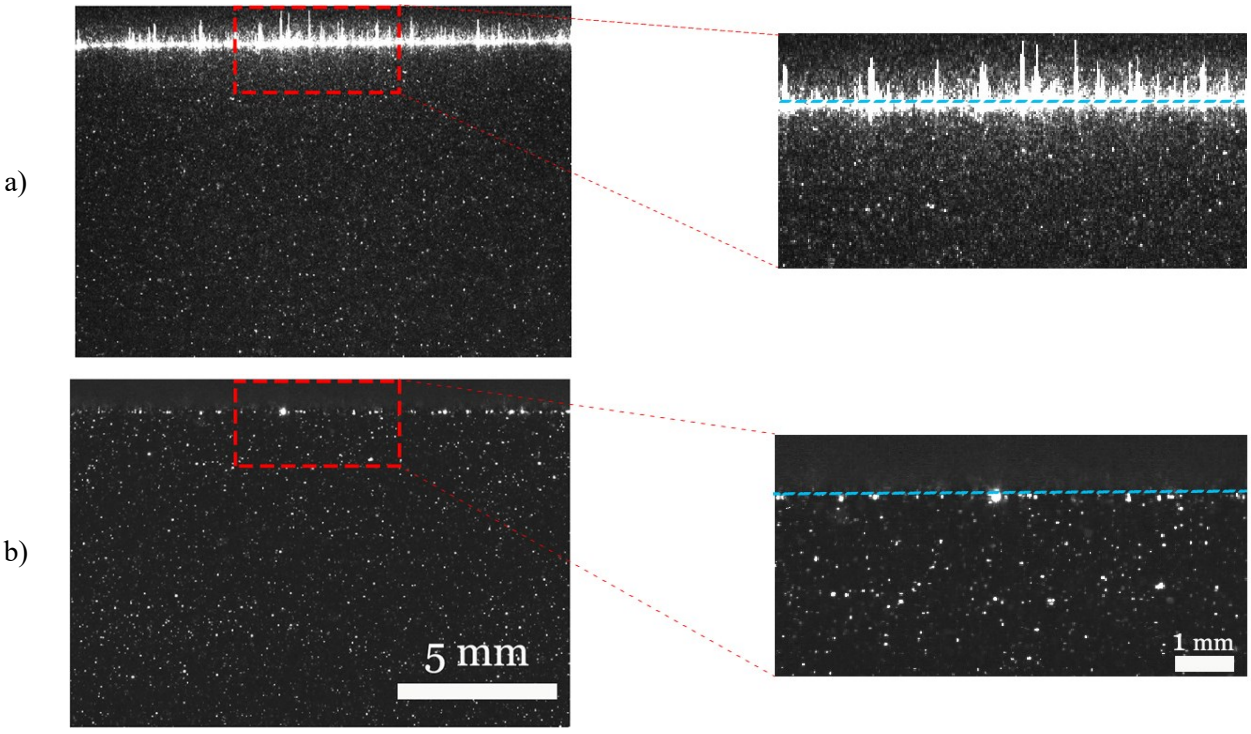

Fig. 3.5. Image quality in the proximity of the SHO wall. a) laser beam directed perpendicularly to the channel wall with hollow glass spheres as tracers, b) laser beam directed along the streamwise direction with silver-coated glass spheres as tracers.

This problem is tackled by optimizing two of the main factors in PIV: illumination and flow seeding. To fix the reflection problem, the laser beam is transformed into a collimated laser sheet using a combination of cylindrical optics just before entering the water channel. Then, the laser

sheet is directed in the streamwise direction parallel to the channel walls using a mirror placed inside the water channel. Far downstream of the measurement region (1.2 m), this mirror is sealed inside a square acrylic tube (50 mm× 50 mm). This configuration provides a laser beam with the same width as the channel which travels parallel to streamwise direction and reduces reflection since the laser sheet does not hit the SHO surface. To further improve the particle image quality the tracer particles are altered from 12 μm hollow glass spheres to 2 μm silver-coated glass spheres (Potters Industries Conduct-O-Fil® SG02S40) which considerably increases the light scattering efficiency. The particles Stokes numbers ratio of 0.36 proves that the fidelity to flow is still acceptable. The results of these measures are evident in figure 3.5.b. The contrast in the image has increased significantly due to lower background noise and brighter particles. The zoomed images of the near-wall regions also indicate that the reflection is noticeably attenuated leading to capturing higher number of tracer particles. To check the possible effects of the mirror inside the flow, the compliance of the mean velocity profile with fully-developed channel results is examined which is discussed in chapter 5. A calibration target is used to establish the relation between the image coordinates and the physical space. The camera is equipped with a 105 mm SLR lens with an aperture setting of f / 5.6. For each data set 10,000 images were recorded with Δt = 900 μs for statistical convergence. Detailed information about the imaging system of the two PIV setups is available in Table 3.2.

The PIV images are improved for the cross-correlation algorithm by subtracting the ensemble minimum from the individual images. The images are further normalized by the ensemble average of the recordings. The mean velocity profile is obtained by averaging the cross-correlations over the ensemble of recordings (Kähler *et al.*, 2012; Meinhart *et al.*, 2000). This method increases the signal-to-noise ratio which allows a higher spatial resolution by allowing a smaller Gaussian interrogation window (IW) of 12×12 pixels with 75% overlap elongated with 4:1 aspect ratio in the streamwise direction. The instantaneous velocity fields for statistical investigation of the turbulent flow are obtained from cross-correlation of individual image pairs with IW of 32×32 pixels and 75% overlap. The vector fields are post processed by universal outlier detection (Westerweel & Scarano, 2005) and limiting the allowable vector range to -0.05 to +0.05 m/s for wall normal and 0 to 0.4 m/s for streamwise velocity. The PIV processing of all data sets are conducted in DaVis 8.2.3 (LaVision, GmbH).

3.2.4. Long-range micro-PTV

Detailed characterization of the near-wall turbulent channel flow over the surfaces is carried out using high magnification two-dimensional PTV technique. The wall-normal/streamwise FOV is recorded to capture the profile of mean velocity and the turbulent statistics in viscous sub-layer and the buffer layer. A schematic of the setup is available in figures 3.4.a-b.

The illumination and seeding is done similar to 2C-PIV experiment of section 3.2.3. Similar calibration procedure to the first experiment is conducted. The camera is equipped with a Navitar zoom lens to obtain a magnification of $M = 1.83$. For each data set 15,000 images were recorded with $\Delta t = 200$ μs. The achieved field of view is 8.2×8.2 mm^2 with digital resolution of 248 pixel mm^{-1}.

The images are improved for the PTV algorithm by subtracting the ensemble minimum from the individual images. The average vector field obtained through the ensemble of correlation (sum-of-correlation) technique is used as the initial displacement value to detect the particle pairs. An in-house PTV code, developed in MATLAB, that initially detects particles based on a preliminary intensity threshold followed by local maximum detection is used. In cases with high magnification, the diffraction pattern of the particles becomes discernable since it introduces a group of local maxima close to each other. The particles with this problem are expelled. The large particles rendering changing shapes within the consecutive images are also removed. Kähler *et al.* (2012a) proved that particles below 3 pixels in diameter might cause the biased error due to the peak locking. To resolve this, an area filter is applied to find pairs of particles within the range of 3-7 pixels in diameter. To achieve sub-pixel accuracy, a Gaussian filter is applied to the detected particles. As the final filtering step, the particles at the borders in streamwise direction are eliminated to decrease the noise level. The resultant velocity vectors are post-processed by limiting the wall-normal velocity fluctuations to 20 % of the streamwise fluctuation. The PTV results are averaged within 6 pixel sub-regions in wall-normal direction for statistical convergence.

3.3. 3D flow measurement

3D measurement can unravel the mechanism of turbulence production by providing a thorough picture of the turbulent flow statistics. In addition to streamwise and wall-normal directions, measurement of the changes in spanwise fluctuations due to changes in the wall boundary condition will decipher the interaction between different flow structures leading to possible skin-friction reduction. Three-dimensional measurements provide the volumetric flow field information giving us the capability of conducting comprehensive vortex analysis. Here, two three-dimensional techniques are utilized for this purpose. First the tomographic PIV is described and next the 3D-PTV technique is discussed.

3.3.1. Tomographic PIV

Tomographic PIV provides a three-dimensional vector field representing the flow field and is helpful in characterizing the 3D coherent structures. In the tomo-PIV system used in the current experiment, the volume of interest was illuminated with a laser beam of 20 mm wide and 4 mm thick. The imaging system consists of four Image pro X (4MP) cameras arranged in a linear configuration as shown in figure 3.6.a and 3.6.b. Cameras 1 and 4 (cameras on sides) are inclined making a $\beta = 80°$ angle and cameras 2 and 3 (cameras in the middle) make a 35° angle. 105 mm objectives are attached to cameras with Scheimpflug adapters in between. The aperture of all the cameras is set to $f/16$. The cameras looked through a prism containing water. The achieved measurement volume is 45.4 mm × 20 mm × 3.5 mm. The flow has been seeded with the 2 µm particles with a concentration of 24 particles mm^{-3}. 400 images are collected with $\Delta t = 1200$ µs.

The preprocessing procedure consists of subtracting the minimum value of each pixel along the sequence, the removal of the residual background intensity by subtracting the sliding minimum with kernel of 3 pixels and the image intensity normalization by the average over a kernel of 300 pixels. A constant value was subtracted from each pixel to decrease the background level to zero. The volume reconstruction is done with 51 mm × 30 mm × 7.5 mm dimensions in streamwise (x), wall-normal (y) and spanwise (z) coordinates respectively, discretized at 42.9 voxels mm^{-1}. Interrogation volumes of 40 × 40 × 40 voxels with 75% overlap have been selected. Adopting a multi-grid volume deformation method the volumetric cross-correlation is performed to acquire

the velocity vector field. The volumetric vector field has 195 × 127 × 15 vectors with spacing of 0.233 mm.

Table 3.2. System specifications of the two PIV measurement setups used in sections 3.2-3. The wall unit of λ_0 = 68 μm associated with the smooth surface is used to normalize the dimensions.

	2C-PIV (section 3.2.3)		Tomo-PIV
Magnification	0.42		0.31
Digital resolution	55.3 pixel mm^{-1}		42.9 pixel mm^{-1}
Measurement field	1975 × 1365 pixels 33.7 mm × 23.7 mm $495^+ \times 348^+$		45.4 mm × 20 mm × 3.5 mm $668^+ \times 294^+ \times 52^+$
Velocity vector	Individual correlation	Ensemble of correlations	Individual correlation
Interrogation window (IW)	32 × 32 pixels 0.58 mm × 0.58 mm $8.5^+ \times 8.5^+$	8 × 8 pixels 0.146 mm × 0.146 mm $2.1^+ \times 2.1^+$	40 × 40 × 40 voxels 0.93 × 0.93 × 0.93 mm^3 $13.7^+ \times 13.7^+ \times 13.7^+$
IW overlap	75 %	75 %	75 %
Vectors per field	163 × 141	142 × 560	195 × 127 × 15

Table 3.3. System specifications of the two PTV measurement setups used. The wall unit of λ_0 = 68 μm associated with the smooth surface is used to normalize the dimensions.

	Long-range micro-PTV	3D-PTV
Magnification	1.83	0.31
Digital resolution	248 pixel mm^{-1}	42.9 pixel mm^{-1}
Measurement field	2048 × 2048 pixels 8.2 mm × 8.2 mm $120^+ \times 120^+$	45.4 mm × 20 mm × 3.5 mm $668^+ \times 294^+ \times 52^+$
Spatial resolution (Averaging window/bin size)	6 × 6 pixels 0.024 mm × 0.024 mm $0.35^+ \times 0.35^+$	6 × 6 × 6 voxels 0.14 × 0.14 × 0.14 mm^3 $2.05^+ \times 2.05^+ \times 2.05^+$
Vectors per field	343 × 343	326 × 210 × 25

3.3.2. 3D Particle tracking velocimetry

In 3D-PTV technique, the individual particles in the three-dimensional volume are detected and tracked. This in turn, provides higher resolution compared to tomo-PIV on condition that sufficient number of images are collected to have the statistics converge. There are two possible ways to estimate the 3D location of the individual particles. In the first method, similar to tomo-PIV, MART algorithm can be adopted which subsequently warrants development of a particle tracking program. The second technique is based on the triangulation of intensity distribution which has been recently added to DaVis. In the current work, the 3D-PTV algorithm of DaVis 8.2.3 (reconstruction based on the triangulation) is applied to the double-frame images collected with the same setup used for tomo-PIV measurement. Similar mapping function obtained from the physical and self-calibration of the Tomo-PIV is applied. DaVis allows changing of only two processing parameters namely, particle intensity threshold and allowed triangulation error on the accuracy of results. Miscellaneous processing investigations were carried out in the form of trial and error to find the optimal processing parameters. Going to smaller triangulation errors could lead to more accurate results, however, it reduces the number of detected particles. This problem can be tackled by either lowering the intensity threshold as a compromise or collecting more images to have the statistics converge. Another limiting factor is the number of particles per each averaging bin. Detecting higher number of particles results in higher spatial resolution attributed to smaller averaging bins. 4000 images are collected with similar settings to tomo-PIV case except for the lower seeding density of 21 particles mm^{-3}. The maximum triangulation error was set 1 pixel for particle intensity threshold of 40 counts. 6×6×6 pixel averaging bins are selected allowing for Eulerian study of the flow. The details can be find in Table 3.3.

(a)

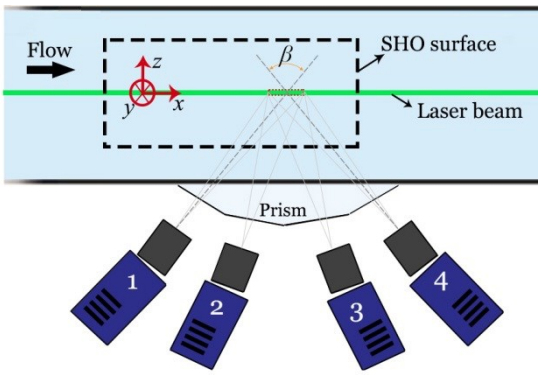

(b)

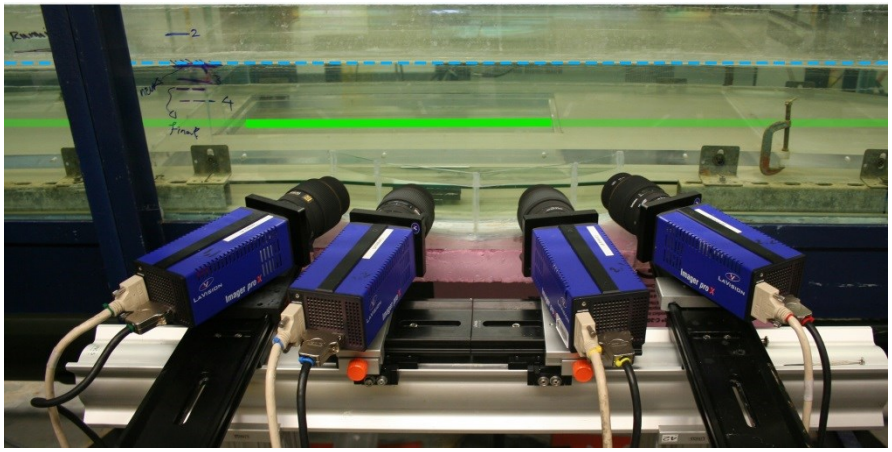

Fig. 3.6. a) A schematic illustration of the arrangement of the cameras for the tomographic PIV (top view), b) a photo of the tomographic PIV setup. The laser sheet trajectory is also depicted.

4. Turbulent flow over wetted and non-wetted superhydrophobic counterparts with random structure

The turbulent structure of the inner layer of a turbulent channel flow over a non-wetted superhydrophobic (SHO) surface with random pattern produced by spray coating is experimentally investigated at Re = 9,600. The results are compared with the wetted counterpart and also a smooth surface. Two planar particle image velocimetry (PIV) measurements are carried out in the streamwise/spanwise and streamwise/wall-normal planes. The vector fields are obtained from both ensemble averaging and individual cross-correlations of double-frame images. The results showed a small increase (~5%) of the mean velocity profile at y^+=10 over the non-wetted surface in comparison with the wetted and the smooth surfaces. Up to 15% reduction of normal and shear Reynolds stresses is observed in the inner layer over the non-wetted SHO surface. The wetted SHO counterpart demonstrates no effect on the mean velocity and Reynolds stresses in comparison with the smooth surface. The result confirms the comment of Gad-el-Hak (2013) that the wetted SHO is hydrodynamically smooth if the surface pores are smaller than the viscous sublayer thickness. A noticeable suppression of the sweep and ejection events, increase of the spanwise spacing of the low and high speed streaks, and attenuation of vortical structures are observed over the non-wetted SHO. These indicate attenuation of the

turbulence regeneration cycle due to the slip boundary condition over the non-wetted SHO surfaces with random texture.

4.1. Introduction

The friction force between the turbulent flow and the solid surface is the main source of energy loss in long transmission pipelines. The performance of marine vessels and aircrafts is also limited by the friction force and has prompted interest in drag reduction methods using various active and passive techniques. Hitherto, polymer additives (Christopher M. White & Mungal, 2008), near-wall injection of bubbles (Sanders *et al.*, 2006) and air layer (Elbing *et al.*, 2008) and wall surface modification (Carpenter, 1997; Choi, 2006; Rothstein, 2010a) have been employed. The latter method of surface modification is of particular interest due to no requirement for a supply of polymer or pressurized gas and also the recent advances in micro/nano manufacturing techniques.

One of the latest surface modification techniques is the fabrication of micro/nano size patterns on an intrinsically hydrophobic material. The result is known as the superhydrophobic surface, in which the adhesion force cannot overcome the water surface tension because of the low surface energy of the material. This phenomenon is known as the Cassie state and results in a partially or fully non-wetted surface (Lafuma & Quéré, 2003). At this state, the micro-scale air pockets will be trapped and retain in the pores and voids of the surface forming a plastron. The slip of the liquid flow over this air plastron has the potential to result in a significant reduction of skin friction in both laminar and turbulent wall-bounded flows (Rothstein, 2010a). In terms of surface pattern, SHO surfaces have either ordered or random structures.

The SHO surfaces with ordered patterns are mostly fabricated through photolithography and soft lithography processes which require nanofabrication facilities and are typically limited to small surface areas (less than 100 cm^2). This has been ideal for experimental investigation of these surfaces for reduction of friction in small-scale laminar flows of microfluidic applications. Among others, the experiments of Ou *et al.* (2004), Joseph *et al.* (2006), and Byun *et al.* (2008) have confirmed significant slip and reduction of skin friction in microchannels which is in agreement with the theoretical model of Lauga and Stone (2003). Investigations of SHO surfaces

with ordered patterns have also been extended to the turbulent regime showing the potential of skin-friction reduction and interaction with the turbulent structures.

In the turbulent regime, the recent experimental study of Park *et al.* (2014) directly measured the skin-friction over a SHO with micro-scale grates using micro-flexure beams and showed up to 75 percent reduction of skin-friction. Other investigations using PIV (Daniello *et al.*, 2009; Woolfor *et al.*, 2009) or pressure drop measurements (Daniello *et al.*, 2009; Jung & Bhushan, 2010) on SHO with patterned structures have also shown about 9-30 percent reduction of skin-friction in low Re number turbulence. The numerical simulation of Min & Kim (2004) showed reduction of skin-friction over a SHO surface represented with only streamwise slip and an increase of skin-friction over a SHO modeled with spanwise slip. These results have confirmed reduction of skin-friction using patterned SHO with nano or micro scale patterns with significant streamwise slip.

The investigation of the turbulent flow over SHO surface by the DNS of Min and Kim (2004) has shown that the effect of SHO surface on the mean velocity profile is extended beyond the viscous sublayer to the buffer and the log layers. Martell *et al.* (2010) showed in a DNS that mean velocity profile near the SHO wall scales with the wall shear stress and the log layer is offset by a slip velocity. The DNS of Jelly *et al.* (2014) over SHO surface with streamwise micro-grooves has shown reduction of the strength of streamwise vortices and also the Reynolds shear stress. These numerical simulations have prescribed a slip boundary condition and obtained both a significant increase of mean velocity and a decrease in turbulent intensities over a wall normal distance extended to the logarithmic layer. However, the PIV experiment of Woolford *et al.* (2009) on a SHO surface with patterned ribs and cavities in the range of 8-23 micron showed negligible change in the mean velocity profile and about 10 percent reduction of streamwise turbulent intensity. The PIV measurement of Daniello *et al.* (2009) reports a large slip velocity of up to 40% of the mean channel velocity over micro-patterned SHO, however, no direct comparison is made with the mean velocity profile over a smooth surface. Further experimental investigation of the turbulent flow over a variety of surface patterns and Reynolds number is required to address the apparent discrepancy.

Despite the promising drag reduction with SHO surfaces with ordered pattern, their application is still constrained because of the complicated small-scale fabrication and low physical durability

(Verho *et al.*, 2011). On the other hand, the SHO surfaces with a random texture have the advantage of large-scale fabrication through spray coating, spin coating or dip coating methods(Brinker, 2008). This feature renders the random SHO surfaces viable for turbulent friction reduction over large surfaces of industrial applications. However, these are only a few experiments over SHO with random texture showing inconsistent trends. The experimental study of Zhao *et al.* (2007) reported no appreciable decrease of skin-friction in turbulent flow over a flat plate with random SHO roughness. Later, Peguero and Breuer (2009) conducted PIV measurements over two SHO surfaces with random patterns (sand-blast surface and random nanograss) and likewise did not observe any drag reduction in the turbulent regime. Aljallis *et al.* (2013) carried out a drag measurement experiment on spray-coated SHO surface with random micro/nanoscale pattern over a wide range of Re number (Aljallis *et al.*, 2013). They showed 30% drag reduction in transitional flow ($10^5<Re<10^6$) but in high Reynolds turbulence ($10^6<Re<10^7$) drag increased. Aljallis *et al.* (2013) speculated that the plastron depletion due to high shear flow resulted in a rough surface and increase of skin friction at high Re number. However, Gad-el-Hak (2013) commented that the increase of skin-friction may not be due to the depletion of the air layer. The length scale of the surface roughness estimated from SEM photographs is lower than 1 μm, which implies the wetted surface is hydrodynamically smooth compared to the estimated thickness of the viscous sublayer (~15 μm). Most recently, Bidkar *et al.* (2014) carried out a direct measurement of skin-friction on SHO surfaces with random texture of various surface characteristics using a floating plate assembly in Re number in the range of 10^6 to 9×10^7. Their results showed up to 30 percent reduction of skin-friction in fully turbulent flow promoting further investigation of the turbulent flow over large-scale SHO surfaces with random texture. The apparent contradiction between the experimental results might be due to the depletion of the air pockets, relative size of surface textures to the flow scales (e.g., thickness of the viscous sublayer), and also measurement uncertainties.

Gad-el-Hak (2013) has also emphasized on the necessity for detailed characterization of the turbulent flow over random SHO surfaces. In an effort to measure the mean flow and the turbulent fluctuations over a hydrophobic surface with random pattern, Haibao *et al.* (2015) performed hot-film anemometery. They reported that the turbulence intensity (bursting events intensity) and friction on hydrophobic surface (largest contact angle of 105.8°) are decreased

compared to smooth wall flow. Their results are encouraging to further characterize the turbulent flow over superhydrophobic surfaces with a contact angle larger than 150° produced by a random surface texture. A detailed experimental investigation of the turbulent structure of the boundary layer can fulfill the shortcomings of numerical investigations in modeling the random surface pattern and shed light on the possible drag reduction mechanisms.

SHO coatings with random surface texture could have a higher longevity if produced with a hierarchical structure ranging from micro to nano-scale pores (Verho *et al.*, 2011). By employing such a coating on a rotating disc apparatus Moaven and Taeibi (2013) achieved up to 15 % drag reduction in the turbulent regime. Their results further suggested that drag reduction rate decreases with Re number. Bidkar *et al.* (2014) also showed that reduction of skin-friction decreases with Re number for SHO surfaces with surface features comparable in size with the viscous sublayer. Therefore, a sustained drag reduction is obtained when the surface roughness is smaller than the viscous sublayer. However, these results are seemingly in contrast with the experiments of Daniello *et al.* (2009). Their measurements of mean velocity profile and pressure drop over a SHO surface with patterned micro-ridges demonstrated that the skin-friction reduction appears once the size of the surface features is comparable with the viscous sublayer thickness. Furthermore, they reported higher drag reduction at higher Re numbers with a thinner sublayer. The DNS of Martell *et al.* (2010) also indicates that skin friction reduction increases with Reynolds number. This contradiction between surfaces with patterned and random structures might be attributed to the hierarchy of surface features on the random surface and their interference with the viscous sublayer. Precise measurement of turbulent statistics over both surface structures would help delineate the physics behind these dissimilar behaviors.

In view of the recent evidence regarding turbulent drag reduction of SHO surfaces with random surface texture, the present study aims to experimentally investigate the structure of the turbulent flow over these surfaces. The experiments are carried out in a large facility to provide a high spatial-resolution measurement system compared to the flow scales. Two PIV configurations with streamwise/wall-normal and streamwise/spanwise arrangements are applied to comprehensively study the turbulent structure in terms of the mean flow, Reynolds stresses, higher-order turbulence statistics, and the length scale of the coherent motions. The

measurements over the non-wetted SHO surface are compared with the wetted SHO counterpart (similar surface texture) and also a smooth surface. The experiments on the wetted SHO surface also demonstrate the behavior of a SHO surface upon complete depletion of the air layer.

4.2. Results

4.2.1. Mean flow

The normalized mean flow velocity profiles across the channel with the smooth, non-wetted and wetted SHO surfaces are presented in figure 4.1. For calculation of the ensemble averages averaging over the ensemble of the images and also in the streamwise direction have been conducted. Each data point represents the velocity vector obtained from each corresponding interrogation window. No considerable velocity difference is observed between the velocity profiles over the three surfaces (differences are smaller than 0.5% except in the near-wall region). The mean velocity profile of the wetted SHO is also very close to the smooth wall indicating that the surface is hydrodynamically smooth. The results are in contrast with the DNS of turbulent flow over SHO surfaces with patterned micro-ridge structures which are simulated using periodic no-slip no-shear boundary conditions (Martell *et al.*, 2009 and 2010). Their results demonstrate about 30% increase in maximum velocity and a slip velocity in the order of 80% of bulk velocity. Nonetheless, the PIV experiments of Woolford *et al.* (2009) over patterned SHO surface composed of micro-ridges (4 μm wide ridges with cavity width of 32 μm) also exhibited no appreciable near-wall difference in velocity profiles which is in agreement with the present measurements. Daniello *et al.* (2009) reported a slip velocity about 40% of the mean velocity over SHO surface with micro-ridge pattern from PIV measurement. The relatively high slip velocity observed by Daniello *et al.* (2009) has been associated with the large streamwise grooves of 60 μm wide providing large shear free surfaces. Unfortunately, the velocity profiles are not compared with a smooth reference surface. There is also no information provided on the spatial resolution and measurement uncertainties of the applied PIV system. The discrepancy may also be due to the directionality of contact angle (or slip velocity) over a surface with streamwise micro-ridges in comparison with a random texture. Over a surface with streamwise micro-ridges, the streamwise slip is dominant over spanwise slip whereas for random texture SHO surface, slip is omnidirectional.

The magnified view of the normalized mean velocity profiles versus the wall normal distance normalized with the wall unit (λ_0=92 μm) is shown in figure 4.2. The slope of the line passing through the center and the data points of the smooth wall between $4<y^+<8$ is used to estimate a reference wall shear stress (τ_0) and λ_0. The profiles of the non-wetted SHO appear to have about 3-5% larger mean velocity within $4< y^+ < 15$ while the profiles of the smooth and the wetted surface overlap. The profiles also exhibit approximately identical wall shear stress which might be due to insufficient spatial resolution and measurement uncertainty of the PIV system within the sublayer ($y^+< 5$). In the immediate vicinity of the wall at $y^+< 4$, the velocity profile over the non-wetted SHO surface is smaller relative to the wetted surface. Scrutiny of the PIV images shows that the sharp reduction of mean velocity at $y^+< 4$ is due to the biased error of PIV cross-correlation algorithm caused by the strong glare points at the non-wetted surface. The non-wetted SHO surface is covered with a thin air layer which renders a shiny irregular surface with high intensity glare points due to the change in refractive index. The reflections are much weaker in the case of smooth and wetted SHO as the laser light can pass through the surface due to transparency.

The current experiment is carried out at a large facility with a relatively wide channel (W = 50 mm) in comparison to Woolford *et al.* (2009) and Daniello *et al.* (2009) who carried out PIV measurements in channels with 4.6 and 7.9 mm width, respectively. Although the spatial resolution of the PIV measurement shown in figures 4.1 and 4.2 is $3.4\lambda_0$, no recordable slip velocity is detectable. The measurement of slip velocity and the possible difference in wall shear stress of the SHO surface would still require higher spatial resolution relative to the boundary layer scales. This can be possibly achieved using a high magnification imaging combined with the application of fluorescent particles to avoid the intense and irregular reflection of the SHO surface.

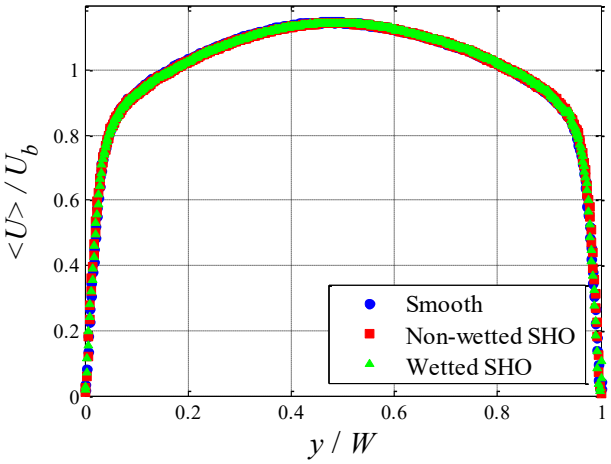

Fig. 4.1. Mean velocity profiles vs wall-normal distance normalized by outer scaling across the channel for the smooth, non-wetted and the wetted SHO surfaces.

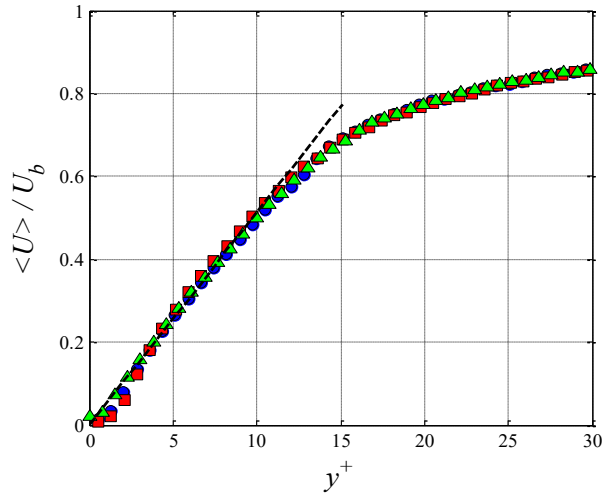

Fig. 4.2. The profile of $U / \langle U \rangle$ versus y^+ in the inner wall layer. The wall normal distance is normalized by inner scaling based on a linear fit (the dashed line) over the near-wall data points of the smooth wall within $4 < y^+ < 8$. Labels are the same as figure 4.1.

The normalized profiles of streamwise Reynolds stress $\langle u^2 \rangle / u_{\tau 0}^2$ over the three surfaces are shown in figure 4.3.a. The intensities of the smooth and the wetted SHO surface overlap which indicates that the micro-scale roughness of the wetted SHO surface ($R_{PT} = 41$ μm is one order of magnitude smaller than the viscous sublayer thickness) acts as hydrodynamically smooth wall with negligible effect on the turbulent flow (Schultz & Flack, 2007). It is also evident that the flow over the non-wetted SHO wall experiences lower streamwise turbulent fluctuations compared to the smooth and the wetted SHO surfaces. The non-wetted SHO surface exhibits

about 12% attenuation in the peak value compared to smooth surface. Furthermore, the location of maximum $\langle u^2 \rangle / u_{\tau 0}^2$ for the non-wetted SHO is shifted about 3 wall units away from the wall demonstrating a thicker viscous sublayer. The increase in $\langle u^2 \rangle / u_{\tau 0}^2$ of the smooth and non-wetted surface for $y^+ < 10$ is due to the biased error of PIV algorithm due to stronger wall scattering of these surfaces. The wall-normal Reynolds normal stress $\langle v^2 \rangle / u_{\tau 0}^2$ profiles presented in figure 4.3.b also show a similar behavior with the profiles of smooth and wetted surfaces almost overlapping. The non-wetted SHO surface exhibits about 13% attenuation in the peak value compared to smooth surface. However, the maximum of $\langle v^2 \rangle / u_{\tau 0}^2$ is displaced away from the wall about 15 wall units. Normalized profiles of Reynolds shear stress $\langle uv \rangle / u_{\tau 0}^2$ over the smooth and wetted SHO walls show negligible difference whilst it is smaller over the non-wetted SHO surface as observed in figure 4.3.c. The peak value reduces by 15 % and shifts about 15 wall units away from the wall for the non-wetted SHO surface. The reduction of Reynolds shear stress for flow over the current non-wetted SHO surface with random pattern demonstrates reduction of total shear stress due to the similar velocity profiles (similar viscous shear stress) and also reduction of turbulence production in the inner layer.

The distinguishable effects of the non-wetted SHO on the profiles of Reynolds stress were the variation in the intensity and the location of the maximum values. The current measurements shows that the peak value of the Reynolds stresses attenuates and shifts away from the wall implying thicker viscous sublayer. The PIV experiment of Woolford *et al.* (2009) also shows attenuation of normal and shear Reynolds stresses with slight displacement of the peak value towards the wall over streamwise micro-ridges (streamwise slip). Their measurement over transverse micro-ridges (spanwise slip) shows an opposite trend of intensification and displacement away from the wall. Similar trends as the experiment of Woolford *et al.* (2009) is also observed in the DNS of Martell *et al.* (2009, 2010) over patterned SHO surfaces. Their results showed that for streamwise micro-ridges the peak turbulence levels move towards the wall while in the case of transverse micro-ridges Reynolds stress profiles are similar to the smooth wall. Conversely, the DNS of Min and Kim (2004) for flow over patterned surfaces with solely streamwise slip and combined streamwise-spanwise slip agrees with the current experimental observations. Their DNS simulation shows attenuation with the displacement of the

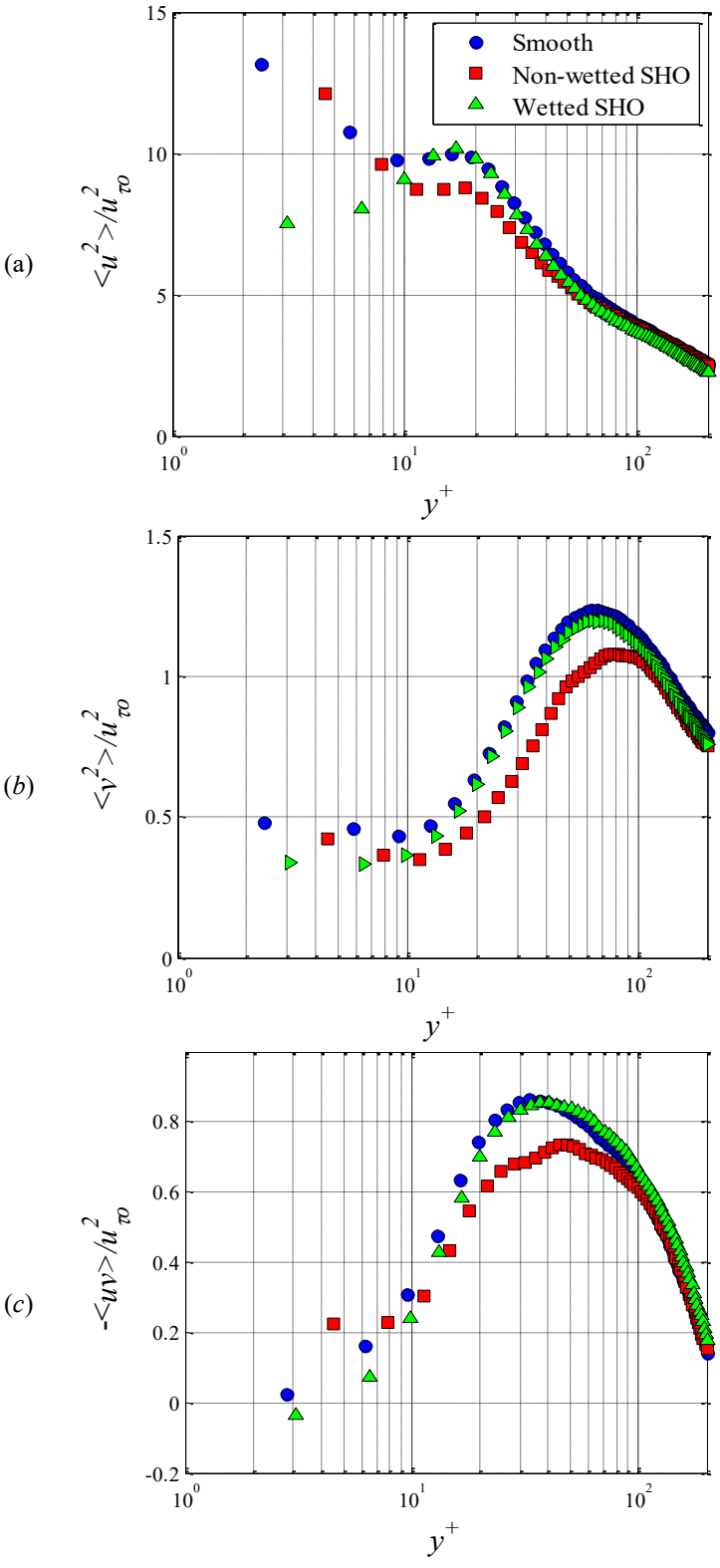

Fig. 4.3. Normalized profiles of normal Reynolds stresses (a) $<u^2>/u_{\tau 0}^2$ and (b) $<v^2>/u_{\tau 0}^2$ and the Reynolds shear stress (c) $-<uv>/u_{\tau 0}^2$ over the three surfaces.

peak location away from the wall for these two cases. However, for the case of only spanwise slip, $<u^2>$ intensifies and the peak location moves closer to the wall.

Figure 4.3 also demonstrates that the turbulence attenuations over the SHO surface are not limited to the sublayer and buffer layer and are well extended into the log layer with the highest variation at about $20 < y^+ < 50$ (buffer layer). Most of the turbulent activities occur in this region and have a growing dominance over the viscous effects. As y increases towards the channel center the profiles of the surfaces tend to merge. Hereafter, due the fact that wetted SHO surface acts as a hydrodynamically smooth surface the results associated with this surface will not be presented for brevity.

4.2.2. Ejection and sweep events

Quadrant analysis is applied to scrutinize the effect of the non-wetted SHO surface on the turbulent motions in the near wall region. Figures 4.4.a-c show the quadrant distribution of u and v fluctuations on the smooth and the non-wetted SHO surfaces at $y^+ =$ 10, 20, and 30, respectively. The events responsible for the large negative Reynolds shear stress are the ejection ($u < 0$, $v > 0$) and sweep ($u > 0$, $v < 0$) motions over both surfaces. In a turbulent wall flow, the ejections have a larger contribution to the Reynolds shear stress across most of the wall normal distance. The contribution of the ejections reduce with moving closer to the wall as the sweep events become more pronounced with larger contribution to turbulence production in the sublayer (Ghaemi & Scarano, 2011). This trend is clearly observed in Fig 6.a-c as the u-v distribution become more skewed towards the ejection events (higher probability on the left side of $u = 0$ axis) with increase of y^+ over the smooth surface.

The sweep events over the non-wetted surface are observed to be weaker in comparison with the sweeps of the smooth surface. This is evident from the smaller area covered by the 0.1% contour of the non-wetted SHO surface at the fourth quadrant (Q_4) of figure 4.4.a. The ejection events have a similar strength for both surfaces as the contours almost overlap in the second quadrant (Q_2) of figure 4.4.a. In figure 4.4.b, there is slight increase of the strength of sweep events over the non-wetted SHO in the Q_4 quadrants. As the wall normal distance increases, the

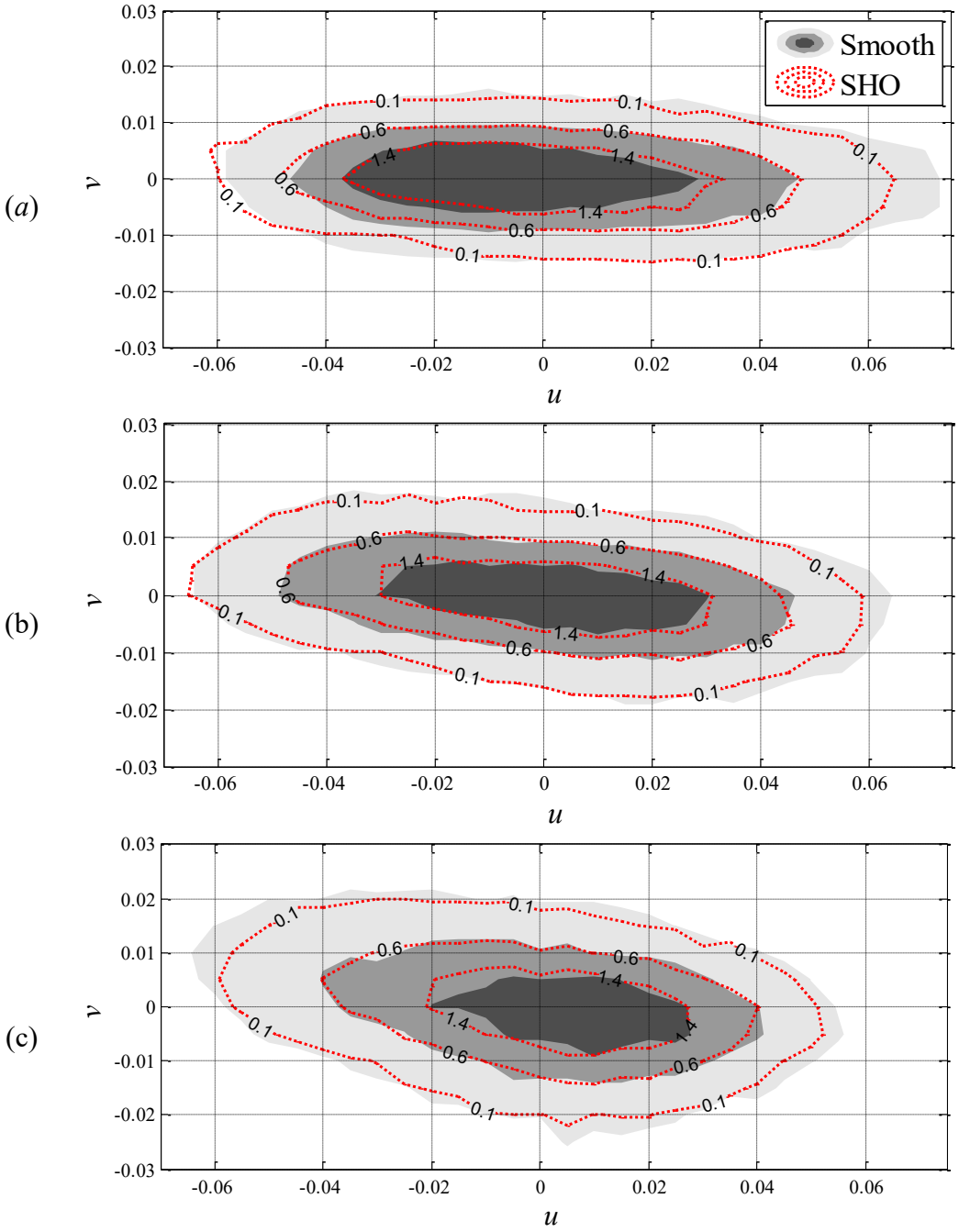

Fig. 4.4. The probability density function (PDF) of turbulent motions over the *u*-*v* quadrant within the boundary layer at wall-normal locations of (a) $y^+ = 10$, (b) $y^+ = 20$, (c) $y^+ = 30$. The filled contours illustrate the PDF velocity fluctuations over the smooth surface while the red dotted contours represent the non-wetted SHO surface. The dark gray, medium gray and light gray colors denote 1.4, 0.6 and 0.1 % PDF values. The PDFs are in percentage and the velocity fluctuations are in m/s.

difference in the contours at Q_4 quadrant (sweep) decreases and discrepancy of the contours is related to the Q_2 quadrant (ejection) as observed in figure 4.4.c. This implies that in the sublayer the non-wetted SHO surface attenuates the sweep events while outside of the sublayer in the buffer layer the effect on the sweep events weakens and the ejection events are attenuated. Therefore, the maximum reduction of Reynolds shear stress which was observed in figure 4.3.c at $y^+ = 30$ is due to the dampening of the ejection events.

Conditional averaging of Reynolds shear stress based on the four quadrants provides detailed information on the contribution of ejection and sweep motions to the total turbulence production. The results are presented in figure 4.5 for the non-wetted SHO and the smooth surface. The profiles associated with Q_2 and Q_4 events (figure 4.5.a) contribute to positive turbulence production (negative Reynolds shear stress) and the profiles associated with Q_1 and Q_3 events (figure 4.5.b) contribute to negative turbulence production (positive Reynolds shear stress) (Kim *et al.*, 1987). For both the smooth and non-wetted SHO surfaces, the conditional average of the Q_4 events is larger than the Q_2 events near the wall at $y^+<15$. Consequently, the Q_4 events (sweeps) dominate at the near-wall region ($y^+<15$) which is in agreement with Kim *et al.*(1987) DNS simulation of turbulent channel flow (Kim *et al.*, 1987). As the distance increase the Q_2 events dominate the turbulence production. This overall trend of sweep and ejection dominance is similar for both the smooth and non-wetted surfaces. However, a suppression of both the ejection and sweep events is observed over the non-wetted surface corroborating the experimental results of Haibao *et al.*(2015) and DNS simulations of Jelly *et al.* (2014). Compared to smooth wall, the peak activity of Q_2 and Q_4 events over the SHO surface is suppressed by 15% and 17%, respectively. Jelly *et al.* (2014) reported 23% and 17% reduction of Q_2 and Q_4 values for flow over SHO surface comprised of streamwise ridges. A difference between the present results and the DNS simulation of Jelly *et al.* (2014) is in the wall normal displacement of the peak values. According to figure 4.5.a, the wall-normal positions of peaks have moved away from the wall which is consistent with the turbulent intensity profiles of figure 4.3. However Jelly *et al.* (2014) reported an opposite displacement of the peak locations. The conditional average of Q_1 and Q_3 events in figure 4.5.b also reduce over the non-wetted SHO wall agreeing with Jelly *et al.*'s results except for the near wall region where they report a bulge in Q_1 magnitude. They associated it to a region of negative turbulent kinetic energy production.

On the whole, both the sweep and ejection events are suppressed over the non-wetted SHO surface leading to smaller Reynolds shear stress and consequently attenuation of turbulence production. As a result, theoretically skin-friction would decrease over a non-wetted SHO surface.

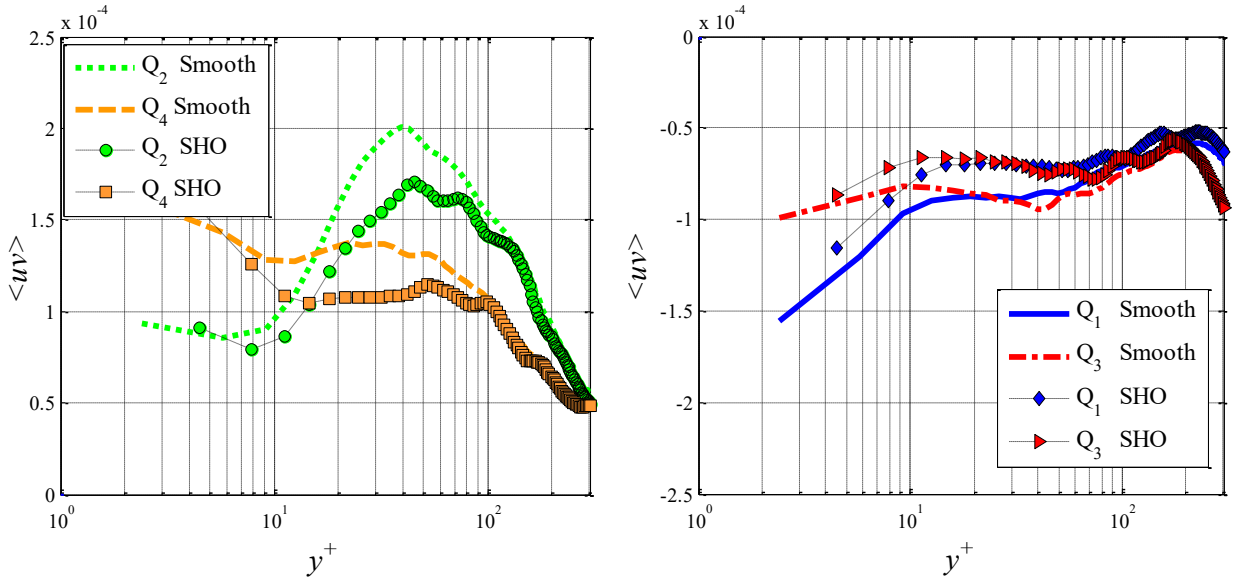

Fig. 4.5. Contribution of (a) second and fourth quadrants, (b) first and third quadrants to Reynolds shear stress $<uv>$ (m^2/s^2).

The triple products of the turbulent fluctuations are investigated to identify the direction of the transport of turbulent kinetic energy. The experiments of Andreopoulos and Bradshaw (1981) on turbulent boundary layer over a rough wall indicated that the triple products of velocity fluctuations can reveal the changes in turbulence structures induced by surface boundary condition. There is no significant change in the general trend of turbulent structures and transport in triple products on figure 4.6 over the smooth and the non-wetted surfaces. The transport direction of $<u^2>$ component of the turbulent kinetic energy (TKE) by means of streamwise velocity fluctuations is indicated by $<u^3>/u_{\tau 0}^3$. The positive value of $<u^3>/u_{\tau 0}^3$ observed in figure 4.6.a confirms the dominance of the sweep events (fourth quadrant) at $y^+ < 12$ while the negative values beyond $y^+ > 12$ show the weakening of the sweeps and the growing dominance of the ejection events (second quadrant) in transport of $<u^2>$ over both surfaces. However, a

noticeable attenuation of $<u^3>/u_{\tau 0}^3$ is observed over the non-wetted SHO surface in the range of $15 < y^+ < 50$.

Figure 4.6.b shows the distribution of $<v^3>/u_{\tau 0}^3$ which represents wall-normal transport of the $<v^2>$ component of TKE by means of wall-normal velocity fluctuations. The direction of $<v^2>$ TKE transport is towards the wall within $8 < y^+ < 33$ and away from the wall for $y^+ > 33$. Similar to $<u^3>/u_{\tau 0}^3$ results, the intensity of these wall-normal motions is significantly decreased over the non-wetted SHO wall.

Figure 4.6.c demonstrates the velocity triple product $<u^2v>/u_{\tau 0}^3$ which indicates the wall-normal transport of $<u^2>$ by means of wall-normal velocity fluctuation (v). The negative sign of $<u^2v>/u_{\tau 0}^3$ at $y^+ < 15$ implies transport of $<u^2>$ towards the wall for both smooth and SHO surfaces. For $y^+ > 15$, the turbulent transport of $<u^2>$ is directed away from the wall as the sign of $<u^2v>/u_{\tau 0}^3$ is positive. The streamwise transport of $<v^2>$ stress presented by $<uv^2>/u_{\tau 0}^3$ is shown in figure 4.6.d. The positive values for smooth and SHO profiles adjacent to the surface ($y^+ < 19$) suggests that streamwise acceleration of the streamwise transport of Reynolds stress has been attenuated. Away from the wall ($y^+ > 19$), streamwise deceleration of transport of Reynolds stress is also reduced implying that regardless of acceleration or deceleration in streamwise transport presence of SHO surface reduces the turbulent fluctuations. The streamwsie and wall-normal turbulent flux of u^2 and v^2 contribution to TKE have been declined for flow over the non-wetted SHO wall compared to reference smooth wall regardless of the transport direction resulting in turbulent production deficit.

Although the quadrant analysis provides helpful information on the contribution of ejection and sweeps to the turbulence production, it does not reveal the properties of vortical structures associated with these motions. Further analysis on the length scales and vortex structures would shed light on the effect of surface slip on turbulent flow structures.

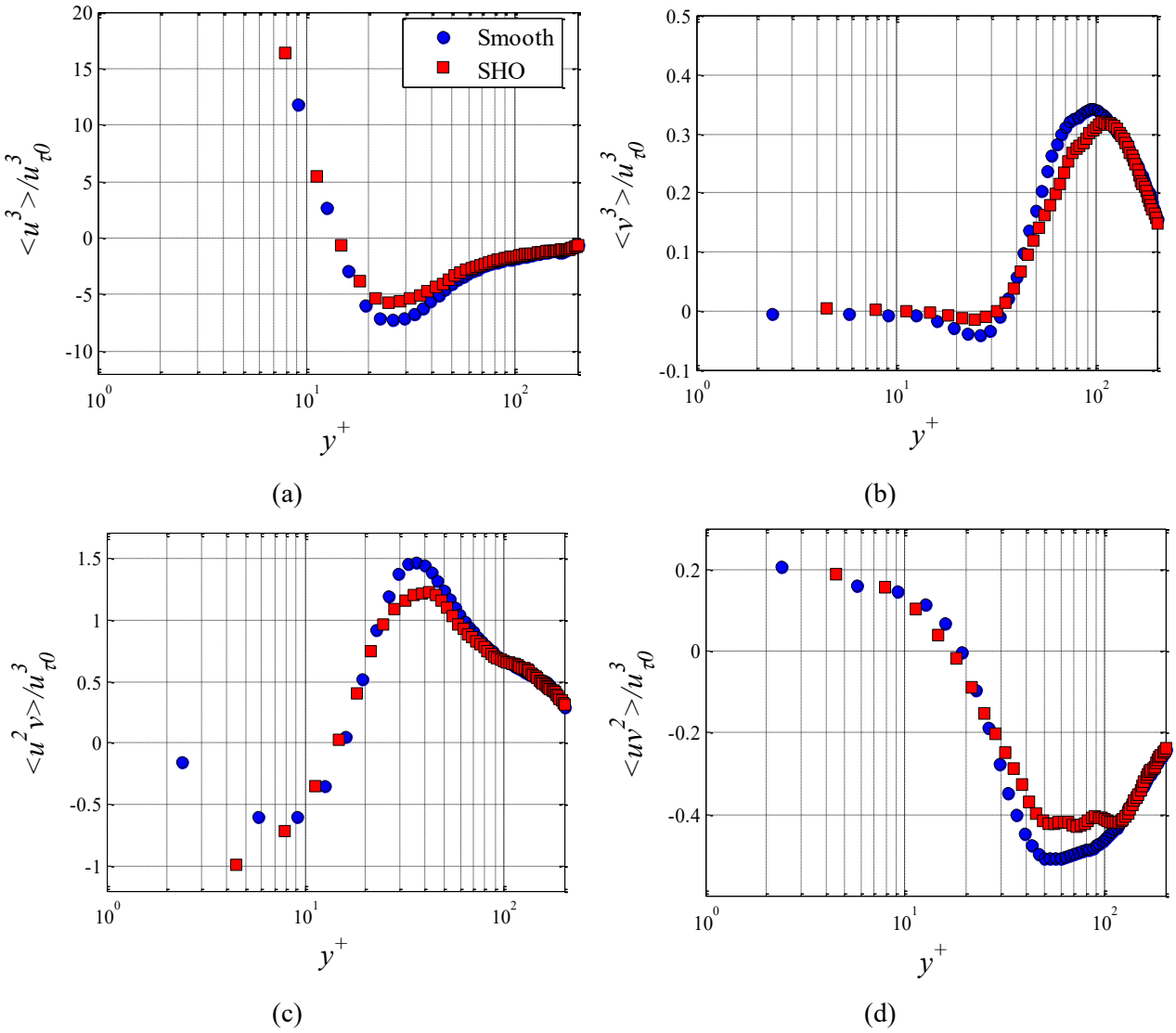

Fig. 4.6. The velocity triple products for the smooth and the non-wetted SHO surfaces in inner scaling (a) $<u^3>/u_{\tau 0}^3$, (b) $<v^3>/u_{\tau 0}^3$, (c) $<u^2v>/u_{\tau 0}^3$, (d) $<uv^2>/u_{\tau 0}^3$.

4.2.3. Length scales

Characterization of the turbulence structures especially in the near-wall can elucidate the mechanism of skin friction reduction. In a turbulent boundary layer, the streamwise and quasi-streamwise vortices strongly interact with the low and high speed streaks through ejection and sweep motions. According to White *et al* .(2004), there is a consensus that regardless of the drag reduction method, the effect of various drag reduction methods includes weakening of the streamwise vortices which results in decrease of the strength and increase of the spanwise

spacing of the streaks (Min & Kim, 2004; Sanders *et al.*, 2006; White & Mungal, 2008). The spanwise spacing of the streaks is characterized using spanwise correlation of streamwise velocity fluctuations,

$$C_{uu} = \frac{\langle u(y_0,z)u(y_0,z+\Delta z)\rangle}{\langle u(y_0,z)^2\rangle} \quad (4.\ 1)$$

where y_0 is the wall-normal distance. The C_{uu} values associated with the spanwise spacing of the near-wall low-speed streaks at y_0^+=15 are presented in figure 4.7.a for the smooth and the non-wetted surfaces. The streak spacing is defined as twice the spanwise Δz for the minimum value of C_{uu} (Smith, 1983; White *et al.*, 2004). The minimum of C_{uu} occurs at Δz^+= 64.0 and Δz^+=71.2 for smooth and non-wetted SHO surfaces, respectively. The separation of around $128\lambda_0$ (Δz^+= 64.0) for the smooth surface is consistent with White *et al.* (2004) at the same y^+. The spanwise spacing over the non-wetted surface increases by 11% ($14\lambda_0$) demonstrating thicker streaky structures and reduction of turbulent production in the near wall region. The interface of the low and high speed streaks is known to be populated with quasi-streamwise vortices (Ghaemi & Scarano, 2011; Kim, 2011). This relatively lower density of streaks theoretically lowers the population density of the vortices leading to skin friction reduction which is also in agreement with the simulation of Jelly *et al.* (2014).

The streamwise correlation of streamwise velocity fluctuations following

$$C'_{uu} = \frac{\langle u(x,y_0)u(x+\Delta x,y_0)\rangle}{\langle u(x,y_0)^2\rangle} \quad (4.\ 2)$$

obtained at Δx^+= 240 is plotted versus the wall normal distance (y_0) to characterize the streamwise length scales of the flow structures. As shown in figure 4.7.b, in the range of $10< y^+ <40$ which mostly covers the buffer layer, the flow structures have been attenuated in size implying the dampening of the ejection events. In this y^+ range, the dominant flow structures are the streamwise vortices. Weakening of the ejection events could in turn lead to weaker streamwise vortices that are responsible for high turbulent fluctuations and consequently high skin-friction. The reduction in the average streamwise length scale of the structures over the non-wetted SHO surface further continues for $y^+ > 50$ also shows that the large scale flow

structures of the logarithmic and the outer later are also attenuated over the non-wetted SHO surface.

(a)

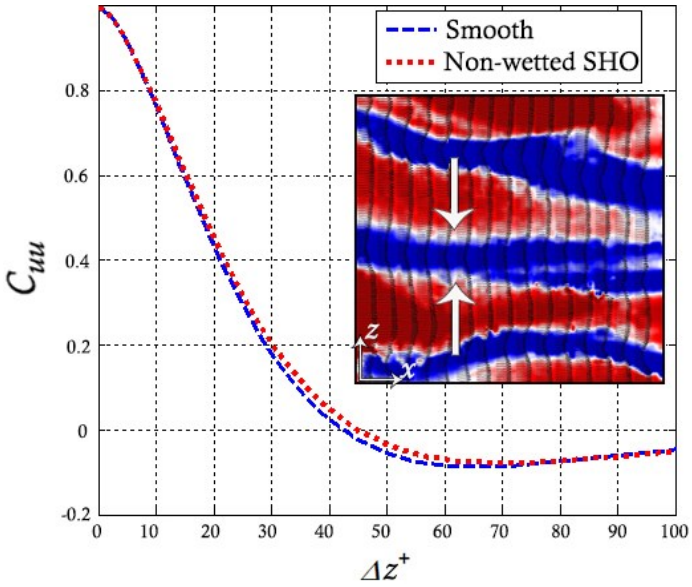

(b)

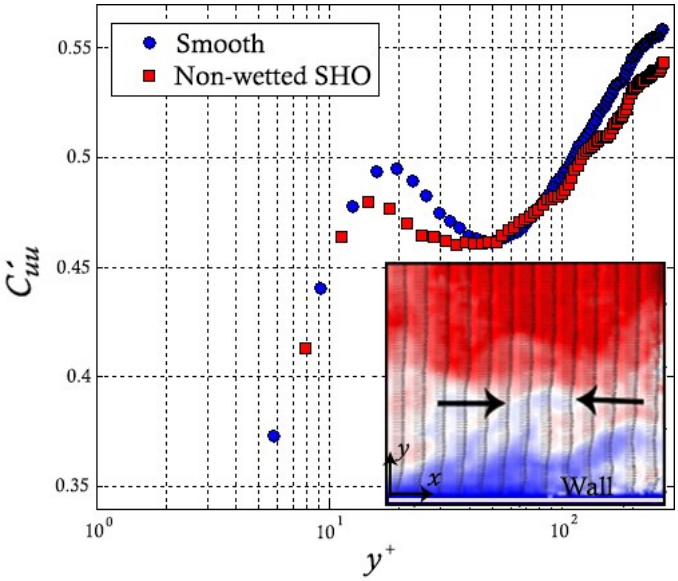

Fig. 4.7. (a) Spanwise correlation function of the streamwise velocity in x-z plane at y^+=15. The image presents the vector field from streamwise/spanwise FOV2 (x-z plane) and the arrows show the spanwise thickness of the low speed streak. (b) Streamwise correlation values of the streamwise velocity at x-y plane corresponding to Δx^+= 240. The image presents the vector field from streamwise/wall-normal FOV1 (x-y plane) and the arrows show the streamwise size of the sample flow structure.

4.2.4. Vortex analysis

The strength of vortical structures provides an indication of turbulence production within near wall region. The Q-criterion proposed by Hunt *et al.* (1988) is applied to identify and evaluate the vortical structures. Figure 4.8.a presents the conditional average of the Q values over regions with $Q > 0.5Q_{max}$ where Q_{max} corresponds to maximum Q over the ensemble of data. The Q values are obtained from planar PIV data (FOV1) associated with the structures in the x-y plane. This conditional averaging only selects vortex cores with large rotation over strain ratio. Relative to the reference smooth surface, vortex strength over the non-wetted SHO surface has been decreased by 12% in the buffer layer. The difference is mostly apparent in the near-wall region (buffer layer) and it diminishes with increase of wall-normal distance. In the outer layer at $y^+ > 50$, due to the lower population of the strong vortices, the conditional average does not reach statistical converge. In the near-wall region, the spanwise-oriented vortices are associated with the early stages of hairpin vortex growth or tilted quasi-streamwise vortices (Sheng *et al.*, 2009). The results confirm reduction in C'_{uu} values in buffer region over the non-wetted surface (figure 4.7.b), both implying weakening of the vortical structures in spanwise direction. These vortical structures induce sweep and ejection events which contribute to the Re stress production (Jelly *et al.*, 2014). Also reflected in quadrant analysis, weakening of the vortical structures leads to suppression of the sweep and ejection events which in turn decreases Re shear stress contribution to the skin friction. Figure 4.8.b further supports the idea of weakening of the vortices over SHO surface. This figure illustrates that the area covered by the spanwise vortical structures detected using $Q > 0.5Q_{max}$ threshold and normalized by the total area of FOV1. The results show reduction of the fractional area over the non-wetted SHO surface in the buffer layer. Figures 4.8.a and b indicate weakening of the vortical structures in strength and size and therefore reduction of turbulence production. These results are in agreement with DNS of Jelly *et al.* (2014).

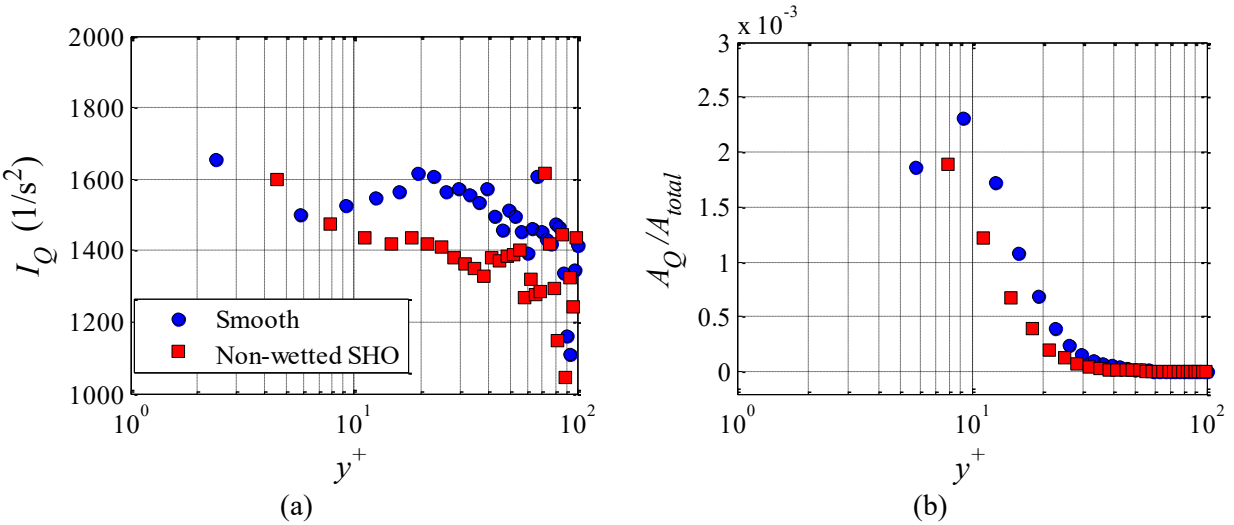

Fig. 4.8. (a) Conditional average of regions with $Q > 0.5Q_{max}$ associated with the spanwise vortex strength versus wall-normal direction. (b) Normalized area of vortical structures detected according to $Q > 0.5Q_{max}$.

4.3. Discussion

A significant reduction of the Reynolds normal and shear stresses (10-15 %) was observed over the non-wetted SHO surface in the wall-normal range of $10 < y^+ < 100$. The mean velocity profile also shows a small increase of about 3-5 % over $5 < y^+ < 15$. A negligible variation of mean velocity profile accompanied by about 10% variation of Reynolds stress is also observed in the PIV measurement of Woolford *et al.* (2007) over a sample with L/W of 27. However, the DNS of Martell *et al.* (2010) reports about 25% increase in maximum velocity values and more than 50% reduction in wall shear stress. In general, the mean velocity profile is not expected to vary in the same order of magnitude as the Reynolds stresses. For example, about 10% change of mean velocity profile (normalized by average channel velocity) corresponds to about 20% change in Reynolds shear stress due to change of channel Re number from 5,600 to 13,750 in the DNS of Kim *et al.*(1987). However, the variation of the mean velocity profiles in the experiments appears relatively small and over a limited range of y^+ in comparison with the results of DNS. The smaller variation in the mean velocity profile over the SHO surface in this work might be associated with the short length of the SHO sample ($8W$) which does not provide sufficient length for the mean velocity profile to adapt to the new surface boundary condition and reach an equilibrium state.

The orientation of the slip velocity over a SHO surface also affects the attenuation or intensification of the turbulent fluctuations. The flow over ordered SHO surfaces with streamwise grooves experiences dominance of streamwise slip while the spanwise grooves work vice versa (Maynes *et al.*, 2007). Nevertheless, over a SHO surface with random texture, the slip would be omnidirectional and the flow would experience slip in both streamwise and spanwise directions. According to the DNS results of Min and Kim (2004), turbulent flow over a surface with omnidirectional slip boundary condition experiences lower rates of drag reduction compared to a surface with merely streamwise slip velocity. This has been attributed to the intensification of streamwise vortices due to the spanwise slip component. Therefore, on a random texture SHO, the attenuation of the streamwise vortices due to streamwise slip is opposed by the adverse effect of spanwise slip. This adverse effect has resulted in 6% increase in the value of $<w^2>$ over the non-wetted SHO wall at $y^+=15$ based on FOV2 measurement. This implies that despite the favorable effect of decreasing $<u^2>$ and $<v^2>$, spanwise slip of the randomly-textured SHO increases the spanwise turbulent fluctuations which may also oppose the near-wall variation of mean velocity.

The streamwise slip velocity resulted in larger streak spacing as it was observed in figure 4.7.a. The streaks are also more coherent and consequently their population density reduces similar to the observations of other drag reduction methods (Min & Kim, 2004; Sanders *et al.*, 2006; White & Mungal, 2008). The steamwise low and high speed streaks are generated by the streamwise vortices of the inner layer (Kim, 2011), therefore, the streamwise vortices are also attenuated in number density and strength. The results show an increase in spacing and consequently reduction in number of streaks, and accordingly the number of streamwise vortices is also predicted to decrease. This trend is also reported in the DNS of Jelly *et al.* (2014) in which a remarkable decrease in the population density of the vortices is observed. A reduction in the strength and size of the spanwise vortices is also observed in figure 4.8. The suppression of the vortices attenuated the ejection and sweep motions as it was evident in figures 4.4-6. Smaller streamwise flow structures in figure 4.7.b further supports the idea that SHO surface suppresses the turbulence generation by weakening the ejection/sweep motions and reducing their interaction with the mean shear. Therefore, the turbulence production and subsequently skin-friction

reduces. However, as discussed above the spanwise slip may adversely affect the drag reduction process by amplifying spanwise fluctuation and increasing the spanwise turbulent intensities.

The reduction of Reynolds stresses suggests that SHO surfaces with random patterns can lead to skin-friction drag reduction in a channel flow. This conclusion is consistent with the experiments of Bidkar *et al.* (2014) demonstrating that to achieve for skin friction reduction, the roughness size of the SHO texture should be one order of magnitude smaller than the thickness of the viscous sublayer. This criterion also applies to the current experiment as observed in figure 3.2.a. The current results also supports Gad-el-Hak's (2013) comment regarding measurement uncertainties of the possibly wetted SHO surface in the work of Aljallis *et al.* (2013). According to the discussion of Bidkar *et al.* (2014), the roughness size becomes comparable with sublayer thickness in higher Reynolds numbers and the drag reduction decreases. Furthermore, current experiments showed that the wetted SHO surface is hydrodynamically smooth and does not increase skin friction. Therefore, the drag increase in Aljallis *et al.* (2013), which was initially speculated to be due to the adverse effect of wetting, might be associated with the measurement uncertainties or the uncontrolled experimental conditions including changes in the location of laminar-turbulent transition due to vibration and superhydrophobicity as explained by Gad-el-Hak (2013).

4.4. Conclusion

Turbulent flow over smooth, non-wetted SHO and wetted SHO surfaces is experimentally investigated. Flow characteristics are measured using planar PIV applied in two different configurations of streamwise/wall-normal and streamwise/spanwise planes. The features of the SHO surface are at least an order of magnitude smaller than the sublayer thickness. A small increase in mean velocity (3-5%) is observed within $4< y^+ < 15$ over the non-wetted SHO surface. The normal and shear Reynolds stresses attenuate in the buffer and logarithmic layers by 15% with the peak wall-normal position moving away from the wall by 15 wall units. The flow over the wetted SHO surface does not experience any change in the mean velocity nor in the Reynolds stresses. This agrees with that fact that the roughness size is smaller than the thickness of viscous sublayer rendering a hydrodynamically smooth wall. Quadrant analysis of the sweep and ejection events suggests that the sweep/ejection events are suppressed due to the slip on the

non-wetted SHO surface. The non-wetted SHO surface tends to have a stronger effect on the ejection events with increase of wall-normal distance. The intensity of the ejection and sweep events over the SHO surface is suppressed by 15% and 17% in comparison with the smooth wall, respectively. It was also seen that the transport of the turbulent kinetic energy is attenuated. The streamwise low and high speed streaks over the non-wetted SHO surface evolve to more coherent structures with 11% increase in spanwise spacing. Analysis of vortical structures showed that the string spanwise vortical structures attenuate by 13% in the buffer layer over the non-wetted SHO. The reduction of Reynolds stresses along with attenuation of the ejection and sweep motions, low and high speed streams and the vortical structures indicate lower turbulence production over the non-wetted SHO surface.

5. Near-wall flow measurement using long-range micro-PTV: Assessment of measurement accuracy

The effectiveness of the changes, described in section 3.2.1, aiming to improve the measurement system as well as ascertaining a fully-developed turbulent boundary layer is evaluated here. Planar PIV experiment has been conducted to check the fully-development of the flow as well as its symmetry. Long-range micro-PTV data are presented which provide high-resolution data from near-wall behavior of the turbulent boundary layer. In this chapter, only the results of the flow over smooth wall are presented as a reference to observe the improvements and ascertaining the flow quality.

5.1. Planar PIV

The mean velocity profile and its inverse with respect to the channel centerline are plotted in figure 5.1. The plot is scaled with outer parameters for easier observation of possible asymmetry in the profile. The coincidence of the mean flow profiles over top and bottom walls indicates the symmetry of the channel flow which is a result of the improvements described in section 3.2.1.

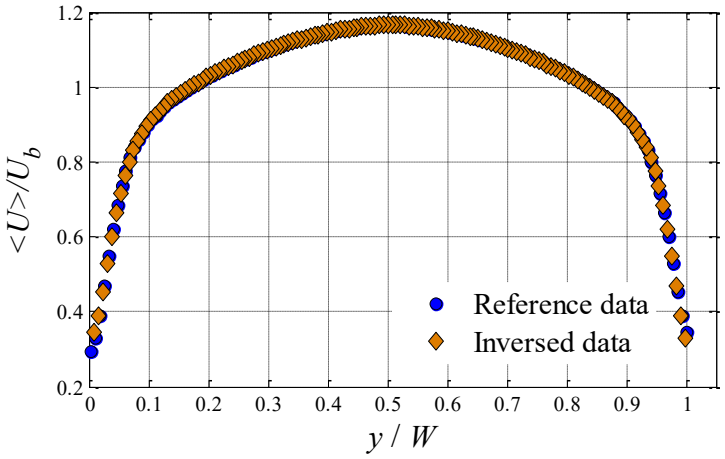

Fig. 5.1. Mean velocity profile and its inverse along the channel centerline (streamwise direction).

In figure 5.2.a-c, the Reynolds stress profiles, obtained from 2C-PIV, are also plotted in the same manner as in figure 5.1. The higher order statistics would amplify any asymmetry. However, the profiles of the intensities also demonstrate reasonable symmetry in channel width. The subtle discrepancy between the $<v^2>/u_\tau^2$ profiles ($0.2 < y/W < 0.3$) is due to the PIV error. Since the rest of the curve is smooth, this error is not associated with convergence issues. One possible explanation is that this local error might be attributed to the different intensity of the particle in that particular region which can be attributed to either non-uniform laser sheet profile or any hindrance to proper imaging of that region. However, visually no noticeable difference could be detected in the images. As shown in figure 5.2.a, the extremum points associated with $<u^2>/u_\tau^2$ is not detected due to the eliminated erroneous data points adjacent to the wall. Nevertheless, the peak points of $<v^2>/u_\tau^2$ profile are resolved in figure 5.2.b. The position of the peaks point for upper wall is at $y/W = 0.14$ at $Re_\tau = \rho u_\tau W/\mu = 146$ which is close the value presented by Moser *et al.*(1999) $y/W = 0.146$ at $Re_\tau = 178$ (for flows with this close Re_τ values very low discrepancy is expected between the normalized profiles (Moser *et al.*, 1999)). Similarly, the $<uv>/u_\tau^2$ profile peak at $y/W = 0.085$ which is pretty close to the same DNS result $y/W = 0.084$. The approximately perfect linear trend of the $<uv>/u_\tau^2$ attests to the fully-development of the flow which will also be examined in the subsequent section.

5.2. Long-range micro-PTV

Examination of the fully-developed behavior of the flow would reveal the effectiveness of the measures taken to improve the experiment detailed in (section 3.2) and guarantee the compliance and consistency with standards introduced by reference data from prior DNS studies. The long-range micro-PTV experiment (details in 3.2.4) is conducted to check these factors and validate the flow and measurement technique with reference data. The velocity profiles presented in figure 5.3 show the fully-developed behavior of the channel flow as it complies with the logarithmic law (the log-law is plotted based on $\kappa = 0.41$ and $\beta = 5.5$). The wall law is also met in sublayer despite the slight discrepancy in the wall vicinity attributed to the PTV measurement error.

The turbulent intensity profiles, in inner scaling (normalized with wall unit of 68 μm), are presented to draw a comparison with reference DNS results of Moser *et al.* (1999). The Reynolds stresses, $<u^2>/u_\tau^2$, $<v^2>/u_\tau^2$, $<uv>/u_\tau^2$, peak at 7.6, 1.54 and −0.75 respectively, which are reasonably in good agreement with the reference data, except for $<v^2>/u_\tau^2$ that has been overestimated. The position of the peak points are also close to reference data although, as it is shown the experimental data are slightly further from the wall due to the lower Re_τ. There is an exception for $<v^2>/u_\tau^2$ profile which shows high biased error. Generally, the reason that the intensity profiles show higher levels of error is related to the higher order of these parameters compared to velocity profile. The high level of error for $<v^2>/u_\tau^2$ is attributed to the low quantity of this parameter compared to the measurement uncertainty level. Nonetheless, the $<uv>/u_\tau^2$ profile shows little discrepancy with reference data because of the fact that the errors associated with u and v do not correlate as in $<u^2>/u_\tau^2$ or $<v^2>/u_\tau^2$.

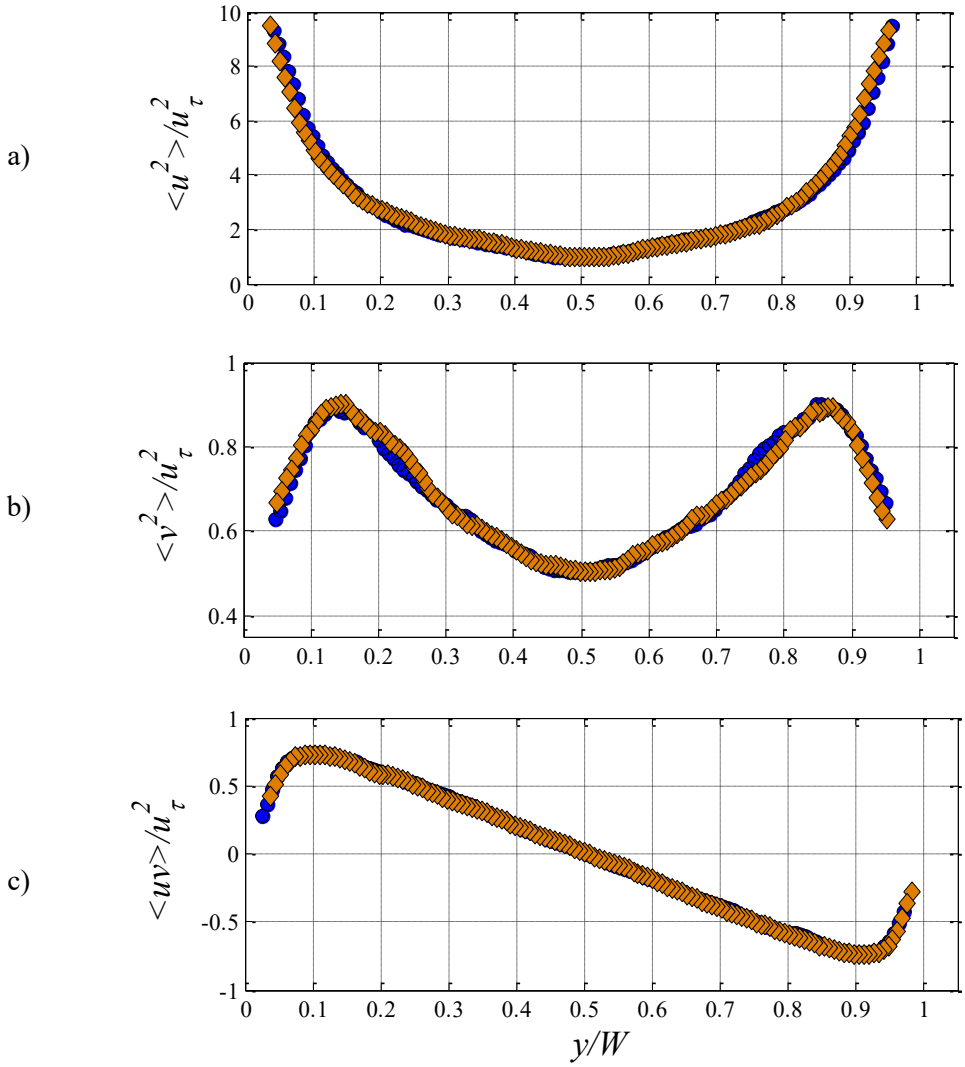

Fig. 5.2. Mean turbulent intensity profile and their inverse along the channel centerline (streamwise direction). a) $<u^2>/u_\tau^2$, b) $<v^2>/u_\tau^2$, c) $<uv>/u_\tau^2$. The markers are the same as figure 5.1.

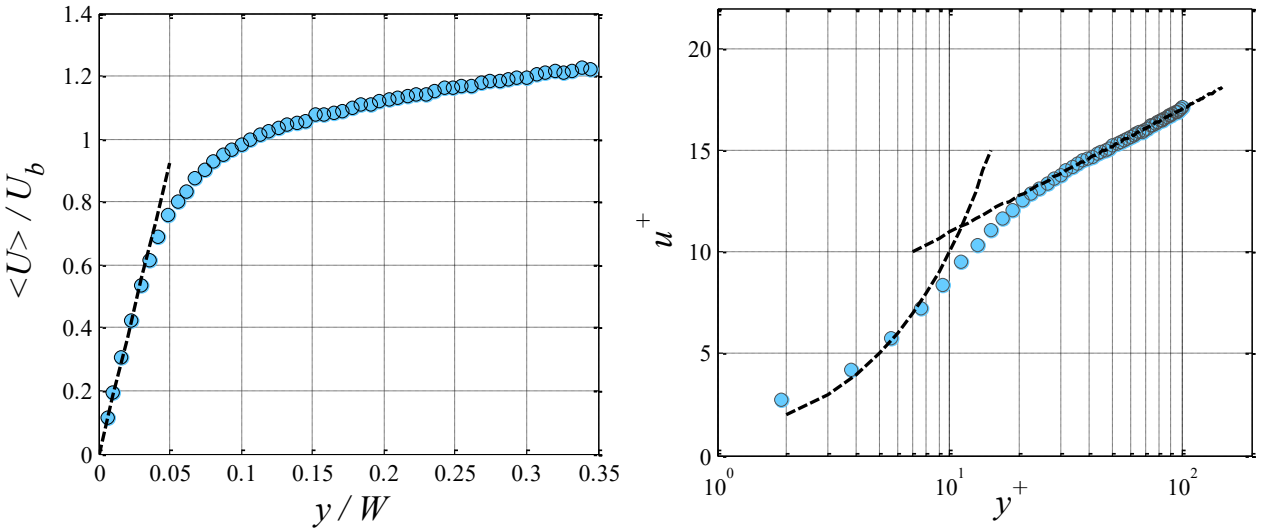

(a) (b)

Fig. 5.3. Mean velocity profiles normalized by a) outer and b) inner scaling. Data is obtained through high-magnification 2C-PTV.

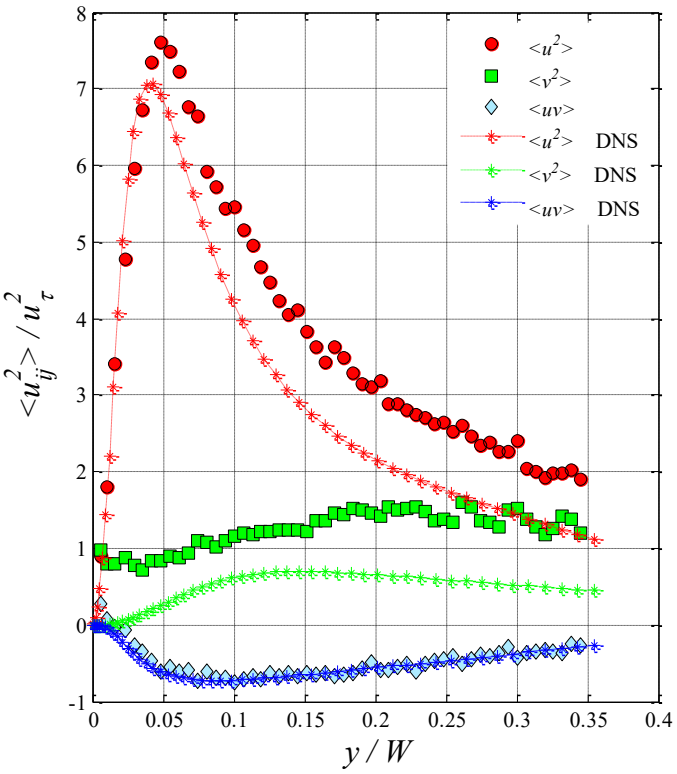

Fig. 5.4. Turbulent intensity profiles normalized by friction velocity at $Re_\tau = 146$. DNS result of Moser *et al.* (1999) at $Re_\tau = 178$ is also shown for comparison.

6. Evaluation of 3D measurement system: Tomographic PIV and 3D-PTV

According to the self-generation cycle of turbulence production (Kim, 2011), the quasi-streamwise vortices are the main factors responsible for induction of skin-friction. These vortices, mostly present in the buffer layer, form high and low-speed streaky flow structures through interaction with mean shear by introducing wall-normal vorticity at streaks edges (identifiable from spanwise inflection points in the streamwise velocity profile). Recognition of the spanwise modulations in the near-wall region, as the salient reasons giving rise to skin-friction drag warrants the application of volumetric measurement technique. 3D measurement can unravel the mechanism of turbulence production by providing full flow statistics. Beside streamwise and wall-normal directions, measurement of the alterations in spanwise turbulent modulations due to changes in the wall boundary condition will decipher the interaction between different flow structures leading to possible skin-friction reduction. Volumetric measurements can present a thorough picture of TBL flow giving us the capability of conducting exhaustive vortex analysis.

The necessity of the 3D measurements is more pronounced in the case of flow control by modification of the wall roughness and surface energy. Different surface modification techniques may lead to different flow manipulation effects. In the case of SHO surfaces, a noticeable

difference can be seen in terms of slip direction. Depending on the geometry of the surface structure elements, isotropic (omnidirectional) or anisotropic slip is achieved. Achievable through current fabrication techniques, all surfaces with random roughness result in isotropic slip length. In contrast, targeted design of surface patterns lead to larger slip length in desired direction and minimizes it in the other direction (anisotropic slip e.g. streamwise microridges). Previous numerical (Min & Kim, 2004; Rastegari & Akhavan, 2015) and experimental (Woolford *et al.*, 2009) studies have shown that the dominant slip direction plays a crucial role in the skin-friction reducing effect of the surfaces. While the largest drag reduction is reported to be attributed to streamwise slip, the surfaces with omnidirectional slip have also been effective (Min & Kim, 2004). DNS studies (Jelly *et al.*, 2014; Türk *et al.*, 2014) have observed formation of secondary flows in the form of coherent streamwsie vortices. Min and Kim's DNS (2004) showed that addition of slip condition in the spanwise direction (similar to random SHO surface) amplifies the quasi-streamwise vortices leading to an adverse effect on the turbulence attenuation.

A thorough 3D experimental study can evaluate the results of the numerical simulations and also enables us to investigate the effect of random surfaces which is not possible by simulation. In particular, study of the spanwise fluctuations would enable us to distinctly judge the efficacy of economical random SHO surfaces compared to fancy patterned ones.

In this chapter, the performance of the 3D measurement system has been evaluated for flow over a reference smooth surface. The 3D measurement of flow over SHO surface were also conducted. However, due to the failure of the newly fabricated SHO surface to affect the flow, the results containing SHO data are presented in Appendix C. This failure is possibly related to the differences between the different batches of the commercial product. Data were collected separately for tomographic PIV and 3D-PTV to get a comparison on the robustness of each method. Based on the 2C-PTV data in chapter 5, the wall unit of the TBL is 68 μm and Re_τ = 146. DNS result of Moser *et al.* (1999) in Re_τ = 178 is used as a reference data to validate the accuracy of the measurement. Due to the normalization of the plots and since the selected Re_τ is rather close, the discrepancy associated with Re_τ difference is not remarkable. Hence, the DNS data can be used as a reference.

6.1. Tomographic PIV

Figure 6.1 presents the mean velocity profile obtained from tomographic PIV process. Although the profile in the middle of the channel seems reasonable, tomo-PIV has failed to accurately measure the near-wall velocity and the PIV biased error is considerable due to presence of the wall. This is noticeable in the $y/W < 0.05$ region where the velocity magnitude is very higher than zero which is expected at $y/W=0$. Bulk velocity is used for normalization of the velocity profile. This velocity is found by averaging the velocity in the wall-normal direction.

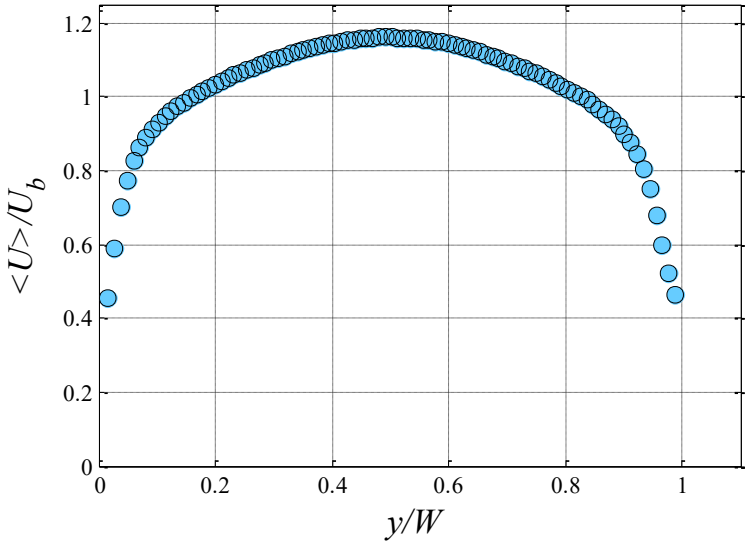

Fig.6.1. Mean velocity profile obtained from tomo-PIV.

The Reynolds stress profiles obtained from tomo-PIV are presented in figure 6.2.a-d. The $<u^2>/u_\tau^2$ and $<uv>/u_\tau^2$ profiles are in good agreement with DNS data except for the near-wall region in which tomo-PIV fails to get the extremum point for $<u^2>/u_\tau^2$ and depicts erroneous quantities for $<uv>/u_\tau^2$. This is due to the fact that for the case of $<u^2>/u_\tau^2$ the relative magnitude of the parameter is very higher than the uncertainty level in the measurement so, the ratio of error to the signal magnitude decreases. The $<uv>/u_\tau^2$ profile also shows rather reliable results which is due to the lack of correlation between the errors associated with each u and v signals. Nonetheless, the noise level increases dramatically for $<v^2>/u_\tau^2$ and $<w^2>/u_\tau^2$ profiles and current tomo-PIV system fails to acquire reliable data for these quantities. Similar to 2C-PIV, one source

of error for $\langle v^2 \rangle / u_\tau^2$ is the high ratio of the measurement uncertainty to signal magnitude which drastically increases the error. Another source of error which mostly affects the $\langle w^2 \rangle / u_\tau^2$ profile is the formation of ghost particles due to the errors during the 3D particle reconstruction technique (Scarano, 2013).

These ghost particles which are produced during the 3D reconstruction impose noticeable noise to the measurement. The rather unsmooth curves especially for $\langle v^2 \rangle / u_\tau^2$ and $\langle w^2 \rangle / u_\tau^2$ profiles is partly associated with the lack of enough convergence. This is investigated through the convergence diagrams presented in figure 6.3.a and b. In which, the variation of the ensemble-averaged quantities normalized with the ultimate value (N=400) versus sample size (N) at a location rather close to the upper wall y/W= 0.1 are plotted. It is noteworthy that the values are averaged over streamwise direction prior to being plotted so that only the effect of sample size would be accounted. The scatter around the ultimate average declines with sample size. Figure 6.3.a presents the convergence diagram for the velocity magnitude $\langle U \rangle$. It is evident that after 20 samples the drastic fluctuations are damped and after 200 samples the magnitude approximately levels off close to 1 and the last 50 data points vary within the range of ± 0.13 percent. However, the convergence for the turbulent intensity profiles occurs with a delay and after averaging over 350 samples the last 50 data points fluctuate between ± 0.40-0.66 percent of the ultimate average value. This implies that higher number of samples is required to reach a convergence level close to the average velocity.

a)

b)

c)

d)

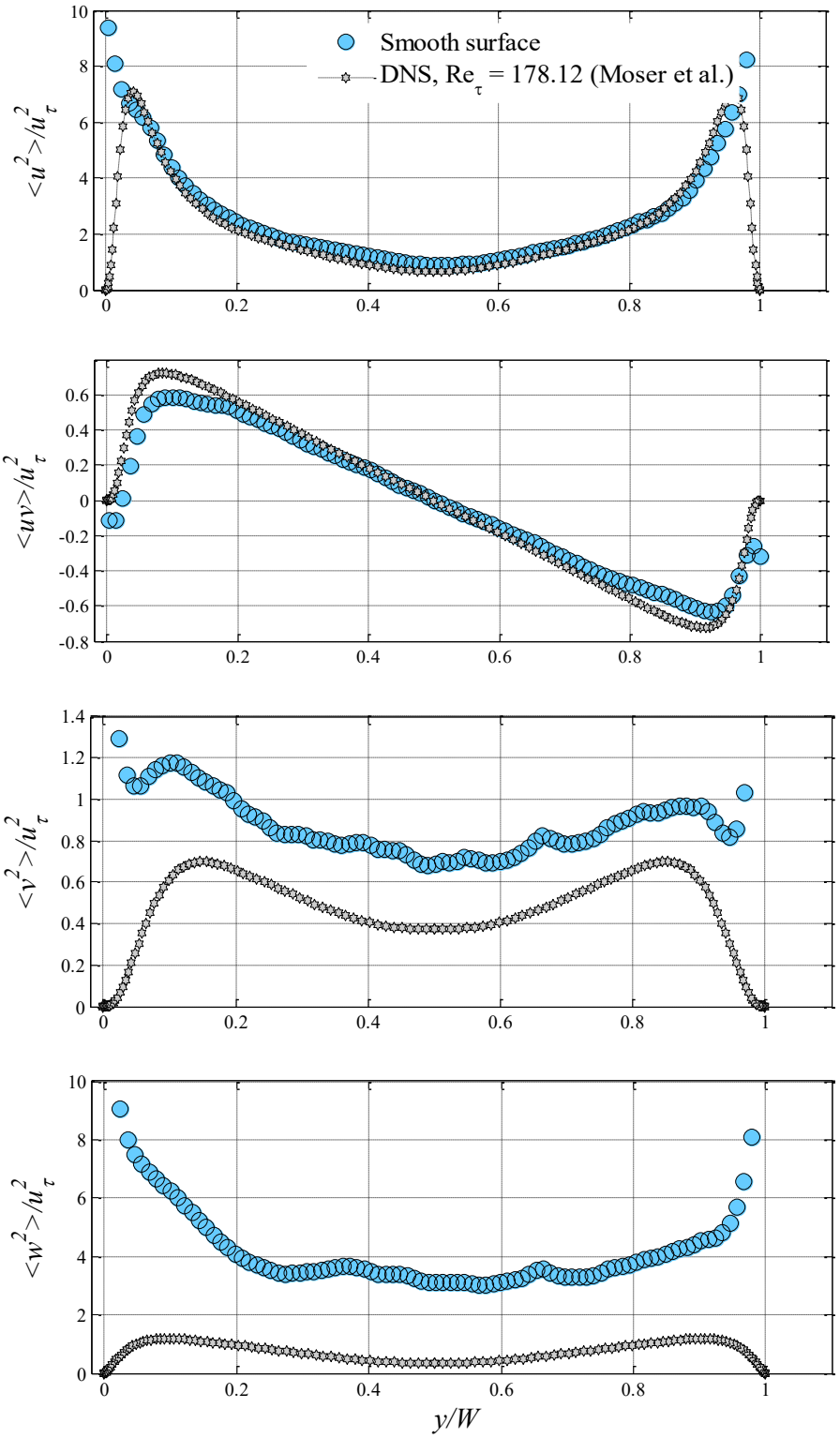

Fig. 6.2. Mean Turbulent intensity profiles acquired from tomo-PIV. a) $<u^2>/u_\tau^2$, b) $<uv>/u_\tau^2$, c) $<v^2>/u_\tau^2$, d) $<w^2>/u_\tau^2$at Re_τ = 146. DNS result of Moser *et al.* (1999) at Re_τ = 178 is also shown for comparison.

(a)

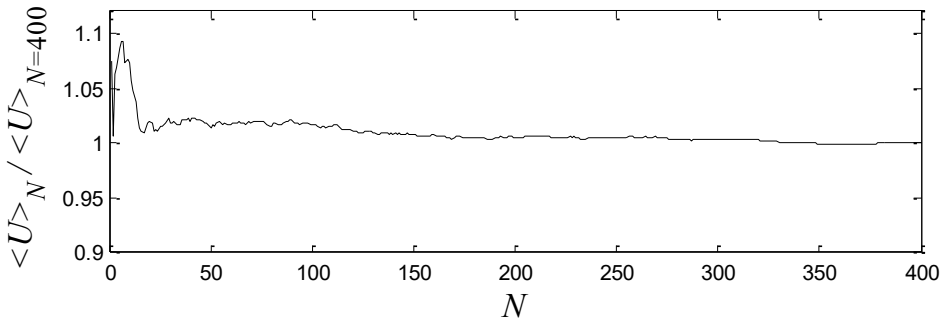

(b)

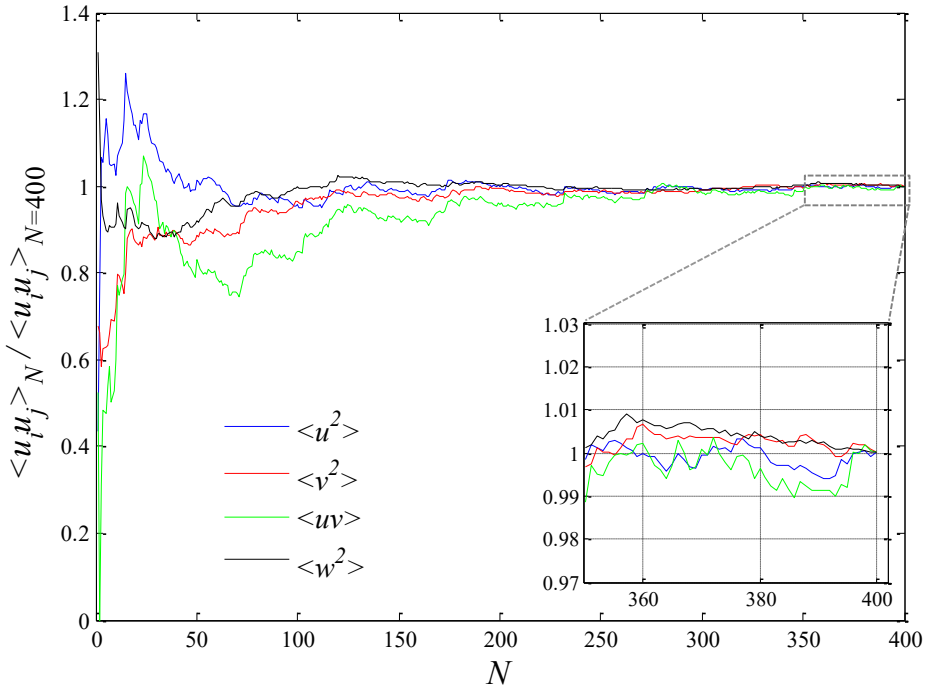

Fig. 6.3. Variations of ensemble averaged values for a) mean velocity, b) turbulent intensities with sample size at y/W= 0.1.

6.2. 3D-PTV

Similar to figure 6.1, figure 6.4 presents the mean velocity profile which is acquired through 3D-PTV process. In comparison with tomo-PIV data, the spatial resolution has improved by 66 percent. Even though the quality of the data has significantly improved in the near-wall region, yet, the velocity at the wall is not zero. Comparatively, the 3D-PTV process gives a better result especially in the near-wall area because of detection and tracking of single particles.

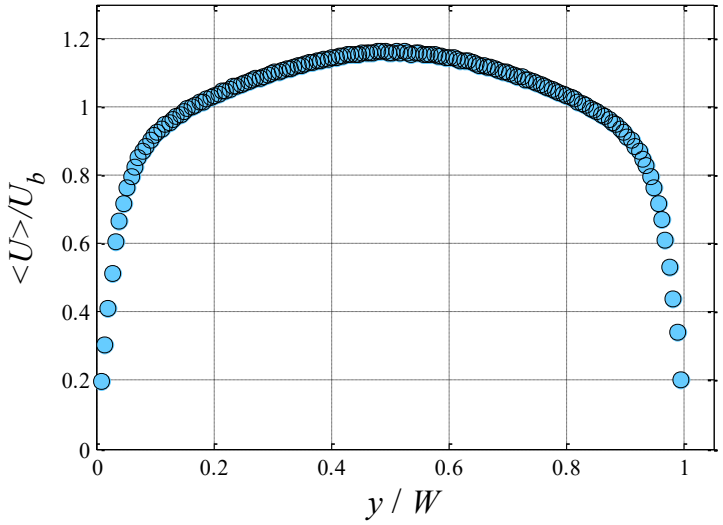

Fig. 6.4. Mean velocity profile obtained from 3D-PTV.

The Reynolds stress profiles obtained from 3D-PTV are illustrated in figure 6.5.a-d. All four profiles are in good agreement with DNS data (Moser *et al.*, 1999). A considerable improvement is associated with detection of the peak points adjacent to the wall especially for $<u^2>/u_\tau^2$, where tomo-PIV delivers erroneous vectors. The position of these peak points are also in agreement with DNS data. For $y/W < 0.2$, it can be shown that the discrepancy between experiment and theory increases. Although it is partially due to the lower Re_τ of the flow, the triangulation error associated with 3D-PTV algorithm of DaVis is also effective. Capturing the near-wall region where most of the turbulence production occurs, in addition to its capability of providing reliable data for $<v^2>/u_\tau^2$ and $<w^2>/u_\tau^2$ profiles, which are not measured accurately by tomo-PIV, are two apparent advantages of the 3D-PTV process over tomo-PIV. Averaging of the velocity vector in particular averaging bins allows us to have data similar to PIV vector field which can be used to calculate vorticity and detect vortices.

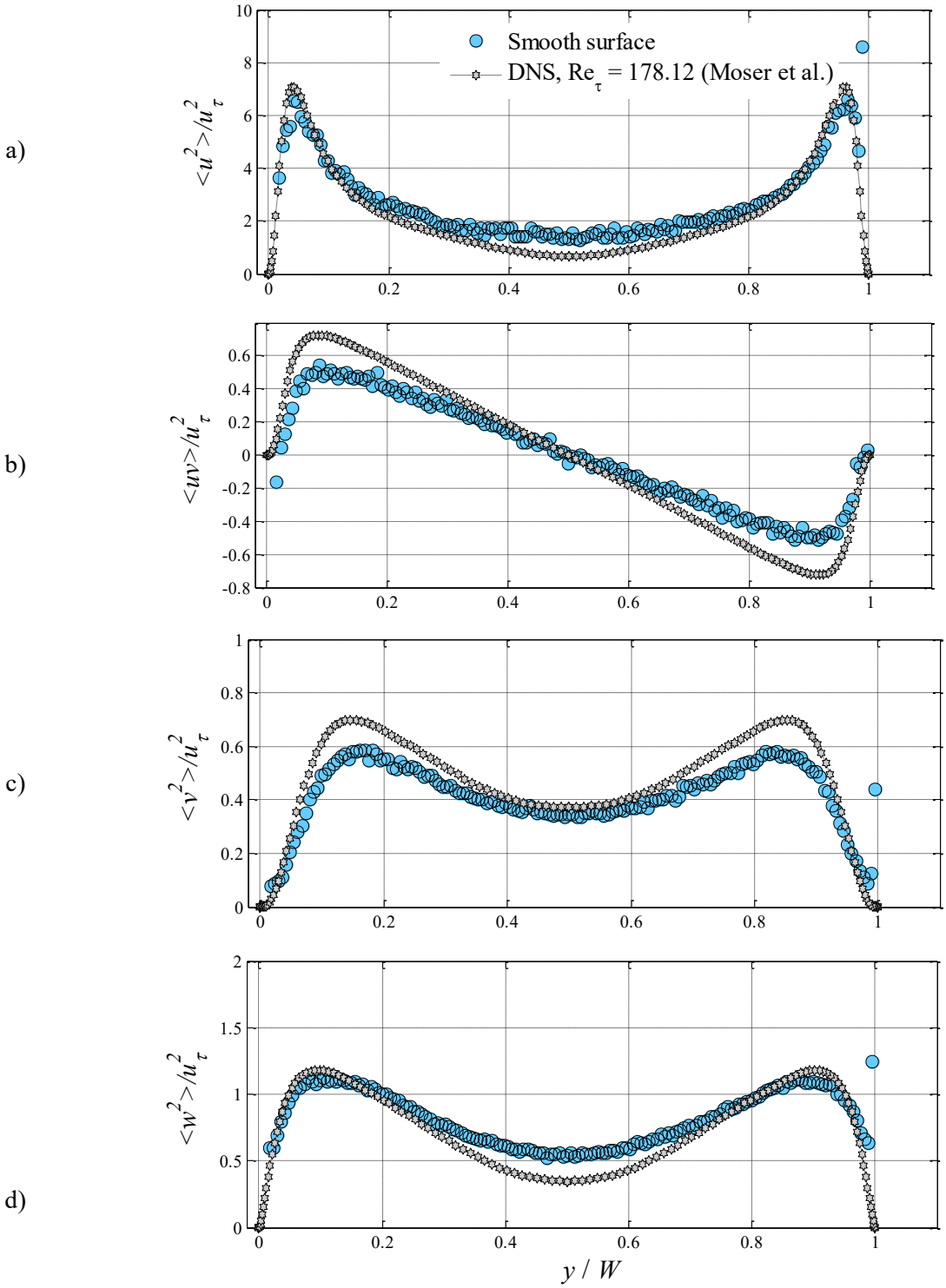

Fig. 6.5. Mean Turbulent intensity profiles acquired from 3D-PTV. a) $<u^2>/u_\tau^2$, b) $<uv>/u_\tau^2$, c) $<v^2>/u_\tau^2$, d) $<w^2>/u_\tau^2$ at $Re_\tau = 146$. DNS result of Moser *et al.* (1999) at $Re_\tau = 178$ is also shown for comparison.

6.3. Conclusion

3D measurement techniques are evaluated for flow over a smooth wall. Performance of the tomo-PIV and 3D-PTV techniques are assessed by their capability in accurately measuring the mean velocity profile and the Reynolds stresses as the higher order statistics. It is shown that the tomo-PIV is successful in measuring the streamwise and shear Reynold stresses while it fails to do so for wall-normal and spanwise Reynold stresses due higher error level. In comparison, the 3D-PTV technique provides higher spatial resolution leading to detection of the near-wall peaks of the streamwise Reynolds stress. It is also more accurate in measuring the wall-normal and spanwise turbulent intensities. Although the sample size for 3D-PTV was one order of magnitude bigger than tomo-PIV, owing to the fact that for 3D-PTV no 3D reconstruction is required the processing procedure is significantly faster. All in all, the 3D-PTV shows a higher capability in measuring the 3D flow statistics provided that enough sample size is selected for statistical convergence. Besides, by averaging the 3D-PTV vectors in averaging bins a vector field can be obtained which is practical for vorticity investigations.

7. Conclusion and Recommendations for Future Research

Conclusion

Application of a superhydrophbic surface with random roughness for turbulent flow has been studied experimentally. To acquire a thorough comparison, turbulent flow over smooth, non-wetted SHO and wetted SHO surfaces is studied. Flow characteristics are measured using planar PIV applied in two different configurations of streamwise/wall-normal and streamwise/spanwise planes. The features of the SHO surface are at least an order of magnitude smaller than the sublayer thickness. A small increase in mean velocity (3-5%) is observed within $4< y^+ < 15$ over the non-wetted SHO surface. The normal and shear Reynolds stresses attenuate in the buffer and logarithmic layers by 15% with the peak wall-normal position moving away from the wall by 15 wall units. The flow over the wetted SHO surface does not experience any change in the mean velocity nor in the Reynolds stresses. This agrees with that fact that the roughness size is smaller than the thickness of viscous sublayer rendering a hydrodynamically smooth wall. Quadrant analysis of the sweep and ejection events suggests that the sweep/ejection events are suppressed due to the slip on the non-wetted SHO surface. The non-wetted SHO surface tends to have a stronger effect on the ejection events with increase of wall-normal distance. The intensity of the ejection and sweep events over the SHO surface is suppressed by 15% and 17% in comparison with the smooth wall, respectively. It was also seen that the transport of the turbulent kinetic energy is attenuated. The streamwise low and high speed streaks over the non-wetted SHO surface evolve to more coherent structures with 11% increase in spanwise spacing. Analysis of

vortical structures showed that the string spanwise vortical structures attenuate by 13% in the buffer layer over the non-wetted SHO. The reduction of Reynolds stresses along with attenuation of the ejection and sweep motions, low and high speed streams and the vortical structures indicate lower turbulence production over the non-wetted SHO surface.

The near-wall behavior of the flow is studied by means of long-range micro-PTV technique. The measurement accuracy of this technique is assessed by comparing the results with reference DNS data. The technique yields reliable results in terms of turbulence statistics compliance with theory and DNS.

Conducting volumetric measurements can further decipher the physics corresponding to the turbulence modification due to the application SHO surfaces. Especially, for the case of random SHO surfaces, this necessity is more pronounced as finding the alterations of spanwise statistics reveals the possible singularities attributed to omnidirectional slip. To this end, tomographic PIV and 3D particle tracking velocimetry as volumetric flow measurement techniques are two canonical diagnostic tools. The performances of these measurements are evaluated through comparison with reference DNS data and the results show that 3D-PTV yields more reliable data compared to tomo-PIV especially in near-wall region where the signal-to-noise ratio increases dramatically for PIV measurements.

Recommendations for Future Research

Planar PIV was used to delineate the physics behind superhydrophobic surface effects on the turbulent channel flow. Performances of other image-based diagnostic techniques (high-magnification 2D-PTV, tomo-PIV and 3D-PTV) were also evaluated as potential techniques to further investigations. Further research as future work is proposed below:

- *Investigating the effect of Reynolds number on the turbulent flow modifications due to SHO surface*. It has been shown that for patterned SHO surfaces, drag reduction increases with Re number. However, study of Bidkar *et al.* (2014) showed that this effect is vice versa for random SHO surface. PIV measurements could help with understanding the circumstances of changes.

- *Performing long-range micro-PTV and micro-PIV measurements in the near-wall region the turbulent channel flow.* One specific difference between turbulent flows over random and patterned SHO surfaces is the displacement of the wall-normal position of peak value in turbulent intensity profiles. Although it has been reported that the peak point move towards the wall for patterned surfaces (Jelly *et al.*, 2014), it was shown here (Chapter 4) that the peak point move away from the wall for random surfaces.
- *Conducting three-dimensional measurement (3D-PTV and tomo-PIV).* To investigate the spanwise fluctuations of the turbulent boundary layer as well as studying the turbulent coherent structures e.g. vortices it is necessary to carry on a 3D measurement.

References

Adrian, R. J., (2007). Hairpin vortex organization in wall turbulence, *Physics of Fluids*, *041301*(19). doi:10.1063/1.2717527

Adrian, R. J., Meinhart, C. D., & Tomkins, C. D. (2000). Vortex organization in the outer region of the turbulent boundary layer. *Journal of Fluid Mechanics*, *422*, 1–54. doi:10.1017/S0022112000001580

Aljallis, E., Sarshar, M. A., Datla, R., Sikka, V., Jones, A., & Choi, C.-H. (2013). Experimental study of skin friction drag reduction on superhydrophobic flat plates in high Reynolds number boundary layer flow. *Physics of Fluids*, *25*(2), 025103. doi:10.1063/1.4791602

Andreopoulos, J., & Bradshaw, P. (1981). Measurements of turbulence structure in the boundary layer on a rough surface. *Boundary-Layer Meteorology*, *20*(1978), 201–213. doi:10.1007/BF00119902

Barthlott, W., & Neinhuis, C. (1997). Purity of the sacred lotus, or escape from contamination in biological surfaces. *Planta*, *202*(1), 1–8.

Bidkar, R. a., Leblanc, L., Kulkarni, A. J., Bahadur, V., Ceccio, S. L., & Perlin, M. (2014). Skin-friction drag reduction in the turbulent regime using random-textured hydrophobic surfaces. *Physics of Fluids*, *26*(8), 085108. doi:10.1063/1.4892902

Bocquet, L., & Lauga, E. (2011). A smooth future? *Nature Materials*, *10*(5), 334–337. doi:10.1038/nmat2994

Brinker, C. J. et al. (2008). Superhydrophobic coating. US Patent, USA.

Byun, D., Kim, J., Ko, H. S., & Park, H. C. (2008). Direct measurement of slip flows in superhydrophobic microchannels with transverse grooves. *Physics of Fluids*, *20*(11). doi:10.1063/1.3026609

Smith, S. P. M. (1983). Characterization of low-speed streaks in the near-wall region of a turbulent boundary layer. *J. Fluid Mechanics*, *129*, 27–54.

Callies, M., & Quéré, D. (2005). On water repellency. *Soft Matter*, *1*(1), 55–61.

Carpenter, P. (1997). The right sort of roughness, *Nature*, *388*(August), 713–714.

Choi, K. (2006). The rough with the smooth, *Nature*, *440*(April), 754.

Daniello, R. J., Waterhouse, N. E., & Rothstein, J. P. (2009). Drag reduction in turbulent flows over superhydrophobic surfaces. *Physics of Fluids*, *21*(8), 085103. doi:10.1063/1.3207885

Davidson, P. A. (2004). *Turbulence: An Introduction for Scientists and Engineers*. Oxford: Oxford University Press.

Elbing, B. R., Winkel, E. S., Lay, K. a., Ceccio, S. L., Dowling, D. R., & Perlin, M. (2008). Bubble-induced skin-friction drag reduction and the abrupt transition to air-layer drag reduction. *Journal of Fluid Mechanics*, *612*, 201–236. doi:10.1017/S0022112008003029

Elsinga, G. E., Scarano, F., Wieneke, B., & van Oudheusden, B. W. (2006). Tomographic particle image velocimetry. *Experiments in Fluids*, *41*(6), 933–947. doi:10.1007/s00348-006-0212-z

Evershed, R. P., Berstan, R., Grew, F., Copley, M. S., Charmant, A. J. H., Barham, E., … Brown, G. (1983). Water-repellent legs of water striders. *Carbohyd. Res*, *113*, 291–299.

Farshad, F. F., & Pesacreta, T. C. (2003). Coated pipe interior surface roughness as measured by three scanning probe instruments. *Anti-Corrosion Methods and Materials*, *50*(1), 6–16. doi:10.1108/00035590310456243

Gad-el-Hak, M. (2013). Comment on “Experimental study of skin friction drag reduction on superhydrophobic flat plates in high Reynolds number boundary layer flow” [Phys. Fluids 25, 025103 (2013)]. *Physics of Fluids*, *25*(7), 079101. doi:10.1063/1.4816362

Ghaemi, S. (2013). *Pressure fluctuations in the turbulent boundary layer*. PhD Thesis, Delft University of Technology.

Ghaemi, S., & Scarano, F. (2011). Counter-hairpin vortices in the turbulent wake of a sharp trailing edge. *Journal of Fluid Mechanics*, *689*, 317–356. doi:10.1017/jfm.2011.431

Guo, Z., & Liu, W. (2007). Biomimic from the superhydrophobic plant leaves in nature: Binary structure and unitary structure. *Plant Science*, *172*(6), 1103–1112.

Haibao, H., Peng, D., Feng, Z., Dong, S., & Yang, W. (2015). Effect of hydrophobicity on turbulent boundary layer under water. *Experimental Thermal and Fluid Science*, *60*, 148–156. doi:10.1016/j.expthermflusci.2014.08.013

Hinds, W. C. (2012). *Aerosol technology: properties, behavior, and measurement of airborne particles*. John Wiley & Sons.

Huang, D. M., Sendner, C., Horinek, D., Netz, R. R., & Bocquet, L. (2008). Water Slippage versus Contact Angle: A Quasiuniversal Relationship. *Physical Review Letters*, *101*(22), 226101. Retrieved from http://link.aps.org/doi/10.1103/PhysRevLett.101.226101

Hulst, V. D. (1981). *Light Scattering by Small Particles*. New York: John Wiley & Sons.

Hussain, K. M. F. (1986). Coherent structures and turbulence, *J. Fluid Mech*., *173*, 303–356. doi:10.1017/S0022112086001192

J.C.R. Hunt, A.A. Wray, P. M. (1988). Eddies, Streams, and Convergence Zones in Turbulent Flows. *Research Report CTR-S88, Center for Turbulence*, 193–208.

Jelly, T. O., Jung, S. Y., & Zaki, T. a. (2014). Turbulence and skin friction modification in channel flow with streamwise-aligned superhydrophobic surface texture. *Physics of Fluids*, *26*(9), 095102. doi:10.1063/1.4894064

Joseph, P., Cottin-Bizonne, C., Benoît, J. M., Ybert, C., Journet, C., Tabeling, P., & Bocquet, L. (2006). Slippage of water past superhydrophobic carbon nanotube forests in microchannels. *Physical Review Letters*, *97*(15), 1–4. doi:10.1103/PhysRevLett.97.156104

Jung, Y. C., & Bhushan, B. (2010). Biomimetic structures for fluid drag reduction in laminar and turbulent flows. *Journal of Physics: Condensed Matter*, *22*(3), 35104.

Kähler, C. J., Scharnowski, S., & Cierpka, C. (2012a). On the resolution limit of digital particle image velocimetry. *Experiments in Fluids*, *52*(6), 1629–1639. doi:10.1007/s00348-012-1280-x

Kähler, C. J., Scharnowski, S., & Cierpka, C. (2012b). On the uncertainty of digital PIV and PTV near walls. *Experiments in Fluids*, *52*, 1641–1656. doi:10.1007/s00348-012-1307-3

Keane, R. D., & Adrian, R. J. (1992). Theory of cross-correlation analysis of PIV images. *Applied Scientific Research*, *49*(3), 191–215.

Kim, J. (2011). Physics and control of wall turbulence for drag reduction. *Philosophical Transactions. Series A, Mathematical, Physical, and Engineering Sciences*, *369*, 1396–1411. doi:10.1098/rsta.2010.0360

Kim, J., Moin, P., & Moser, R. (1987). Turbulence statistics in fully developed channel flow at low Reynolds number. *Journal of Fluid Mechanics*, *177*, 133–166.

Kim, J., Moin, P., & Moser, R. (1987). Turbulence statistics in fully developed channel flow at low Reynolds number. *J. Fluid Mech.*, *177*, 133–166. doi:10.1017/S0022112087000892

Klebanoff, P. (1955). Characteristics of turbulence in boundary layer with zero pressure gradient. *NACA TN-3178*.

Kline, S. J., Reynolds, W. C., Schraub, F. A., & Runstadler, P. W. (1967). The structure of turbulent boundary layers. *Journal of Fluid Mechanics*, *30*(04), 741–773.

Koch, K., Bhushan, B., & Barthlott, W. (2008). Diversity of structure, morphology and wetting of plant surfaces. *Soft Matter*, *4*(10), 1943–1963.

Lafuma, A., & Quéré, D. (2003). Superhydrophobic states. *Nature Materials*, *2*(7), 457–60. doi:10.1038/nmat924

Lauga, E., & Stone, H. A. (2003). Effective slip in pressure-driven Stokes flow. *Journal of Fluid Mechanics*, *489*, 55–77.

Lee, C., & Kim, C. J. (2009). Maximizing the giant liquid slip on superhydrophobic microstructures by nanostructuring their sidewalls. *Langmuir*, *25*(21), 12812–12818.

Lumley, J., & Blossey, P. (1998). Control of Turbulence. *Annual Review of Fluid Mechanics*, *30*, 311–327. doi:10.1146/annurev.fluid.30.1.311

Marmur, A. (2003). Wetting on hydrophobic rough surfaces: to be heterogeneous or not to be? *Langmuir*, *19*(20), 8343–8348.

Martell, M. B., Perot, J. B., & Rothstein, J. P. (2009). Direct numerical simulations of turbulent flows over superhydrophobic surfaces. *Journal of Fluid Mechanics*, *620*, 31. doi:10.1017/S0022112008004916

Martell, M. B., Rothstein, J. P., & Perot, J. B. (2010). An analysis of superhydrophobic turbulent drag reduction mechanisms using direct numerical simulation. *Physics of Fluids*, *22*(6), 065102. doi:10.1063/1.3432514

Maynes, D., Jeffs, K., Woolford, B., & Webb, B. W. (2007). Laminar flow in a microchannel with hydrophobic surface patterned microribs oriented parallel to the flow direction. *Physics of Fluids (1994-Present)*, *19*(9), 93603.

Meinhart, C. D., Wereley, S. T., & Santiago, J. G. (2000). A PIV Algorithm for Estimating Time-Averaged Velocity Fields. *Journal of Fluids Engineering*, *122*(June 2000), 285. doi:10.1115/1.483256

Merzkirch, W. (2001). Particle image velocimetry. In *Optical Measurements* (pp. 341–357). Springer.

Min, T., & Kim, J. (2004). Effects of hydrophobic surface on skin-friction drag. *Physics of Fluids*, *16*(7), L55. doi:10.1063/1.1755723

Moaven, K., Rad, M., & Taeibi-Rahni, M. (2013). Experimental investigation of viscous drag reduction of superhydrophobic nano-coating in laminar and turbulent flows. *Experimental Thermal and Fluid Science*, *51*, 239–243. doi:10.1016/j.expthermflusci.2013.08.003

Moser, R. D., Kim, J. D., & Mansour, N. N. (1999). Direct Numerical Simulation of Turbulent Channel Flow up to Re_τ=590. *Physics of Fluids*, *11*(4), 943–945.

Moser, R. D., Kim, J., & Mansour, N. N. (1999). Direct numerical simulation of turbulent channel flow up to Re 590 ₠. *Physics of Fluids*, *11*(4), 943–945. doi:10.1063/1.869966

Navier, C. (1823). Mémoire sur les lois du mouvement des fluides. *Mémoires de l'Académie Royale Des Sciences de l'Institut de France*, *6*, 389–440.

Ou, J., Perot, B., & Rothstein, J. P. (2004). Laminar drag reduction in microchannels using ultrahydrophobic surfaces. *Physics of Fluids (1994-Present)*, *16*(12), 4635–4643.

Park, H., Sun, G., & Kim, C. J. (2014). Superhydrophobic turbulent drag reduction as a function of surface grating parameters. *Journal of Fluid Mechanics*, *747*, 722–734. doi:10.1017/jfm.2014.151

Peguero, C., & Breuer, K. (2009). On Drag Reduction in Turbulent Channel Flow over Superhydrophobic Surfaces. *Advances in Turbulence XII*, *132*, 233–236. doi:10.1007/978-3-642-03085-7

Raffel, M., Willert, C.E., Wereley, S.T., Kompenhans, J. (2007). *Particle Image Velocimetry* (2nd ed.). Springer.

Rastegari, A., & Akhavan, R. (2015). On the mechanism of turbulent drag reduction with super-hydrophobic surfaces. *Journal of Fluid Mechanics*, *773*, R4. doi:10.1017/jfm.2015.266

Roach, P., Shirtcliffe, N. J., & Newton, M. I. (2008). Progess in superhydrophobic surface development. *Soft Matter*, *4*(2), 224–240.

Robinson, S. K. (1991). Coherent motions in the turbulent boundary layer. *Annu. Rev. Fluid Mech*. *23*, 901-39, doi:10.1146/annurev.fluid.23.1.601

Rothstein, J. P. (2010a). Slip on Superhydrophobic Surfaces. *Annual Review of Fluid Mechanics*, *42*(1), 89–109. doi:10.1146/annurev-fluid-121108-145558

Rothstein, J. P. (2010b). Slip on Superhydrophobic Surfaces. *Annual Review of Fluid Mechanics*, *42*, 89–109. doi:10.1146/annurev-fluid-121108-145558

S. Pope. (2000). *Turbulent Flows*. Cambridge University Press.

Samaha, M., Tafreshi, H. V., & Gad-el-Hak, M. (2012). Superhydrophobic surfaces: From the lotus leaf to the submarine. *Comptes Rendus - Mecanique*, *340*(1-2), 18–34. doi:10.1016/j.crme.2011.11.002

Sanders, W. C., Winkel, E. S., Dowling, D. R., Perlin, M., & Ceccio, S. L. (2006). Bubble friction drag reduction in a high-Reynolds-number flat-plate turbulent boundary layer. *Journal of Fluid Mechanics*, *552*(-1), 353. doi:10.1017/S0022112006008688

Scarano, F. (2013). *Experimental Aerodynamics*. Delft University of Technology.

Scarano, F. (2013). Tomographic PIV: principles and practice. *Measurement Science and Technology*, *24*(1), 012001. doi:10.1088/0957-0233/24/1/012001

Schultz, M. P., & Flack, K. a. (2007). The rough-wall turbulent boundary layer from the hydraulically smooth to the fully rough regime. *Journal of Fluid Mechanics*, *580*, 381. doi:10.1017/S0022112007005502

Sendner, C., Horinek, D., Bocquet, L., & Netz, R. R. (2009). Interfacial water at hydrophobic and hydrophilic surfaces: Slip, viscosity, and diffusion. *Langmuir*, *25*(18), 10768–10781.

Sheng, J., Malkiel, E., & Katz, J. (2009). Buffer layer structures associated with extreme wall stress events in a smooth wall turbulent boundary layer. *Journal of Fluid Mechanics*, *633*, 17–60.

Sirovich, L., & Karlsson, S. (1997). Turbulent drag reduction by passive mechanisms, *Nature*, 388 (February), 728–730.

Smith, C. R., & Metzler, S. P. (1983). The characteristics of low-speed streaks in the near-wall region of a turbulent boundary layer. *Journal of Fluid Mechanics*, *129*, 27–54.

Spalart, P. R. (1988). Direct simulation of a turbulent boundary layer up to Rθ= 1410. *Journal of Fluid Mechanics*, *187*, 61–98.

Stanislas, M., Perret, L., & FOUCAUT, J. (2008). Vortical structures in the turbulent boundary layer: a possible route to a universal representation. *Journal of Fluid Mechanics*, *602*, 327–382.

Stone, H. A., Stroock, A. D., & Ajdari, A. (2004). Engineering flows in small devices. *Annual Review of Fluid Mechanics*, *36*(1), 381–411. doi:10.1146/annurev.fluid.36.050802.122124

Theodorsen, T. (1952). Mechanism of Turbulence. In *Proc. 2nd Midwest. Conf. Fluid Mech.* (pp. 1–19). Columbus, Ohio.

Türk, S., Daschiel, G., Stroh, a., Hasegawa, Y., & Frohnapfel, B. (2014). Turbulent flow over superhydrophobic surfaces with streamwise grooves. *Journal of Fluid Mechanics*, *747*, 186–217. doi:10.1017/jfm.2014.137

Verho, T., Bower, C., Andrew, P., Franssila, S., Ikkala, O., & Ras, R. H. a. (2011). Mechanically durable superhydrophobic surfaces. *Advanced Materials (Deerfield Beach, Fla.)*, *23*(5), 673–8. doi:10.1002/adma.201003129

Vinogradova, O. I. (1995). Drainage of a Thin Liquid Film Confined between Hydrophobic Surfaces. *Langmuir*, *11*(6), 2213–2220. doi:10.1021/la00006a059

Vinogradova, O. I., & Belyaev, A. V. (2011). Wetting, roughness and flow boundary conditions. *Journal of Physics. Condensed Matter : An Institute of Physics Journal*, *23*, 184104. doi:10.1088/0953-8984/23/18/184104

Wallace, J. M., Eckelmann, H., & Brodkey, R. S. (1972). The wall region in turbulent shear flow. *Journal of Fluid Mechanics*, *54*(01), 39–48.

Walsh, M. J. (1983). Riblets as a Viscous Drag Reduction Technique. *AIAA Journal*, *21*(4), 485–486. doi:10.2514/3.60126

Walsh, M., & Lindemann, A. (1984). Optimization and application of riblets for turbulent drag reduction. In *22nd Aerospace Sciences Meeting*. American Institute of Aeronautics and Astronautics. doi:doi:10.2514/6.1984-347

Wenzel, R. N. (1936). Resistence of solid surfaces to wetting by water. *Ind. Eng. Chem.*, *28*(8), 988–994. doi:10.1021/ie50320a024

Wenzel, R. N. (1949). Surface Roughness and Contact Angle. *J. Phys. Chem.*, *53*(9), 1466–1467.

Westerweel, J., & Scarano, F. (2005). Universal outlier detection for PIV data. *Experiments in Fluids*, *39*, 1096–1100. doi:10.1007/s00348-005-0016-6

White, C. M., & Mungal, M. G. (2008). Mechanics and Prediction of Turbulent Drag Reduction with Polymer Additives. *Annual Review of Fluid Mechanics*, *40*(1), 235–256. doi:10.1146/annurev.fluid.40.111406.102156

White, C. M., Somandepalli, V. S. R., & Mungal, M. G. (2004). The turbulence structure of drag-reduced boundary layer flow. *Experiments in Fluids*, *36*(October 2002), 62–69. doi:10.1007/s00348-003-0630-0

Wieneke, B. (2008). Volume self-calibration for 3D particle image velocimetry. *Experiments in Fluids*, *45*(4), 549–556. doi:10.1007/s00348-008-0521-5

Woolford, B., Maynes, D., & Webb, B. W. (2009). Liquid flow through microchannels with grooved walls under wetting and superhydrophobic conditions. *Microfluidics and Nanofluidics*, *7*(1), 121–135.

Woolford, B., Prince, J., Maynes, D., & Webb, B. W. (2009). Particle image velocimetry characterization of turbulent channel flow with rib patterned superhydrophobic walls. *Physics of Fluids*, *21*(8), 085106. doi:10.1063/1.3213607

Yan, Y. Y., Gao, N., & Barthlott, W. (2011). Mimicking natural superhydrophobic surfaces and grasping the wetting process: A review on recent progress in preparing superhydrophobic surfaces. *Advances in Colloid and Interface Science*, *169*(2), 80–105. doi:10.1016/j.cis.2011.08.005

Zhao, J., Du, X., & Shi, X. (2007). Experimental research on friction-reduction with super-hydrophobic surfaces. *Journal of Marine Science and Application*, *6*(3), 58–61. doi:10.1007.

Appendix A

Surface roughness parameters

The surface roughness R_a, also known as arithmetic roughness (Farshad & Pesacreta, 2003), is defined as:

$$R_a = \frac{1}{L}\int_0^L |Z(x) - \bar{Z}|\, dx \tag{A.1}$$

where $Z(x)$ is the wall-normal coordinate of the surface, L is the profile measurement length and $\bar{Z}$ is the mean of the measured profile $Z(x)$.

The average root-mean-square height, R_{rms}, of the roughness profiles is found from

$$R_{rms} = \sqrt{\frac{1}{L}\int_0^L |Z(x) - \bar{Z}|^2\, dx} \tag{A.2}$$

The mean peak-to-trough roughness height is defined as the average of the maximum peak-to-trough heights of roughness profiles within five consecutive sampling subsections of the measured profiles(Farshad & Pesacreta, 2003)

$$R_{PT} = \frac{1}{5}(Z_1 + Z_2 + Z_3 + Z_4 + Z_5) \tag{A.3}$$

where Z_i is the maximum peak-to-trough height in i-th sampling subsection length.

The skewness of the profile is defined as:

$$Skewness = \frac{1}{R_{rms}^3}\left[\frac{1}{L}\int_0^L |Z(x) - \bar{Z}|^3\, dx\right] \tag{A.4}$$

Appendix B

A survey on optimal image preprocessing and vector field post-processing procedure for planar PIV

The initial results from the first set of processed 2C-PIV data did not conform to the physics of the flow. Especially, observation of drastically higher quantities for turbulent intensities associated with wetted SHO surface was not in accord with the fluid dynamical criteria. The roughness elements on a surface are not influential on flow characteristics of a turbulent boundary layer unless their characteristic height exceeds the minimum critical value. As discussed in chapter 4, the roughness on the current surface (once fully wetted) does not meet this criterion so, theoretically it is considered as a smooth wall. This observation warranted a thorough investigation in order to ascertain the optimum accurate image pre-processing and vector field post-processing procedure.

All acquired images are pre-processed prior to any cross-correlation steps to increase the signal-to-noise ratio which in turn improves the cross-correlation quality leading to lower number of erroneous vectors and/or higher resolution. This survey is designed to examine the effects of different processing steps. Each step is added consecutively resulting in five particular combinations of image pre-processing and vector field post-processing approaches. To precisely inspect the accuracy of the approaches, turbulent intensities as second order statistics were studied so that any noise in the experiment would be amplified and observed easier. The final goal was to reduce the noise level. In all of the approaches, PIV images are improved for the cross-correlation algorithm by subtracting the ensemble minimum from the individual images. The other steps are either included or excluded to the five processing approaches as discussed in

the following paragraphs and the results are presented in figures B.1-3 for smooth, non-wetted SHO and wetted SHO surfaces, respectively.

1. Apart from the initial pre-processing step (described in section 3.1.3), in this approach no other pre-processing or post-processing steps were applied. However, the abovementioned problem with wetted SHO wall appeared with a significantly high level of noise for streamwise fluctuations.
2. The image pre-processing step was modified with particle intensity normalization with the scale of 5 pixels. No further post-processing steps were applied on the vector field. This approach, in spite of yielding very smooth vector fields and significantly lower number of bad vectors, resulted in unreasonable data for flow over non-wetted SHO surface particularly for streamwise turbulent intensities.
3. In this approach no additional pre-processing was conducted. However, the vector fields were post-processed by universal outlier detection(Westerweel & Scarano, 2005) and the empty spaces were filled up with interpolation. Yet, the similar problem to first approach persisted albeit diminished.
4. In this stage, the images were initially multiplied by a constant number to intensify the signal level, and subsequently, were normalized by the ensemble average of the recordings. Other pre/post-processing steps were selected as approach one. Similarly, the unrealistic streamwise fluctuations for wetted SHO surface were observed even though declined.
5. As the final approach, a combination of approach 3 and 4 were adopted while an additional post-processing step consisting of limiting the allowable vector range to -0.03 to +0.03 m/s for wall-normal and 0 to 0.2 m/s for streamwise velocity was used to further eliminate the bad vectors. The eliminated vectors were substituted with interpolated vectors.

The final approach resulted in realistic turbulent intensities for wetted SHO surface. It contains lower level of noise and yielded a rather smooth profile therefore it was adopted as the final processing approach.

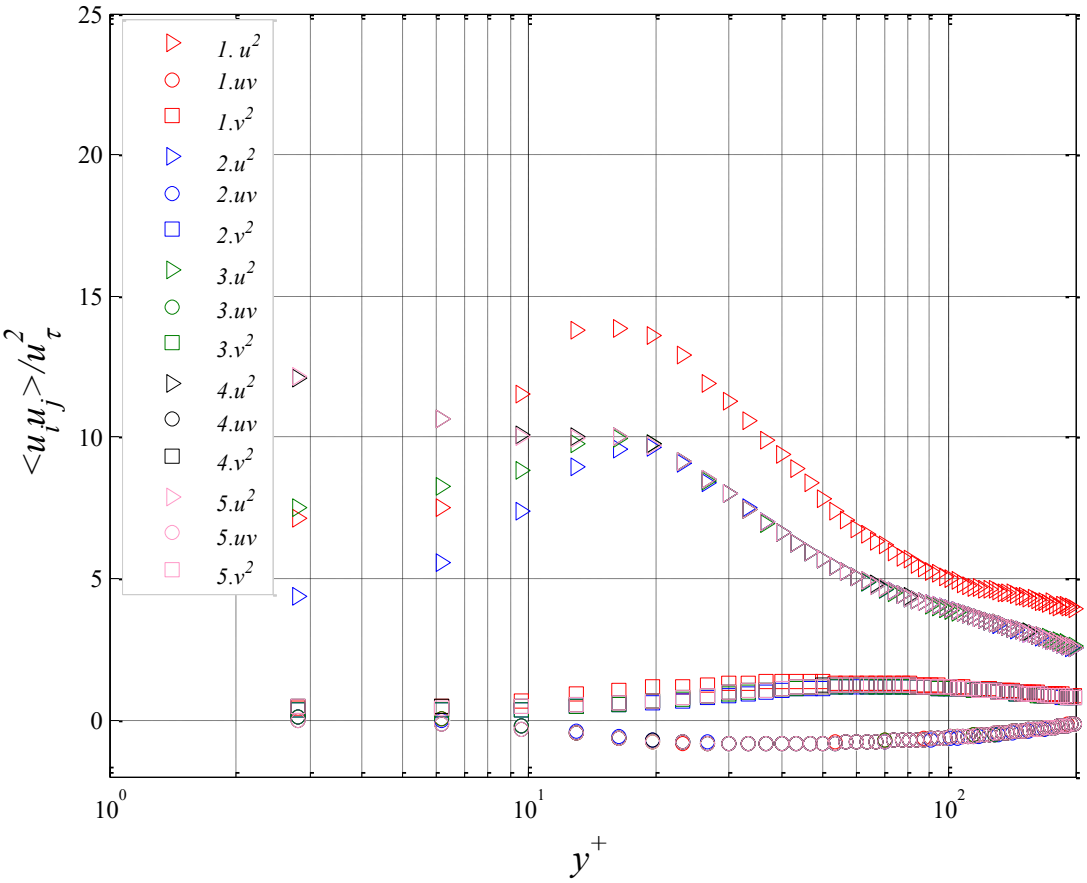

Fig.B.1. Turbulent intensities associated with turbulent boundary layer over a smooth reference surface.

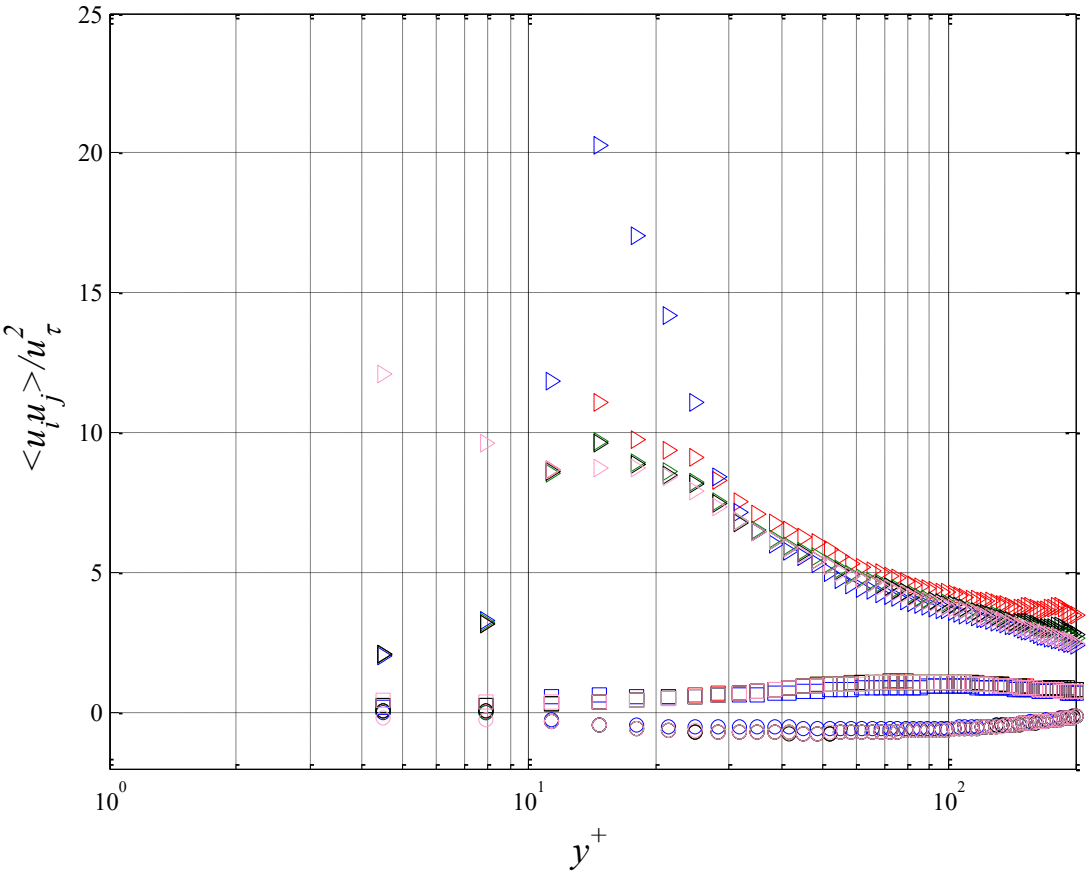

Fig. B.2. Turbulent intensities associated with turbulent boundary layer over the non-wetted SHO surface. The marker symbols are the same as in Fig. B.1.

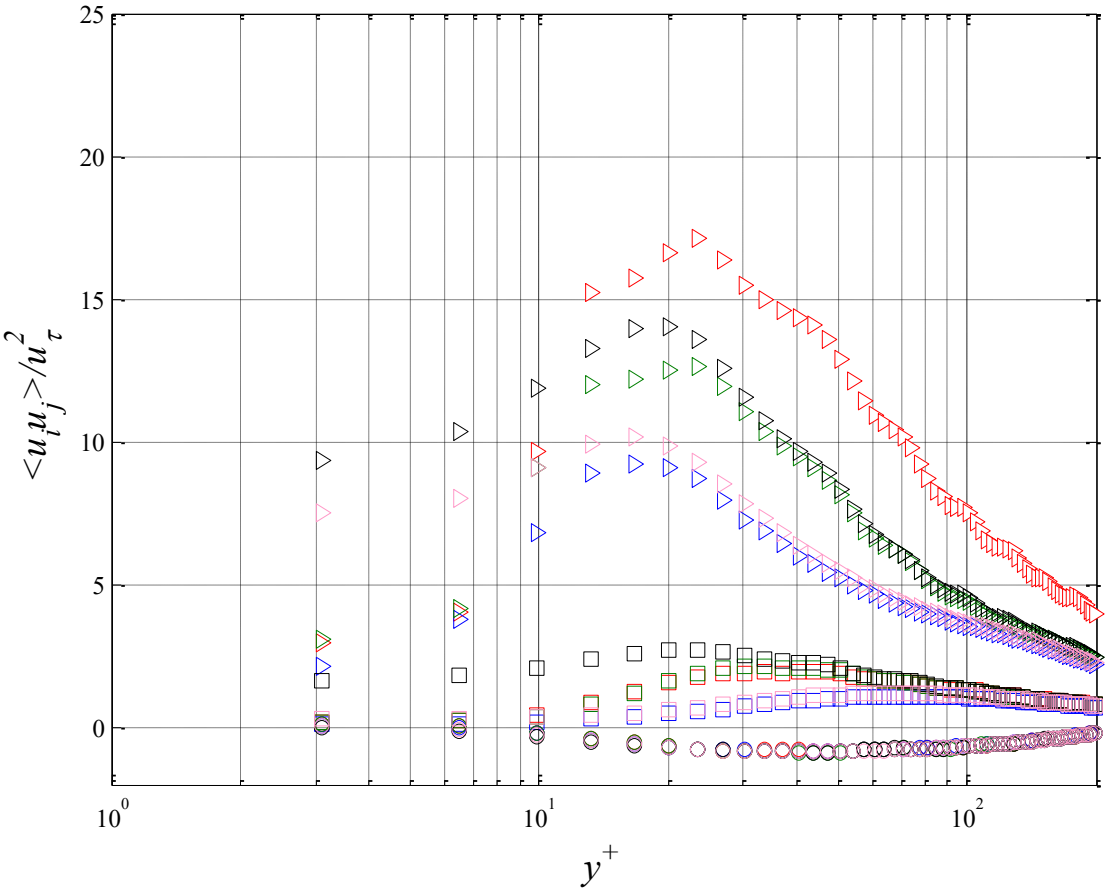

Fig.B.3. Turbulent intensities associated with turbulent boundary layer over the wetted SHO surface. The marker symbols are the same as in Fig. B.1.

Appendix C

3D measurement results of flow over smooth and SHO surfaces compared with DNS results

Here, the results of the experiment presented in Chapter 6, including the SHO surface data has been discussed. Figure C.1.a and b depict the mean velocity profiles obtained from tomo-PIV and 3D-PTV experiments, respectively. Figures C.2.a-d and C.3.a-d demonstrate the mean Reynolds stress profiles from tomo-PIV and 3D-PTV, respectively. As a reference the DNS data of (Robert D Moser *et al.*, 1999) at Re_τ = 178 are also added. The upper wall (where the replaceable module is installed) is at y=0 in all plots.

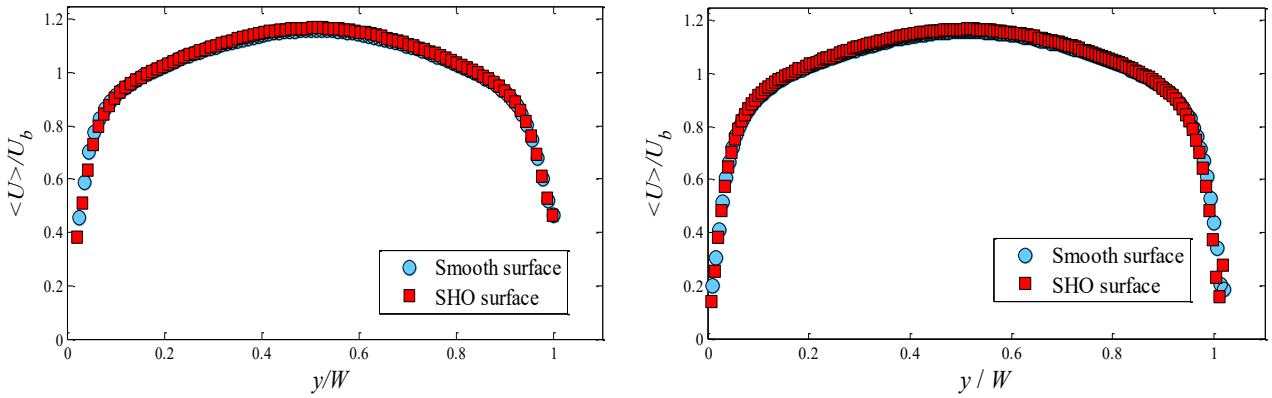

(a) (b)

Fig. C.1. Mean velocity profile obtained from (a) Tomo-PIV, (b) 3D-PTV.

a)

b)

c)

d)

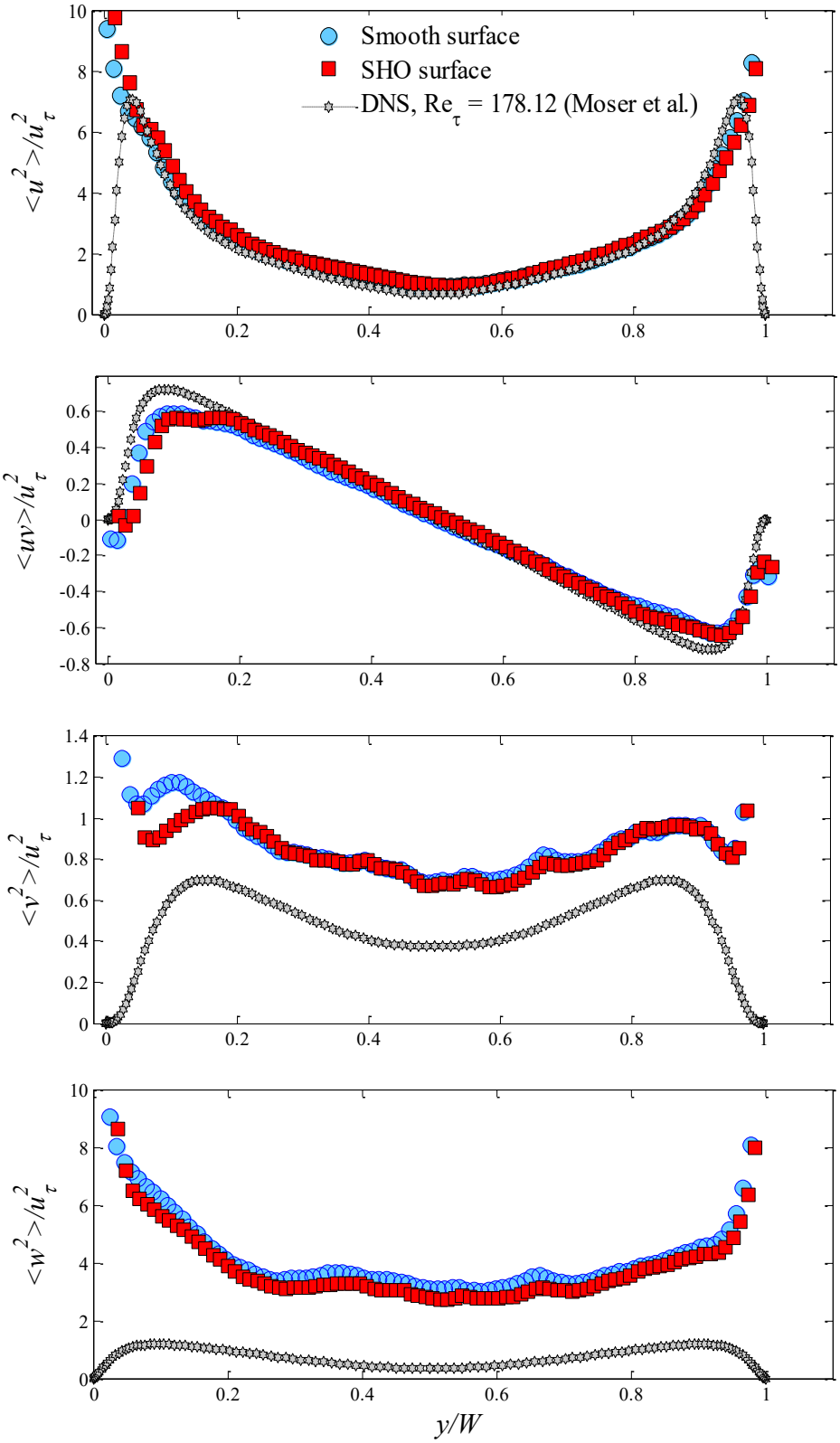

Fig. C.2. Mean Turbulent intensity profiles acquired from tomo-PIV. a) $<u^2>/u_\tau^2$, b) $<v^2>/u_\tau^2$, c) $<uv>/u_\tau^2$. d) $<w^2>/u_\tau^2$.

a)

b)

c)

d)

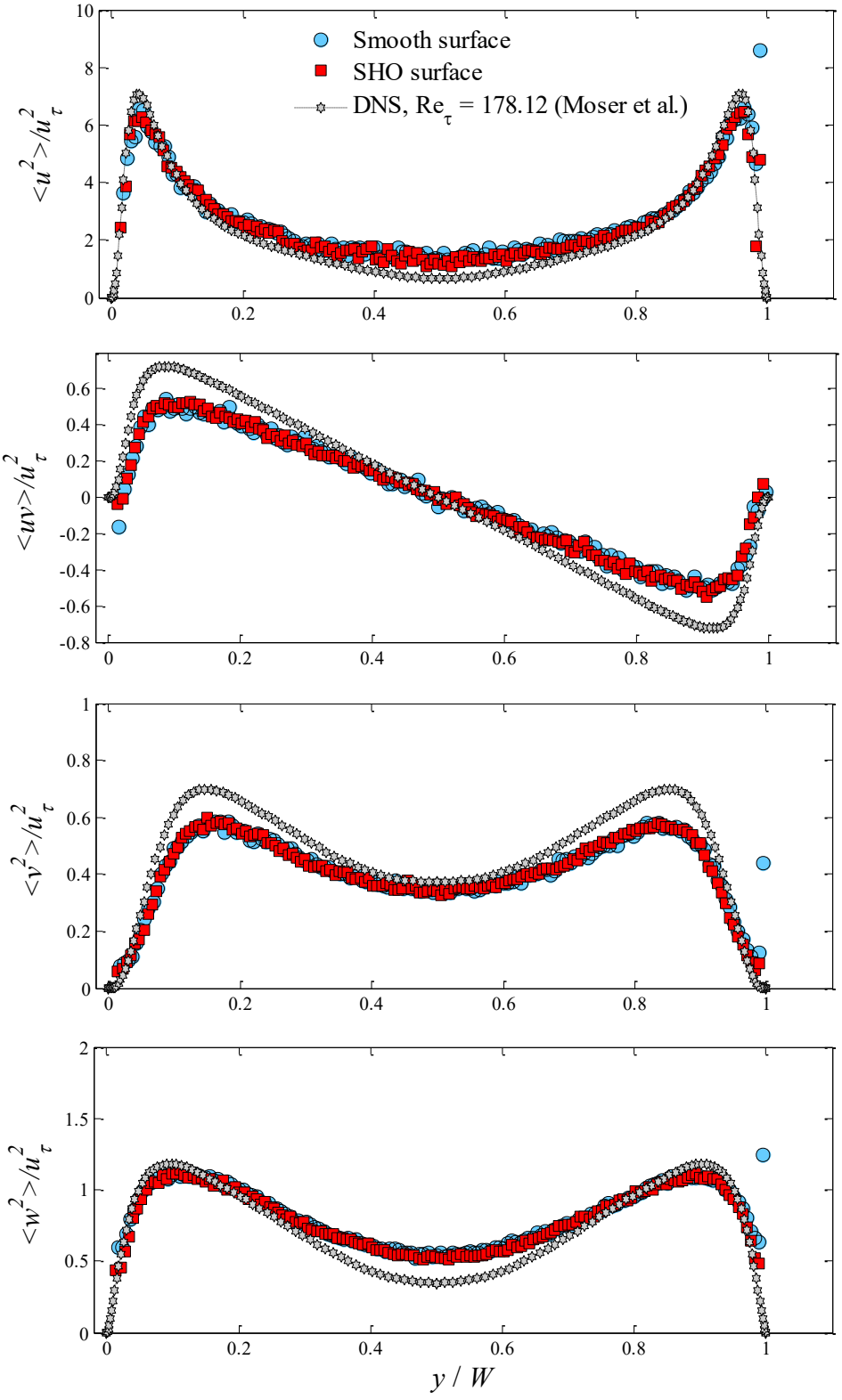

Fig. C.3. Mean Turbulent intensity profiles acquired from 3D-PTV. a) $<u^2>/u_\tau^2$, b) $<v^2>/u_\tau^2$, c) $<uv>/u_\tau^2$. d) $<w^2>/u_\tau^2$.